ABSTRACT

A Search for Universal Extra Dimensions in the Multi-Lepton Channel
from Proton-Antiproton Collisions at $\sqrt{s}$=1.8 TeV

Chun Lin

2005

In this thesis we present the results of a search for Universal Extra Dimensions (UED) with compactification radius near the TeV scale in the multi-lepton channel from proton-antiproton collisions at center-of-mass energy of 1.8 TeV at the Fermi National Accelerator Laboratory. This is the first UED search in the multi-lepton channel performed at the Tevatron.

In the UED scenario, Kaluza-Klein (KK) excitations of Standard Model (SM) particles would be pair produced at the Tevatron and would undergo cascade decays into their zero mode counterparts (SM particles) and the lightest KK particle (LKP). The LKP, the first KK excited photon, is stable and will escape the detector, resulting in a missing energy signature. The signature of the UED scenario we consider is multiple SM leptons, jets and missing energy. We present the result from an analysis of a multi-lepton search using CDF Run IB data corresponding to an integrated luminosity of 87.5 pb^{-1}. We set an upper limit for the total KK production cross section $\sigma_{KK} < 7.9$ pb at 95% confidence level, corresponding to a minimum extra dimension energy scale of 280 GeV (maximum radius of 3.5×10^{-19} m).

A Search for Universal Extra Dimensions in the Multi-Lepton Channel from Proton-Antiproton Collisions at $\sqrt{s}$=1.8 TeV

A Dissertation

Presented to the Faculty of the Graduate School

of

Yale University

in Candidacy for the Degree of

Doctor of Philosophy

by

Chun Lin

Dissertation Directors: Colin Gay, Michael Schmidt

December, 2005

© 2005 by Chun Lin

All rights reserved.

This dissertation is dedicated to my parents.

Acknowledgements

I would like to thank many people who through their knowledge, guidance, support and friendship, have made the completion of this thesis possible.

My deepest thanks go to my thesis advisors Professor Colin Gay and Professor Michael Schmidt for giving me the opportunity to join the group and conduct an exciting analysis at CDF and Fermilab. I gratefully acknowledge their continuous guidance and support in all aspects of the research.

This thesis would not have been possible without the dedicated effort of the entire CDF collaboration and the Fermilab staff. People in the Yale CDF group helped me greatly with my research, especially Andrew Martin, Greg Feild, Steve Nahn, and Marcel Stanitzki. I benefitted from many useful discussions with them and learned a great deal of experimental particle physics.

This research received much feedback from the members of the CDF Exotic physics analysis group. Special mention goes to Alexei Safonov, Amitabh Lath, Teruki Kamon, and Stephan Lammel. The conveners, Beate Heinemann and Song Ming Wang were especially supportive. I thank Bogdan Dobrescu of Fermilab theoretical physics department for providing many suggestions to improve this analysis.

I received guidance and support from members of the CDF DAQ group for my CDF Run II service task of implementing various dynamic prescaling algorithms in the trigger rates monitor (ScalerMon) [73]. Special thank goes to William Badgett and Jonathan Lewis.

There were also many friends who have made my graduate student life memorable.

I would thank my fellow graduate students in the CDF Yale group particularly, Zhaoou Yu, Ke Li and Chun Yang, for their friendship and mutual support in the research.

I wish to thank my thesis committee members Andreas Heinz, Homer Neal, Jack Sandweiss, and Witold Skiba for reading my dissertation and providing many helpful suggestions.

Finally, I can't thank enough for the love, support and encouragement of my family - my parents, and my wife Yuhong.

Contents

1 Introduction **1**

2 Theory **4**

2.1 The Standard Model 4

2.2 Extra Dimensions 9

2.2.1 Kaluza-Klein Theory of Extra Spacetime Dimensions 10

2.2.2 Large Extra Dimensions - the ADD Model 14

2.2.3 Warped Extra Dimensions - the RS Model 16

2.2.4 Universal Extra Dimensions - the ACD Model 18

2.3 The Minimal Universal Extra Dimensions Scenario 19

2.3.1 Kaluza-Klein Modes Expansion on S^1/Z_2 Orbifold 20

2.3.2 MUED Mass Spectrum 22

2.3.3 Comparison of MSSM and MUED 26

3 Apparatus **28**

3.1 The Tevatron 29

3.2 The Collider Detector at Fermilab 33

3.2.1 The Tracking Detectors 36

3.2.2 Calorimeters 40

3.2.3 The Muon Chambers 45

3.2.4 Beam-Beam Counters 47
3.2.5 The Trigger Systems 48

4 Search Strategy **52**
4.1 Collider Phenomenology of the MUED Scenario 52
4.2 "Blind Analysis" Procedure 57

5 Data Sample **59**
5.1 Run IB Dilepton Sample 60
5.2 Run IB Trilepton Skimming Selection 65
5.3 Run IB Trilepton Analysis Selection 65

6 Standard Model Backgrounds **69**
6.1 Real Multi-Lepton events 70
6.2 Dilepton Plus Misidentified Lepton Events 72

7 Monte Carlo Simulations **76**
7.1 The MUED Signal Simulation 77
7.2 The Standard Model Background Simulation 78
7.3 Monte Carlo Efficiency Corrections 80
7.3.1 Trigger Efficiencies 80
7.3.2 Lepton Identification Efficiencies 81
7.3.3 Isolation Efficiencies 82

8 Data Analysis **84**
8.1 Bad Run Removal 84
8.2 Cosmic Ray Removal 84
8.3 Vertex Requirements 85

8.4 Charge Sum and Lepton Pair Requirements 86
8.5 Invariant Mass Requirements 86
8.6 Resonance Removal 88
8.7 $\Delta\phi_{\ell_1\ell_2}$ Requirements 88
8.8 Lepton Candidates Combinations Selection 88
8.9 Final Optimization Cuts 89
8.10 Summary of Events Selection Path, Expected Background and MUED Signal 91

9 Uncertainties 100

9.1 Systematic Uncertainty 100
9.2 Statistical Uncertainty 102
9.3 Theoretical Uncertainty 102

10 Limits on UED 105

10.1 Limit Setting Method 105
10.2 Cross Section Limit of KK Q_1Q_1 Pair Production 107
10.3 Cross Section Limit of KK Quark Pair Production + KK Gluon-Quark Production + KK Gluon Pair Production 109

11 Conclusion 112

A MUED Radiative Corrections to Kaluza-Klein Masses 114

B Run IB Standard Model Background Monte Carlo 116

C MUED Signal Monte Carlo Pythia TCL File 120

D $b\bar{b}/c\bar{c}$ Background Scale Factor 129

E Combined Results from all Channels including eee, $ee\mu$, $e\mu\mu$ and $\mu\mu\mu$ 136

F Results from the $\mu\mu\mu$ Channel 138

G Charged Multiplicity 143

Bibliography 149

List of Tables

2.1 List of leptons and their most fundamental properties. 5

2.2 List of quarks and their most fundamental properties. 5

2.3 List of bosons and their most fundamental properties. 6

2.4 Comparison of MSSM and MUED 27

3.1 Summary of the properties of the CDF calorimeters. 42

4.1 SU(2)-doublet KK quark decay branching ratios 55

5.1 Selection criteria for CEM and PEM electrons. 61

5.2 Selection criteria for CMU/P, CMX, and CMIO muons. 61

5.3 Analysis lepton selection cuts for CEM and PEM electrons. 66

5.4 Analysis lepton selection cuts for CMU/P, CMX and CMIO muons. . 66

7.1 MUED Monte Carlo points for $n = 1$ KK particles of different values of R and ΛR. 77

7.2 Summary of CDF Run IB lepton ID efficiencies. 82

7.3 Summary of calorimeter isolation efficiency of Run IB Z^0 data events. 83

7.4 Summary of calorimeter isolation efficiency of ISAJET+QFL Drell-Yan MC events. 83

8.1 Punzi Optimization Grid 90

8.2 Expected background, data and MUED signal after each cut. 91

10.1 Total detection efficiency in the non-$\mu\mu\mu$ Channels. 110

B.1 SM $b\bar{b}/c\bar{c}$ background M.C. 118

B.2 SM Drell-Yan background M.C. 119

B.3 SM $t\bar{t}$ background M.C. 119

B.4 SM boson pair background M.C. 119

D.1 Number of data and $b\bar{b}/c\bar{c}$ events in each dilepton channel in the invariant mass of 2 closest lepton less than 5 GeV/c^2 region. 130

D.2 Number of data and $b\bar{b}/c\bar{c}$ events in each trilepton channel in the invariant mass of 2 closest lepton less than 5 GeV/c^2 region. 135

E.1 In all channels, the expected background after each cut in different channels. 137

F.1 Expected background after each cut in the $\mu\mu\mu$ channel. 138

F.2 Total detection efficiency in the $\mu\mu\mu$ Channel. 139

F.3 Summary of Event: Run 63604 Event 108434 142

G.1 Expected background after each cut in different channels. 147

G.2 Total detection efficiency comparison of with and without charged multiplicity cut. 147

List of Figures

2.1 The SM based extrapolation of gauge couplings measurements. 8

2.2 Illustration of the Large Extra Dimensions - the ADD Model. 15

2.3 Illustration of the Warped Extra Dimensions - the RS Model. 17

2.4 The mass spectrum of the $n = 1$ modes at tree level for $R^{-1} = 500$ GeV, $\Lambda R = 20$ and $m_h = 120$ GeV. 22

2.5 The first few KK levels "Weinberg" angle θ_n versus (a) R^{-1}, for fixed $\Lambda R = 20$ and (b) ΛR. 24

2.6 One-loop corrected mass spectrum of the $n = 1$ modes for $R^{-1} = 500$ GeV, $\Lambda R = 20$ and $m_h = 120$ GeV. 24

2.7 Radiative corrections to the spectrum of the $n = 1$ modes for $R^{-1} =$ 500 GeV, versus ΛR. 25

2.8 The mass splitting between KK quarks and the LKP γ_1, as well as the splitting between the KK gauge bosons and the LKP, as a function of $1/R$ for $\Lambda R = 20$. 26

3.1 Schematic diagram of the Tevatron and its associated accelerators at Fermilab. 30

3.2 A perspective view of three quarters of the CDF detector. 34

3.3 A one quarter view of CDF. 34

3.4 One of the SVX′ barrels. 36
3.5 SVX′ ladder. 37
3.6 Diagram of the VTX. 38
3.7 Diagram of the CTC endplate. 39
3.8 The $\eta - \phi$ segmentation of the calorimeters in the CDF detector. . . . 43
3.9 Diagram of the CEM light collection system in a single wedge of the CEM and CHA calorimeters. 44
3.10 $\eta - \phi$ coverage of the muon system for the central region of the CDF detector. 46
3.11 Schematic drawing of the principal elements of the CDF data acquisition pipeline. 49

4.1 The $n = 1$ KK spectroscopy showing the dominant and rare transitions and the resulting decay products. 53
4.2 The cross section for the production of two stable KK final states as a function of the KK mass for Tevatron Run I. 54
4.3 The Feynman diagram for n=1 KK quark pair production and subsequent decays to 3 or 4 lepton final state. 55

6.1 The Feynman diagrams for leading and some higher order production of $b\bar{b}$. 71
6.2 The Feynman diagrams of tree-level $t\bar{t}$ production. 72
6.3 The Feynman diagrams of some higher order weak diboson production. 73
6.4 The Feynman diagrams for leading and some higher order Drell-Yan production. 74

7.1 MUED signal MC transverse momentum of three leptons after tight lepton cuts 78

7.2 MUED signal MC missing energy after tight lepton cuts 79
7.3 MUED signal MC isolation of three leptons after tight lepton cuts . . 79
7.4 MUED signal MC transverse momentum of the quark jets from decays of SU(2)-doublet KK quarks. 80

8.1 Distributions of invariant mass of the two closest leptons. 87
8.2 Distributions of opening angle of the two highest transverse momentum leptons. 92
8.3 Lepton state distribution of reconstructed SM background MC 93
8.4 Lepton state distribution of reconstructed signal MC 93
8.5 Distributions of invariant mass of the two closest leptons in the non-$\mu\mu\mu$ channels. 94
8.6 Distributions of opening angle of the two highest transverse momentum leptons in the non-$\mu\mu\mu$ channels. 95
8.7 Punzi search in non-$\mu\mu\mu$ channel of the cut matrix to optimize value $\mathbb{A}$. 96
8.8 Distributions of isolation in the non-$\mu\mu\mu$ channels. 97
8.9 Distributions of missing transverse energy in the non-$\mu\mu\mu$ channels. . 98
8.10 Distributions of missing transverse energy after isolation < 4 GeV cut in the non-$\mu\mu\mu$ channels. 99

D.1 Data invariant mass of the two closest leptons in the less than 5 GeV/c^2 region by lepton pair type. 131
D.2 Data invariant mass of the two closest leptons in the less than 5 GeV/c^2 region by S.S. and O.S. lepton pair type. 131
D.3 $b\bar{b}/c\bar{c}$ invariant mass of the two closest leptons in the less than 5 GeV/c^2 region by lepton pair type. 132

D.4 $b\bar{b}/c\bar{c}$ invariant mass of the two closest leptons in the less than 5 GeV/c^2 region by S.S. and O.S. lepton pair type. 132

D.5 Data invariant mass of the two closest leptons in the less than 5 GeV/c^2 region same sign lepton pair. 133

D.6 $b\bar{b}/c\bar{c}$ invariant mass of the two closest leptons in the less than 5 GeV/c^2 region same sign lepton pair. 133

D.7 Data invariant mass of the two closest leptons in the less than 5 GeV/c^2 region opposite sign lepton pair subtract same sign lepton pair. 134

D.8 $b\bar{b}/c\bar{c}$ invariant mass of the two closest leptons in the less than 5 GeV/c^2 region opposite sign lepton pair subtract same sign lepton pair. 134

E.1 Punzi search of the cut matrix to optimize value $\mathbb{A}$. 137

F.1 Punzi search in $\mu\mu\mu$ channel of the cut matrix to optimize value $\mathbb{A}$. . 139

F.2 Run 63604 Event 108434 event display. 141

F.3 Run 63604 Event 108434 transverse $\eta - \phi$ plot. 141

G.1 Punzi search of the cut matrix to optimize value $\mathbb{A}$. 144

G.2 Punzi search in non-$\mu\mu\mu$ channel of the cut matrix to optimize value $\mathbb{A}$.145

G.3 Punzi search in $\mu\mu\mu$ channel of the cut matrix to optimize value $\mathbb{A}$. . 146

G.4 Distributions of charged multiplicity in the non-$\mu\mu\mu$ channels. 148

Chapter 1

Introduction

> **physics:** science that deals with the structure of matter and the interactions between the fundamental constituents of the observable universe. In the broadest sense physics, which was long called natural philosophy (from the Greek *physikos*), is concerned with all aspects of nature on both the macroscopic and submicroscopic levels. Its scope of study encompasses not only the behaviour of objects under the action of given forces but also the nature and origin of gravitational, electromagnetic, and nuclear force fields. Its ultimate objective is the formulation of a few comprehensive principles that bring together and explain all such disparate phenomena. [1]

A search for simplification of understanding our sophisticated universe is in many senses a search for unification of the four fundamental forces in nature: the electromagnetic, weak, strong, and gravitational forces. In the past several decades physicists have achieved astonishing advances through the establishment of the Standard Model (SM) of elementary particles. The SM has been remarkably successful in describing the strong and electroweak interactions under the gauge group

$SU(3)_C \times SU(2)_L \times U(1)_Y$, and most current experimental results are consistent with the SM [1].

However there are some open questions in the SM which lead us to the assumption that there must be a theory beyond the SM. One possible extension to the SM is the Universal Extra Dimensions (UED) scenario [2]. The UED scenario is an extension of the SM in which all particles live in a $(4+n)$-dimensional spacetime. All of the SM fields propagate into extra compact dimensions of size $R \sim \text{TeV}^{-1}$ (10^{-19} m).

In the UED scenario, momentum conservation in the extra dimensions leads to Kaluza-Klein (KK) number conservation at tree level. Except for zero mode mass contributions, at each level all KK particles have the same masses given by n/R, where the integer mode number n is the KK number. KK number conservation is violated by loop corrections and localized terms at the boundaries. However KK parity remains conserved [2] and leads to the existence of a stable lightest KK particle (LKP). Due to radiative corrections, KK masses are shifted from their tree level values. All higher level KK particles undergo cascade decays to the LKP by emitting soft SM particles. The LKP cannot be detected directly because it interacts with detectors very weakly, but has a mass about R^{-1}, thus resulting in large missing energy. The typical UED events at hadron colliders give leptons plus jets signatures combined with large missing transverse energy.

The current bounds from electroweak data on the size of these extra dimensions are around 300 GeV for Tevatron Run I, and around 400 GeV for Tevatron Run II [2, 3, 4]. Such light KK states may be produced at the Tevatron with center-of-mass energy of 1.8 TeV.

The UED scenario can explain electroweak symmetry breaking [5], the number of

[1] Neutrino oscillation is one exception. In the SM neutrinos are exactly massless. However recent experiments show that neutrinos oscillate between different flavors. This indicates neutrinos have a very small mass and the SM may need to be modified slightly.

[2] Since a translation by the length of the extra dimension leads to an either odd or even state.

generations [6], proton stability [7], and neutrino oscillations [8]. The Higgs doublet is an addition to the SM to break the electroweak symmetry and to explain the origin of mass. It has been shown [9] that the existence of a Higgs doublet is a natural consequence of gauge bosons and fermions propagating in extra dimensions compactified at $\sim$ TeV scale. Studies [10, 11] have shown that the LKP is a good dark matter candidate. All of the above reasons make the UED scenario a compelling model for experimentalists to explore.

In this thesis we study the original UED scenario which does not consider gravity. The LKP is the first level KK photon and is stable. An extension to the original UED scenario [12] studies the KK number violating interactions mediated by gravity, allowing a KK photon to decay to a photon and a KK graviton. The corresponding collider signal consists two hard photons plus large missing energy carried away by the KK gravitons. This "new signal" is outside the scope of this analysis, - interested readers may refer to [12] and the references within.

The outline of this thesis is as follows. In the next chapter we review the relevant theories and the Minimal Universal Extra Dimensions (MUED) scenario. In Chapter 3 we describe the experimental apparatus. We introduce our search strategy in Chapter 4 and describe the data sample selection in Chapter 5. We discuss the SM backgrounds to our analysis in Chapter 6 and the Monte Carlo simulations in Chapter 7. In Chapter 8, 9 and 10 we present the details of the data analysis, uncertainties and the final results. We conclude in Chapter 11 with a brief summary. The appendices include some detailed discussions such as the SM background and MUED Monte Carlo simulations, $b\bar{b}/c\bar{c}$ background Monte Carlo scale factor, results from $\mu\mu\mu$ lepton channel and consideration of charged multiplicity selection requirement.

Chapter 2

Theory

2.1 The Standard Model

The Standard Model is the combination of electroweak theory [13] and quantum chromodynamics [14] to describe elementary particles and their interactions. In the SM the elementary particles are divided into leptons, quarks, and bosons.

The constituents of matter, leptons and quarks, are fermions, with half-integer spin and obeying Fermi-Dirac statistics. The 6 leptons are paired into three families with each family consisting of a charged lepton and its associated neutrino. The 6 quarks are arranged in three families of weak isospin doublets. Both the leptons and the quarks occur in $\mathrm{SU(2)_L}$ doublets. However quarks carry $\mathrm{SU(3)_C}$ color charge whereas leptons do not. Tables 2.1 and 2.2 list the known fermions and their most fundamental properties.[1]

In addition to the fermions, there are particles which mediate the four known forces: the photon (γ) mediates the electromagnetic force, the $W^{\pm}$ and Z^0 mediate the weak force, the gluon (g) mediates the strong force and the graviton (G) mediates

[1]Electric charge Q is given in units of the elementary charge $|e| = 1.609 \times 10^{-19}\ C$.

Table 2.1: List of leptons and their most fundamental properties.

Leptons (Spin= 1/2)			
Particle Name	Symbol	Mass (GeV/c^2)	Q
Electron	e	0.000511	-1
Electron Neutrino	ν_e	$< 3 \times 10^{-9}$	0
Muon	μ	0.106	-1
Muon Neutrino	ν_μ	$< 1.9 \times 10^{-4}$	0
Tau	τ	1.777	-1
Tau Neutrino	ν_τ	$< 1.82 \times 10^{-2}$	0

Table 2.2: List of quarks and their most fundamental properties.

Quarks (Spin= 1/2)			
Particle Name	Symbol	Mass (GeV/c^2)	Q
Up	u	1.5 - 4 $\times 10^{-3}$	2/3
Down	d	4 - 8 $\times 10^{-3}$	-1/3
Charm	c	1.15 - 1.35	2/3
Strange	s	80 - 130 $\times 10^{-3}$	-1/3
Top	t	174	2/3
Bottom	b	4.1 - 4.4	-1/3

gravity. These force carriers are bosons, with integer spin and obeying Bose-Einstein statistics. The strength of each force is given by a corresponding coupling constant α. Table 2.3 lists the bosons and their most fundamental properties.

The leptons, quarks, and bosons described above are the fundamental particles, which means they make up all particles found in nature and are not themselves made up of smaller particles. There is currently no experimental evidence of any further internal structure of these particles. For every particle there is an anti-particle with identical spin and mass but opposite electric charge.

The quarks are confined through the strong force to form bound states called hadrons. Hadrons are classified into two categories by the quark model: quark-

Table 2.3: List of bosons and their most fundamental properties. The electromagnetic force is carried by photons. The weak force is carried by $W^{\pm}$ and Z^0. The strong force is carried by gluons. Gravity has yet to be incorporated in the Standard Model as a quantized theory. The Higgs Boson (H^0) is believed to be the source of electroweak symmetry breaking and mass. The Higgs boson has yet to be discovered.

Bosons					
Name	Mass (GeV/c^2)	Q	Spin	Force Carried	Particles Effected
Photon (γ)	0	0	1	Electromagnetic	All charged
$W^{\pm}$	80.4	$\pm$ 1	1	Weak	Quarks and Leptons
Z^0	91.2	0	1	Weak	Quarks and Leptons
Gluon (g)	0	0	1	Strong	Quarks and Gluons
Graviton (G)	0	0	2	Gravitation	All
Higgs (H^0)	> 114	0	0		All massive particles

antiquark bound states known as mesons, and three quark bound states known as baryons. For example B^0 mesons are made up of $b\bar{d}$ quarks and protons are made up of uud quarks. Mesons are bosons, while baryons are fermions.

The interactions between particles are described by gauge theories in the Standard Model. Gauge theories are applications of quantum field theories with invariance (or symmetry) principles. For example, Quantum Electrodynamics (QED), the gauge theory of electromagnetism, describes the photon mediated interactions of electric charged particles where the electric charge is conserved. Another example, Quantum Chromodynamics (QCD), the gauge theory of the strong force, describes the gluon mediated strong interactions where the color charge is conserved.

The Standard Model as it looks today is a very successful theory. It is consistent with most of the current data, and there is very little experimental evidence for any physics beyond the Standard Model. Despite the success of the SM, it does have a number of theoretical deficiencies which should not occur in a fundamental theory. For example,

- The Standard Model does not contain a quantum description of gravity.

- The SM does not explain why there are three generations of quarks and leptons, nor does it explain the origin of their masses.

- The mass of the top quark is 174 GeV/c^2 while the mass of its isospin partner (the bottom quark) is $\simeq$ 4.1 GeV/c^2. The SM does not explain why the top quark is so much heavier than the other quarks.

- The SM relies on the Higgs mechanism to give particles masses, but so far the Higgs boson has not been observed in experiments.

- The SM cannot explain the hierarchy problem, namely the huge difference between the Planck scale ($\sim 10^{19}$ GeV) [2], the scale associated with gravity and at which all four forces presumably have the same strength) and the electroweak scale (100 GeV to 1 TeV, the scale at which the symmetry between electromagnetism and the weak interaction is broken). [3]

- The SM based extrapolation of gauge couplings measurements shows (Figure 2.1) that the electromagnetic, weak and strong forces do not unify at any energy. Thus the SM (without modification) cannot be a candidate for a unified theory (a theory in which all forces unify), if a unified theory exists.

Those shortcomings of the SM lead to the suspicion that the SM is just a low energy manifestation of a more fundamental theory and that there is a theory beyond the SM. Many have been proposed, such as technicolor [16], grand unified

[2] According to Heisenberg Uncertainty Principle, $\Delta x\ \Delta p \geq \frac{\hbar}{2}$. Note that $\hbar c = 197.327$ MeV fm (PDG 2004). 1 fm = 10^{-15} m. 10^{19} GeV corresponds to $\sim 10^{-35}$ m; 1 TeV corresponds to $\sim 10^{-19}$ m; 1 GeV corresponds to $\sim 10^{-16}$ m.

[3] The strength of the gravitational force is characterized by the Newtonian gravitational constant $G_N = 6.6742 \times 10^{-11}\mathrm{m}^3\mathrm{kg}^{-1}\mathrm{s}^{-2} = 6.707 \times 10^{-39}$ GeV^{-2}; the Planck scale $M_{\mathrm{Planck}} \sim 1/\sqrt{G_N} \sim 10^{19}$ GeV. The strength of the electroweak force is characterized by the Fermi coupling constant $G_F = 1.166 \times 10^{-5}$ GeV^{-2}; the electroweak scale $m_{ew} \sim 1/\sqrt{G_F} \sim 246$ GeV.

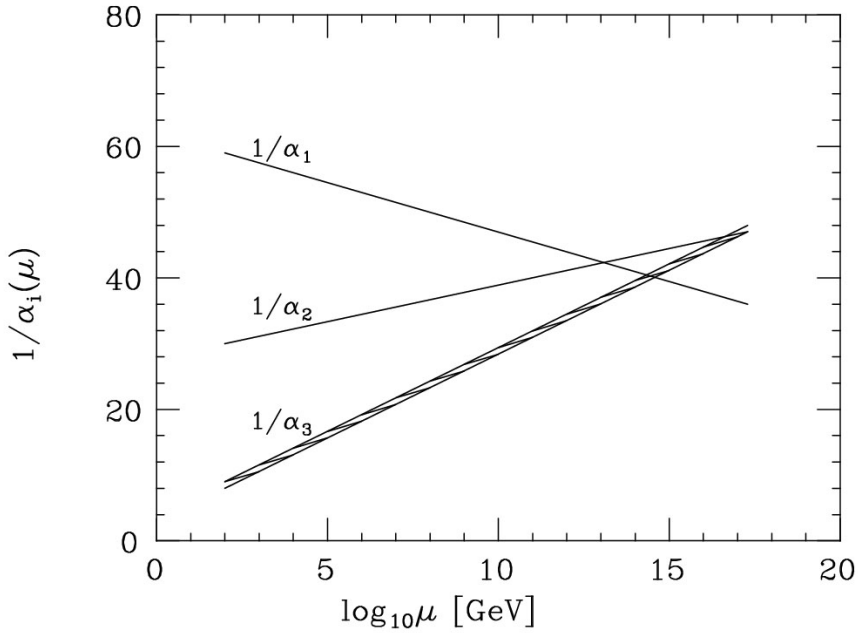

Figure 2.1: The SM based extrapolation of gauge couplings measurements. α_1 is the $U(1)_Y$ coupling constant, α_2 is the $SU(2)_W$ coupling constant and α_3 is the $SU(3)_C$ coupling constant. These coupling constants do not meet at a single point. Adapted from [15].

theories [17], supersymmetry (SUSY) [18], and extra dimensions [19]. Each of these models solves some of the above problems, but up to now there is no experimental evidence for any of these models.

SUSY and extra dimensions are among the most promising theories beyond the SM. In the next section we will describe extra dimensions. Here we give a brief review of SUSY. SUSY relates fermions and bosons by transforming fundamental particles into "superpartners" which differ from the original particles by 1/2 unit of spin, while keeping all other quantum numbers the same. In SUSY the hierarchy problem manifests itself as the difference between the Higgs boson mass and the Planck mass. One can show that two identical one-loop diagrams in which one diagram has a fermion and the other has a boson will cancel out if their masses are identical; the divergences are logarithmic if these masses are different, and can be removed via

renormalization. A full explanation can be found in [18]. Stabilization of the Higgs and unification of α_1, α_2, and α_3 place a mass limit of superpartners in the range of ~ 1 TeV.

2.2 Extra Dimensions

The number of dimensions is a measure of the number of degrees of freedom available for movement in space. It can also be thought of as the number of coordinates necessary to determine the location of an object. Our perceptions tell us that we live in a universe with three dimensions of space and one dimension of time. The inverse square laws such as Newton's law of gravitational force and Coulomb's law of electric force observed in the experiments are also evidence for three spatial dimensions. However extra dimensions are not only possible, but can also solve some of the puzzles present in the four-dimensional world. In fact string theory, which incorporates both gravity and gauge theories, requires six or seven extra spatial dimensions. The extra dimensions are not necessarily to be very small either, - in some scenarios they can be as large as 1 mm and still consistent with our current observations.

Theorists have proposed many possibilities for theories with extra dimensions, and a good starting point for further reading on extra dimensions can be found in [19, 20, 21] and the references within. So far no complete and consistent extra dimension model has been constructed, and the energy scale required to probe the extra dimensions differs in these models. For example in the original Kaluza-Klein theory of extra spacetime dimensions, the size of the extra dimension is near the Planck length; yet many recent models propose extra dimensions that are much larger. In this section we briefly describe the original Kaluza-Klein theory, then review three extra dimensions scenarios which are within the reach of the Tevatron

and the LHC: the large extra dimensions, the warped extra dimensions, and the universal extra dimensions scenarios. The current collider searches for the large extra dimensions and the warped extra dimensions at the Tevatron are summarized in [22]. This analysis is the first UED search in the multi-lepton channel performed at the Tevatron.

The differences of various extra dimensions scenarios come from different assumptions of how the fermions and bosons are confined in the spacetime. Most modern extra dimensions scenarios use a "brane"-world picture: we call our observed 3-dimensional space a 3-brane ("wall") [4], and this 3-brane is embedded in a higher D-dimensional spacetime ("bulk"), where $D = 3 + 1 + \delta$, and δ is the number of extra spatial dimensions which are orthogonal to our 3-brane.

2.2.1 Kaluza-Klein Theory of Extra Spacetime Dimensions

The first application of extra spacetime dimensions to fundamental physics dated back to the early twentieth century by Gunnar Nordström, Theodor Kaluza and Oskar Klein, in their pioneering work of searching for a possible means of unifying electromagnetism with gravity, the two fundamental forces known at that time.

In Einstein's theory of special relativity time t is treated as a fourth dimension, together with the space coordinates they are collectively denoted x^μ (here we use Greek letters such as μ, ν to denote coordinates 0,1,2,3). In Einstein's theory of general relativity, a gravitational field with two indices, $g_{\mu\nu}(x)$, which also has the geometrical interpretation of a metric tensor, was introduced. In a four-dimensional

[4] A n-brane is a brane with n spatial dimensions. For example a 1-brane is a string, a 2-brane is a membrane.

spacetime, the infinitesimal distance between two points is:

$$ds^2 = g_{\mu\nu}(x)\ dx^\mu dx^\nu \tag{2.1}$$

Inspired by Maxwell's unification of electricity and magnetism, Nordström [23] in 1914 and Kaluza [24] in 1921 independently proposed a way of unifying electromagnetism with gravity by postulating a fifth dimension. Kaluza applied Einstein's general theory of relativity to a five-dimensional spacetime manifold [5]. The postulated fifth coordinate together with the first four coordinates are denoted collectively x^M (here we use Roman letters such as M, N to denote coordinates 0,1,2,3,4). In a five-dimensional spacetime, the line element becomes:

$$d\hat{s}^2 = \hat{g}_{MN}(x)\ dx^M dx^N \tag{2.2}$$

where

$$\hat{g}_{MN} = \begin{pmatrix} g_{\mu\nu} + \kappa^2\phi^2 A_\mu A_\nu & \kappa\phi^2 A_\mu \\ \kappa\phi^2 A_\nu & \phi^2 \end{pmatrix} \tag{2.3}$$

$g_{\mu\nu}$ describes Einstein's gravitational field, A_μ describes Maxwell's electromagnetic field, ϕ is a scalar field and κ is a constant ($\kappa \equiv 4\sqrt{\pi G_N}$, where G_N is the gravitational constant in four dimensions); $g_{\mu\nu}$, A_μ, and ϕ transform respectively as a tensor, a vector and a scalar under four-dimensional general coordinate transformations.

Both Nordström and Kaluza assumed that all derivatives with respect to the

[5] In physics a manifold can be considered as a smooth multi-dimensional space with no special points or boundaries.

fifth coordinate vanish (so called "cylinder condition") so that physics depends on the first four coordinates, to explain why no fifth dimension had been observed by us in nature.

In 1926 Klein [25] applied Kaluza's theory to quantum theory. He showed that Kaluza's cylinder condition would arise naturally if the fifth coordinate was a length-like one and had two properties: (1) a circular topology (S^1); and (2) a "compactified"[6] scale. The space topology is then the product of a four-dimensional space and a circle: $R^4 \times S^1$, and we can envisage such topology as a tiny circle at each point in four-dimensional spacetime.

Under property (1) any five-dimensional physical field $f(x, y)$ (where $x = (x^0, x^1, x^2, x^3)$ denotes coordinates on R^4, and y denotes the coordinate on S^1) becomes periodic, as $f(x, y) = f(x, y + 2\pi R)$, where R is the radius (scale parameter) of the fifth dimension. Therefore all the fields can be expanded in Fourier series along S^1 (we set $0 \leq \frac{y}{R} \leq 2\pi$):

$$g_{\mu\nu}(x, y) = \frac{1}{\sqrt{2\pi R}} \sum_{n\in\mathbb{Z}} \mathrm{e}^{in\frac{y}{R}} g^{(n)}_{\mu\nu}(x) \ , \tag{2.4}$$

$$A_\mu(x, y) = \frac{1}{\sqrt{2\pi R}} \sum_{n\in\mathbb{Z}} \mathrm{e}^{in\frac{y}{R}} A^{(n)}_\mu(x) \ , \tag{2.5}$$

$$\phi(x, y) = \frac{1}{\sqrt{2\pi R}} \sum_{n\in\mathbb{Z}} \mathrm{e}^{in\frac{y}{R}} \phi^{(n)}(x) \ , \tag{2.6}$$

The superscript $^{(n)}$ refers to the nth Fourier mode.

Considering the action for a five-dimensional complex Klein-Gordon quantum

[6] A compact dimension is curled up on itself and is very small. Anything travelling along this dimension's direction would return to its original position instantaneously. The extra dimension is so small (near the Planck length) in the original Kaluza-Klein theory that it cannot be observed by conventional methods. However a few recent models of extra dimensions with radius of order 1 TeV^{-1} could be observed at the Tevatron or the LHC.

field $\phi(x,y)$ of mass m_0:

$$
\begin{aligned}
S &= \int_0^{2\pi R} dy \int d^4x \, \left\{ \partial_M \phi(x,y)^* \partial^M \phi(x,y) - m_0^2 \phi(x,y)^* \phi(x,y) \right\} && (2.7) \\
&= \int_0^{2\pi R} dy \int d^4x \, \frac{1}{2\pi R} \left\{ \sum_{mn} \partial_\mu \phi^{(m)}(x)^* \, \partial^\mu \phi^{(n)}(x) \, e^{i(n-m)y/R} \right. \\
&\quad - \sum_{mn} (-im/R)(in/R) \, \phi^{(m)}(x)^* \, \phi^{(n)}(x) \, e^{i(n-m)y/R} \\
&\quad \left. - m_0^2 \sum_{mn} \phi^{(m)}(x)^* \, \phi^{(n)}(x) \, e^{i(n-m)y/R} \right\} && (2.8) \\
&= \int d^4x \left\{ \sum_n \partial_\mu \phi^{(n)}(x)^* \partial^\mu \phi^{(n)}(x) - \sum_n \left[m_0^2 + \frac{n^2}{R^2} \right] \phi^{(n)}(x)^* \phi^{(n)}(x) \right\} && (2.9)
\end{aligned}
$$

The last step uses the orthogonal property of different modes in the Fourier expansion:

$$
\int_0^{2\pi R} dy \, e^{i(n-m)y/R} = 2\pi R \, \delta_{mn} \tag{2.10}
$$

We see that the effective 4-D action corresponding to a 5-D action of mass m_0 is an infinite tower of 4-D Klein-Gordon fields with masses given by

$$
m_n^2 = m_0^2 + \frac{n^2}{R^2} \tag{2.11}
$$

where the integer number n is the KK number.

Similar to a quantum particle in a box, the momentum in the fifth dimension is quantized in units of $1/R$. Thus equation (2.11) is equivalent to $m_n^2 = m_0^2 + p_5^2$, where p_5 is the momentum in the fifth dimension. The fifth dimension leads to an infinite tower of Kaluza-Klein (KK) states, which is labelled by KK number n for each individual KK excitation. Higher mode excitations correspond to higher momentum modes in the extra dimension, thus higher KK mass in our effective 4-D

theory.

In the original KK theory the fifth dimension is compact and homogeneous, and all forces and particles propagate in this dimension. The compactness of the fifth dimension ensures that momentum in the fifth dimension of even the $n = 1$ modes will be too large to be observed [7]. Hence KK theory explains why only the $n = 0$ modes will be observable, and the low energy (e.g. below TeV scale) physics is effectively four-dimensional. However in the late 1990's, theoretical physicists began to wonder what the TeV physics world would look like if the 10^{19} GeV Planck scale is not the fundamental gravitational scale and the scale of extra dimensions is much larger than the Planck length of 10^{-35} m. The results are a series of scenarios of extra dimensions which propose many new possibilities of physics beyond the Standard Model.

2.2.2 Large Extra Dimensions - the ADD Model

Large Extra Dimensions refers to the scenario proposed by Arkani-Hamed, Dimopoulos and Dvali [26]. In this scenario, gravitons propagate in the bulk while all of the SM fields are localized to the 3-brane, as illustrated in Figure 2.2.

The ADD model is motivated by the hierarchy problem and provides a framework for solving the hierarchy problem without relying on supersymmetry. According to the ADD model, the large difference between the gravitational scale and the electroweak scale is due to a geometrical suppression of the gravitational lines of flux by a factor proportional to the volume of the extra dimensions:

$$M_{\text{Planck}}^2 = M_*^{n+2}\, R^n \quad , \tag{2.12}$$

[7] The extra dimension is traditionally considered to be of order of the Planck scale, which means the contribution from momenta of KK excitations to 4-D effective masses is about 10^{19} GeV.

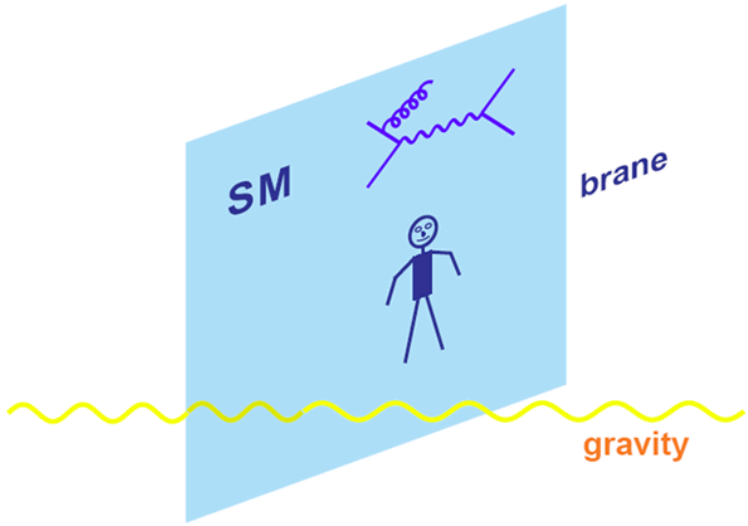

Figure 2.2: Illustration of the Large Extra Dimensions - the ADD Model.

where M_{Planck} is the Planck scale ($\sim 10^{19}$ GeV), M_* is the fundamental gravitational scale (or the Planck scale in higher dimensions), R is the scale of the extra dimensions, and n is the number of extra dimensions (n is 2 in the original ADD model, and extended up to 6 in many variations of the ADD model).

Newton's law states that the gravitational potential falls as $V(r) \sim 1/r$. Extra dimensions weaken the potential as $V(r) \sim 1/r^{(n+1)}$ when $r < R$ due to gravity propagating in the extra dimensions. In the ADD model M_* is supposed to be of order $\sim$ 1 TeV. For a $n = 1$ scenario, equation (2.12) yields $R \sim 10^{13}$ m. This scenario is ruled out because there is no observed deviation from Newton's Law at such a large scale. For $n \geq 2$ scenarios, R can be as large as 1 mm, and these scenarios cannot be ruled out since no tests of gravity has been carried out at distances much lower than 1 millimeter [27, 28]. Thus the observed hierarchy between the Planck scale and the electroweak scale is possibly due to the largeness of the scale of extra dimensions.

The consequence of these large extra dimensions is that there is a Kaluza-Klein

tower of graviton modes, where the zero mode is the standard 4-D massless graviton, and the higher KK modes are massive spin 2 particles. These massive particles can be emitted or exchanged along with the SM gauge bosons, thus can be detected at the Tevatron or the LHC. The search for Large Extra Dimensions at the CDF and D0 has excluded the fundamental gravitational scale below 1.0 TeV for 2 extra dimensions at 95% confidence level [29, 30].

2.2.3 Warped Extra Dimensions - the RS Model

Warped Extra Dimensions refers to the scenario proposed by Randall and Sundrum [31]. In this scenario there is one extra spatial dimension, and the five-dimensional geometry is "warped" by the presence of branes. There are several variations of the RS model, and here we refer to RS-1, the original RS model. In this model the fifth dimension y is a line interval ($y \in [0, 1]$) with the "Planck brane" at one end ($y = 0$) and the "TeV brane" at the other end ($y = 1$). It is also assumed that the SM particles live on the TeV brane, see Figure 2.3.

The 5-D line element is

$$ds^2 = a^2(y)\eta_{\mu\nu}dx^\mu dx^\nu + b^2 dy^2 \tag{2.13}$$

where $a(y) = e^{-kby}$ is the warp factor, b is the size of the fifth dimension, and k is determined by the 5-D cosmological constant Λ and the 5-D gravitational scale M: $k = (-\Lambda/6M^3)^{1/2}$.

M_{Planck} is related to M by:

$$M^2_{\text{Planck}} = \frac{M^3}{k}(1 - e^{-2kb}). \tag{2.14}$$

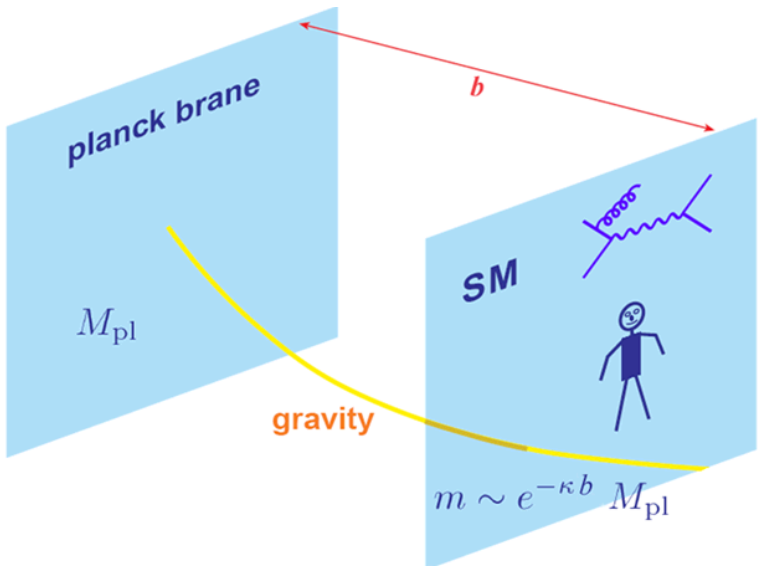

Figure 2.3: Illustration of the Warped Extra Dimensions - the RS Model.

Randall and Sundrum assume that the Planck brane has positive tension σ and the TeV brane has negative tension $-\sigma$ (tension σ is the 4-D energy density, which has the same form as a 4-D cosmological constant). Particles on the Planck brane have masses of the order the Planck mass $M_{\rm Planck}$, while particles on the TeV brane have their masses suppressed by the warp factor e^{-kb}. By adjusting b, so that $kb \sim 36$, the masses of particles on the TeV brane will be in the TeV scale regardless of the scale of other parameters (Λ, σ, k, and M can be of the order of $M_{\rm Planck}$).

Similar with the ADD model, the phenomenology of the RS model gives rise to massive KK modes of the graviton, with their mass splittings on the order of $\sim$ TeV as measured on the TeV brane. The phenomenological differences between the RS model and the ADD model are: (i) the mass spectrum of KK gravitons in the RS model is discrete and unevenly spaced, while in the ADD model it is evenly spaced and effectively a continuous spectrum, and (ii) in the RS model each resonance has a coupling strength of 1/TeV, while in the ADD model the collective strength of all KK graviton modes give a coupling strength of 1/TeV.

2.2.4 Universal Extra Dimensions - the ACD Model

Universal Extra Dimensions refers to the scenario proposed by Appelquist, Cheng, and Dobrescu [2]. In the Universal Extra Dimensions (UED) scenario, all of the Standard Model fields are allowed to propagate in the bulk. The extra dimensions are compactified with size $R \sim \text{TeV}^{-1}$. Unlike the ADD model or the RS model, in the ACD model every SM particle has heavy KK partners similar to the case of Minimal Supersymmetric Model (MSSM). In addition, the UED model is not motivated to explain the hierarchy problem. Instead it was originally proposed as a model for electroweak symmetry breaking [5].

The UED model has been studied extensively with one or two extra dimensions. The most attractive feature of the UED scenario with one extra dimension (the Minimal Universal Extra Dimensions, MUED) is that it is very predictive if we assume all boundary terms vanish at the cutoff energy scale $\Lambda > R^{-1}$. Another feature of the MUED scenario is the existence of the stable lightest KK particle (LKP), which is a good dark matter candidate [10, 11]. On the other hand, the UED scenario with two extra dimensions can constrain the number of fermion generations [6] and incorporate gravity as well as explain proton stability and neutrino oscillations [7, 8].

The typical UED events at hadron colliders give leptons plus jets signatures combined with large missing transverse energy ($\not{E}_T$). The current bounds from electroweak data on the size of these extra dimensions are around 300 GeV for Tevatron Run I, and around 400 GeV for Tevatron Run II [2, 3, 4]. Such light KK states can be produced at the Tevatron or the LHC.

2.3 The Minimal Universal Extra Dimensions Scenario

The Minimal Universal Extra Dimensions (MUED) scenario is the simplest UED scenario in which all of the SM fields propagate in one extra dimension compactified on a S^1/Z_2 orbifold [8], where Z_2 is the reflection symmetry $y \to -y$ (note that this is equivalent to $y \to \pi R - y$ as a result of the S^1/Z_2 orbifold).

At tree level KK number n is a good quantum number and is conserved in all interactions and decays. The Feynman rules for the KK modes are derived in Ref. [32, 33]. The orbifold fixed points break translational symmetry in the fifth dimension, therefore momentum in the y direction (thus also the KK number) is no longer conserved. However, a translation by πR in the y direction remains a symmetry of the orbifold. One can show that under this transformation the $n =$ even KK modes are invariant while the $n =$ odd KK modes change sign[9]. Therefore, KK parity $(-1)^n$ is still a good symmetry. This symmetry implies that the lightest KK particle (LKP) is stable and LKPs can only be pair produced. KK parity conservation plays an analogous role to R-parity conservation in supersymmetry: R-parity conservation implies that the lightest supersymmetric particle (LSP) is stable and LSPs can only be pair produced.

In this section we first discuss the boundary conditions on S^1/Z_2 orbifold, then review the radiative corrections to the KK mass spectrum, and compare MUED with MSSM in the end.

Throughout this thesis, we use the following notations, adapted from [34]: upper

[8] An orbifold is a manifold with special points such as endpoints or boundaries. It is often constructed by imposing a discrete symmetry Γ on a manifold K. An orbifold is the resulting quotient space K/Γ. The S^1/Z_2 orbifold is equivalent to a line segment between 0 to πR.

[9] KK parity is the symmetry of the reflection around the line segment center at $y = \pi R/2$ combined with changing signs for all odd fields.

case letters denote SU(2)-doublets; lower case letters denote SU(2)-singlets; subscript $_n$ denotes the $n-th$ KK mode; subscript $_L$ denotes left-handedness; subscript $_R$ denotes right-handedness, e.g. Q_1 denotes $n = 1$ mode SU(2)-doublet quarks, q_1 denotes $n = 1$ mode SU(2)-singlet quarks.

2.3.1 Kaluza-Klein Modes Expansion on S^1/Z_2 Orbifold

We now consider the Kaluza-Klein modes expansion for a scalar, a vector, and a spinor in five dimensions with the fifth dimension compactified on a S^1/Z_2 orbifold.

A 5-D scalar field ϕ on the S^1/Z_2 orbifold is either even or odd under $\mathcal{P}_5 : y \to -y$:

$$\left.\begin{aligned} \partial_5 \phi_+ &= 0 \\ \phi_- &= 0 \end{aligned}\right\} \quad \text{at } y = 0, \pi R. \tag{2.15}$$

The associated KK expansions are

$$\begin{aligned} \phi_+(x,y) &= \frac{1}{\sqrt{\pi R}}\phi_+^{(0)}(x) + \frac{\sqrt{2}}{\sqrt{\pi R}}\sum_{n=1}^{\infty}\phi_+^{(n)}(x)\cos\frac{ny}{R}, \\ \phi_-(x,y) &= \qquad\qquad\qquad \frac{\sqrt{2}}{\sqrt{\pi R}}\sum_{n=1}^{\infty}\phi_-^{(n)}(x)\sin\frac{ny}{R}, \end{aligned} \tag{2.16}$$

For a 5-D vector field A^M on the S^1/Z_2 orbifold, the first four components are even under $\mathcal{P}_5 : y \to -y$, while the fifth component is odd ($A^\mu \to A^\mu$, $A^5 \to -A^5$ for $\mathcal{P}_5 : y \to -y$)

$$\left.\begin{aligned} \partial_5 A^\mu &= 0 \\ A^5 &= 0 \end{aligned}\right\} \quad \text{at } y = 0, \pi R. \tag{2.17}$$

The associated KK expansion are

$$\begin{aligned} A_\mu(x,y) &= \frac{1}{\sqrt{\pi R}} A_\mu^{(0)}(x) + \frac{\sqrt{2}}{\sqrt{\pi R}} \sum_{n=1}^{\infty} A_\mu^{(n)}(x) \cos\frac{ny}{R}, \\ A_5(x,y) &= \qquad\qquad\qquad\qquad \frac{\sqrt{2}}{\sqrt{\pi R}} \sum_{n=1}^{\infty} A_5^{(n)}(x) \sin\frac{ny}{R}. \end{aligned} \tag{2.18}$$

For a 5-D Dirac spinor $\psi = \psi_L + \psi_R$, one can show that only one of the chiralities has zero modes by solving 5-D Dirac equation on an interval (S^1/Z_2 orbifold), thus the 4-D chirality is a natural consequence of the orbifold boundary conditions. Note that (1) any 5-D fermion includes a left-handed component and a right-handed component; and (2) an even mode has a zero mode while an odd mode does not have a zero mode. Thus if the left-handed fermion is odd (no zero mode) then the right-handed component must be even (has a zero mode); if the right-handed fermion is odd (no zero mode), then the left-handed component must be even (has a zero mode). The orbifold boundary conditions can thus be imposed as:

$$\left.\begin{aligned} \partial_5 \psi_{+R} &= 0 \\ \psi_{+L} &= 0 \end{aligned}\right\} \quad \text{at } y = 0, \pi R \quad \text{or} \quad \left.\begin{aligned} \partial_5 \psi_{-L} &= 0 \\ \psi_{-R} &= 0 \end{aligned}\right\} \quad \text{at } y = 0, \pi R. \tag{2.19}$$

The associated KK expansion are

$$\begin{aligned} \psi_+(x,y) &= \frac{1}{\sqrt{\pi R}} \psi_R^{(0)}(x) + \frac{\sqrt{2}}{\sqrt{\pi R}} \sum_{n=1}^{\infty} \left(\psi_R^{(n)}(x) \cos\frac{ny}{R} + \psi_L^{(n)}(x) \sin\frac{ny}{R} \right), \\ \psi_-(x,y) &= \frac{1}{\sqrt{\pi R}} \psi_L^{(0)}(x) + \frac{\sqrt{2}}{\sqrt{\pi R}} \sum_{n=1}^{\infty} \left(\psi_L^{(n)}(x) \cos\frac{ny}{R} + \psi_R^{(n)}(x) \sin\frac{ny}{R} \right). \end{aligned} \tag{2.20}$$

Equation (2.20) shows that the zero mode is either left-handed or right-handed while the higher modes contain both left-handed and right-handed chirality.

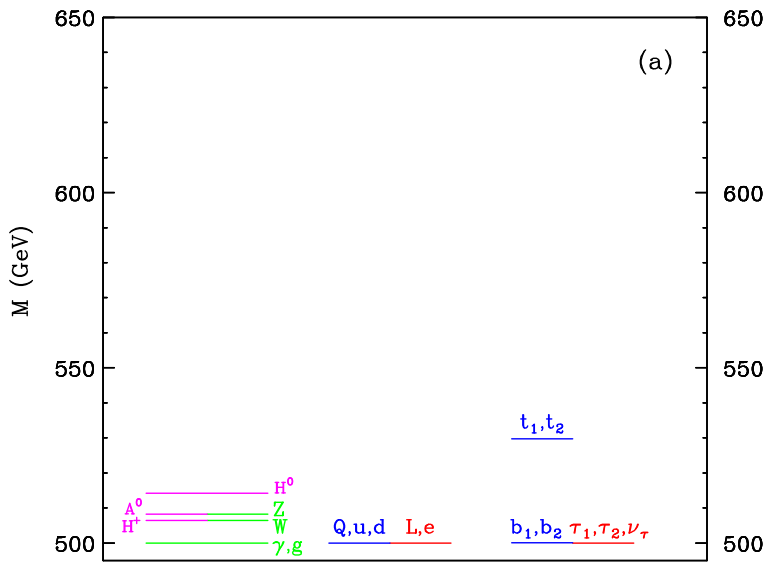

Figure 2.4: The mass spectrum of the $n = 1$ modes at tree level for $R^{-1} = 500$ GeV, $\Lambda R = 20$ and $m_h = 120$ GeV. Ref. [35]

2.3.2 MUED Mass Spectrum

The tree-level mass of the n-th KK mode satisfies:

$$m_n^2 = m_0^2 + \frac{n^2}{R^2}, \tag{2.21}$$

where R is the radius of the compact dimension, m_0 is the zero mode (Standard Model) mass and n is the KK number which corresponds to the quantized momentum p_5 in the compact dimension. Except for zero mode mass contributions, at each level all KK modes would be degenerate in mass, with masses given by n/R, as shown in Figure 2.4.

The most important contributions to the splittings in the KK mass spectrum are from radiative loop corrections [10], which comprise both bulk terms and boundary terms.

[10]Radiative corrections are virtual contributions, e.g. the type where a Higgs dissociates into a virtual pair of $t\bar{t}$ which then recombines to reform the Higgs.

The bulk terms are radiative corrections due to fields propagating along the fifth dimension, which are finite - the corrections to the KK mass are proportional to $k/16\pi^4 R^2$ [35], where k is the contribution of the KK fields inside the loop and is different for different particles. Thus the KK mass degeneracy is lifted.

The boundary terms are loop effects that are localized on the fixed points of the S_1/Z_2 orbifold, which are logarithmically divergent - thus it's necessary to introduce a cutoff scale Λ, and make the assumption that all boundary terms are negligible at scale $\Lambda > R^{-1}$. The corrections to the KK mass are proportional to $m_n(k/16\pi^2)\ln(\Lambda^2/\mu^2)$ [35], where μ is the energy scale where the corrections are calculated. Thus the KK mass degeneracy is further lifted.

Assuming all boundary terms vanish at some cutoff scale $\Lambda > R^{-1}$, the MUED scenario has three free parameters: $\{R, \Lambda, m_h\}$, where m_h is the mass of the SM Higgs boson, which cannot be predicted within the UED scenario.

Electroweak symmetry breaking introduces mixing among the states, causing non-negligible tree-level contributions to the KK mass spectrum for certain fields. This effect is important for the KK modes of the top quark, the Higgs boson, photon and Z. Ref. [35] calculated the first few KK levels "Weinberg" mixing angle θ_n versus (a) R^{-1}, for fixed $\Lambda R = 20$; and (b) ΛR, for fixed $R^{-1} = 300$ GeV as shown in Figure 2.5. The mixing angle is different from the Standard Model Weinberg electroweak mixing angle θ_W [11] due to radiative corrections to the masses of gauge bosons.

The corrections to the KK spectrum calculated by Cheng, Matchev and Schmaltz [35] using the one-loop leading log approximation are listed in Appendix A. The one-

[11] In the Standard Model the Weinberg mixing angle θ_W gives the relationship between the strengths of the electromagnetic and weak interactions, as well as the relationship between the masses of the gauge bosons W and Z: $\sin^2\theta_{\mathrm{W}} = \frac{\pi\alpha}{\sqrt{2}\mathrm{G_F}}\frac{1}{\mathrm{m_W^2}} = 1 - \frac{\mathrm{m_W^2}}{\mathrm{m_Z^2}} = 0.23$, where α is the fine structure constant and $\mathrm{G_F}$ is the Fermi coupling constant.

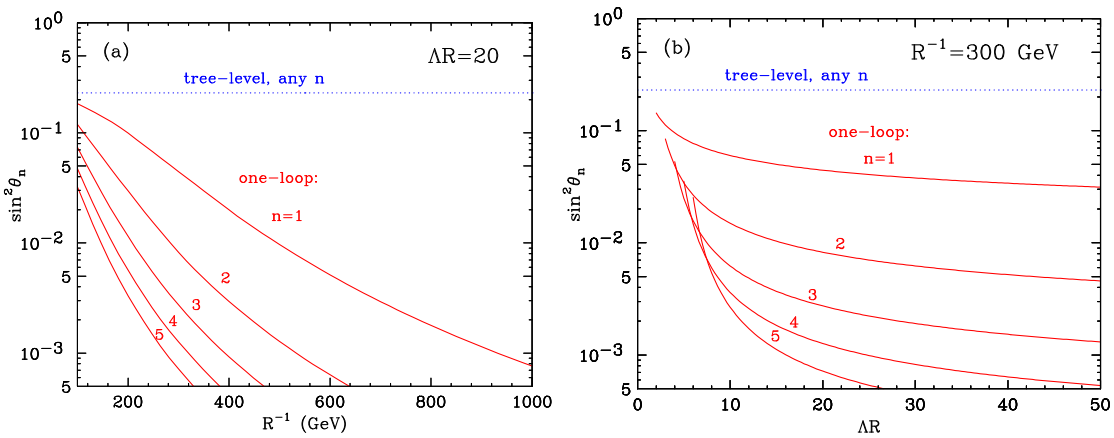

Figure 2.5: The first few KK levels "Weinberg" angle θ_n versus (a) R^{-1}, for fixed $\Lambda R = 20$ and (b) ΛR, for fixed $R^{-1} = 300$ GeV. Adapted from Ref. [35].

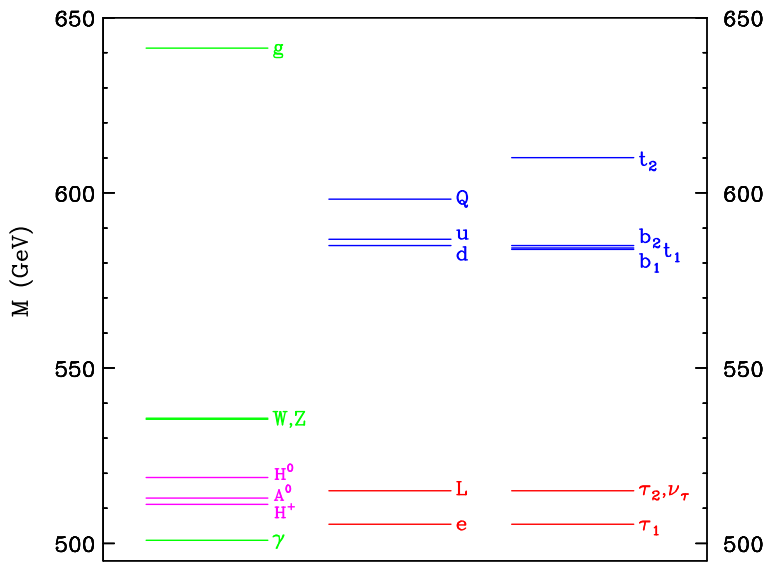

Figure 2.6: One-loop corrected mass spectrum of the $n = 1$ modes for $R^{-1} = 500$ GeV, $\Lambda R = 20$ and $m_h = 120$ GeV. Ref. [35]

loop corrected mass spectrum of the $n = 1$ KK modes is shown in Figure 2.6. The dependence of the $n = 1$ KK modes mass splittings on the cutoff scale Λ is shown in Figure 2.7. The corrections to the masses give rise to the pattern $m_{g_n} > m_{Q_n} > m_{q_n} > m_{\mathrm{W}_n} \sim m_{\mathrm{Z}_n} > m_{L_n} > m_{\ell_n} > m_{\gamma_n}$ with γ_1 being the lightest KK particle. γ_1 is a mixture of the $n = 1$ KK mode B_1 of the $\mathrm{U}(1)_Y$ gauge boson B and the $n = 1$ KK mode W_1^0 of the $\mathrm{SU}(2)_W$ gauge boson W^3.

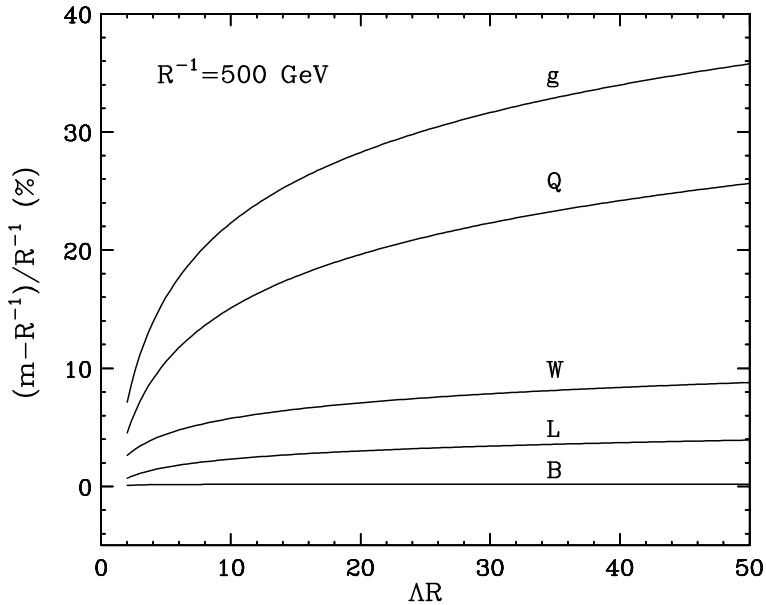

Figure 2.7: Radiative corrections (in %) to the spectrum of the $n = 1$ modes (gluon, quark, gauge boson W, lepton, gauge boson B) for $R^{-1} = 500$ GeV, versus ΛR. Ref. [34]

The mass splitting between the KK quarks and the LKP, as well as the splitting between the weak KK gauge bosons and the LKP is shown as a function of $1/R$ in Figure 2.8 [36].

Note that the KK W and KK Z are virtually degenerate in mass, and that $m_{\mathrm{W}}, m_{\mathrm{Z}} < m_q, m_Q$, which means the KK W and KK Z can only have leptonic decays, and result in a very clean signature for our search.

The mass splittings among the $n = 1$ KK modes are large enough for the prompt decay of a heavier $n = 1$ KK mode to a lighter $n = 1$ KK mode. However the subsequent detections of the soft SM particles emitted from these decays are not trivial since the mass spectrum is still quite degenerate.

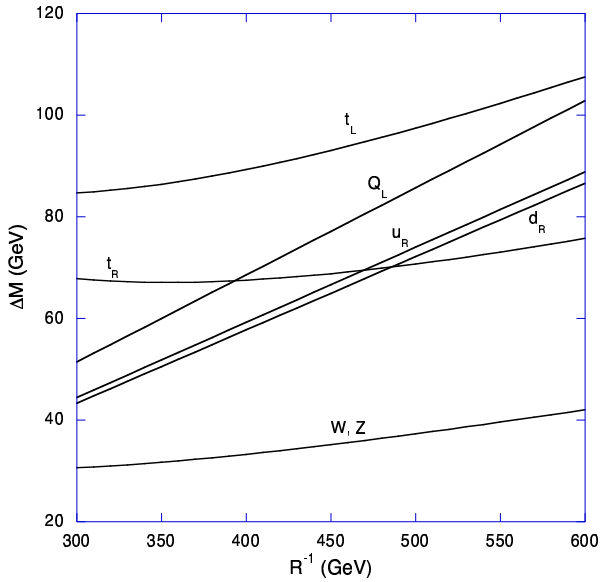

Figure 2.8: The mass splitting between KK quarks and the LKP γ_1, as well as the splitting between the KK gauge bosons and the LKP, as a function of $1/R$ for $\Lambda R = 20$. Here Q_L stands for all isodoublet KK quarks except top, u_R stands for up and charm isosinglet KK quarks, and d_R stands for down, strange and bottom isosinglet KK quarks. Ref. [36]

2.3.3 Comparison of MSSM and MUED

MSSM and MUED are the simplest models of SUSY and UED respectively. MSSM assumes that all particles carry a conserved multiplicative quantum number, called R-parity, which is +1 for ordinary particles and -1 for superpartners. Thus SUSY particles must be produced in pairs, and that there is a lightest supersymmetric particle (LSP) which is stable. The LSPs are neutral and weakly interacting, and would not interact with the detector thus lead to missing energy. There are many similarities between MSSM and MUED, yet there are also several differences. Table 2.4 is the comparison of MSSM and MUED.

Table 2.4: Comparison of MSSM and MUED

	MSSM	MUED
SM partners	sparticles	KK partners
Masses of SM partners	~ 1 TeV	$\sqrt{m_0^2 + n^2/R^2}$ ($R^{-1} \sim 1$ TeV)
Spins compared with SM particles	differing by 1/2	identical
Couplings compared with SM particles	identical	identical
Higher level excitations	no	higher KK modes exist
Parity conservation	R-Parity	KK Parity
Lightest stable particle	LSP	LKP

Chapter 3

Apparatus

The apparatus employed in this study resides at the Fermi National Accelerator Laboratory (FNAL, Fermilab) which is located in the western suburbs of Chicago, Illinois, covering about 6,700 acres of land. The collisions of protons and antiprotons occur in a superconducting collider, called the Tevatron, operating at a center-of-mass energy of $\sqrt{s} = 1.8$ TeV. Protons and antiprotons circulate in opposite directions, and observation of the collisions is achieved at two sites along the collider ring - CDF (Collider Detector at Fermilab) and D0.

The run of Tevatron from year 1992 to 1996 is called Run I. There have been many important results in Run I, among which the most prominent one was the discovery of the top quark in 1994. This analysis uses data taken during the period from year 1994 to 1996 (also known as Run IB).

The Tevatron and the CDF detector are described in detail in [37, 38, 39]. Here we will briefly describe the general features and capabilities of the apparatus as well as details of the detector components relevant to the analysis, as they were configured during the Run IB period.

3.1 The Tevatron

The Tevatron is a superconducting synchrotron which can accelerate protons and antiprotons to 900 GeV. The clockwise revolving beam of protons and the counter-clockwise revolving beam of antiprotons collide head on at a center-of-mass energy of $\sqrt{s} = 1.8$ TeV. A schematic diagram of the Tevatron and its associated accelerators is shown in Figure 3.1.

A series of steps are needed to accelerate protons and antiprotons to energies of 900 GeV. The Cockcroft-Walton [40] electrostatic accelerator provides the first stage of acceleration. Inside this giant cylindrical capacitor, hydrogen gas atoms are ionized by adding an additional electron to form H^-. The negative ions are then attracted to a positive voltage and accelerated to an energy of 750 keV. The H^- ions leaving the Cockcroft-Walton are injected into a linear accelerator (Linac). The Linac is a 150 m long series of radio-frequency (RF) cavities. The RF cavities produce an electric field that rapidly changes direction. The cavities increase in length in the direction of acceleration, thus the H^- ions always experience an accelerating field while in the gaps between the cavities and are shielded within the cavities as electric field change direction. The H^- ions are accelerated to a kinetic energy of 400 MeV ($\sim$ 70% of the speed of light) at the exit of the Linac.

The H^- ions leaving the Linac enter the Booster, a small rapid cycling synchrotron 150 m in diameter. It is here that the H^- ions lose their two electrons as they pass through a thin carbon foil (only 1.5 μm thick), leaving only the protons. The protons travel around the Booster 20,000 times, taking only 1/30 second altogether, and leave the Booster with kinetic energy of 8 GeV ($\sim$ 99% of the speed of light) and are injected into the Main Ring. The Main Ring is another proton synchrotron, which is 1 km in radius. The main ring uses conventional dipole mag-

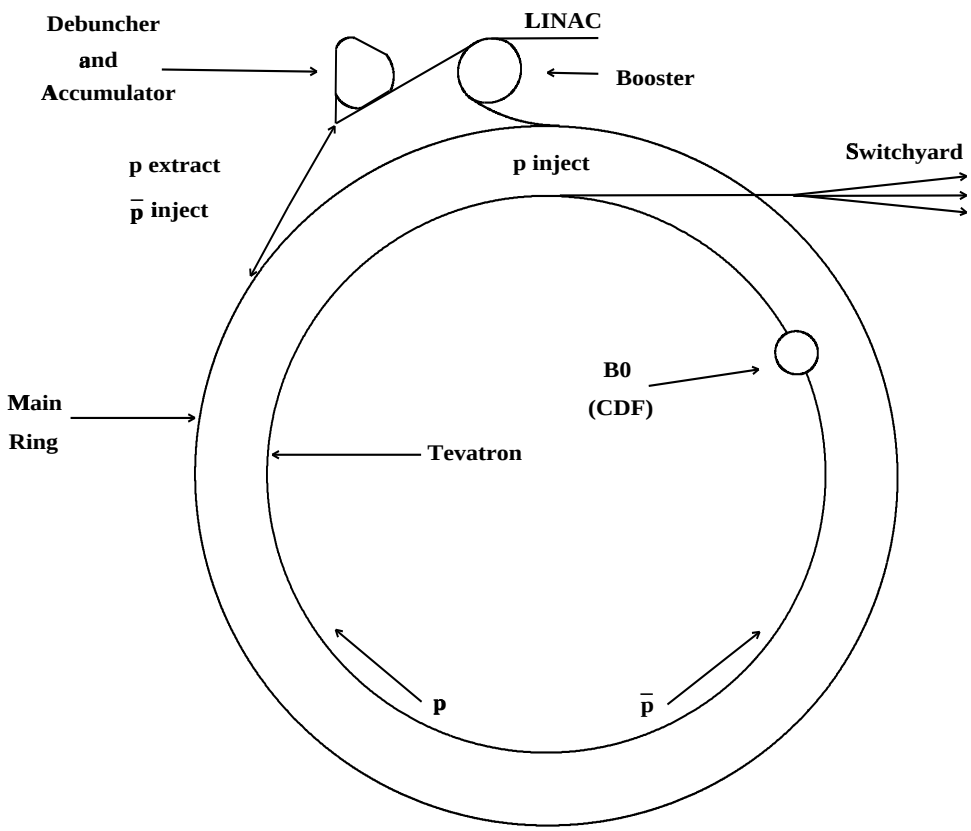

Figure 3.1: Schematic diagram of the Tevatron and its associated accelerators at Fermilab. H^- ions are accelerated in Cockcroft-Walton before they are injected into the LINAC. H^- ions pass through carbon foil, leaving only the protons in the Booster. The protons then travel to the Main Ring and finally to the Tevatron. Some protons are extracted from the Main Ring to make anti-protons. The anti-protons are re-injected into the Main Ring and then into the Tevatron. The total kinematic energy available to the collision is $\sqrt{s} = 1.8$ TeV.

nets for steering the beam and quadrupole magnets for focusing the beam and a single RF cavity for acceleration. The Main Ring accelerates protons to 150 GeV before injecting them into the Tevatron. The Tevatron is a rapid cycling synchrotron with superconducting magnets. The superconducting magnets can produce a high magnetic field (4 Tesla) to accelerate the protons to 900 GeV in the Tevatron.

To produce antiprotons, some protons in the Main Ring are accelerated to 120 GeV, then extracted from the Main Ring and directed onto a thin disc-shaped tungsten target. For every million protons sent onto the tungsten target, about 10 antiprotons are produced. The energy of the antiprotons produced is expected to be 8 GeV with a large spread. The antiprotons are deflected by a dipole magnet into the Debuncher, away from the beam dump. The Debuncher is a rounded triangular-shaped synchrotron with a mean radius of 90 m. A stochastic cooling technique [41] is employed to reduce the energy spread and the transverse motion of the antiprotons [1]. When the momentum spread of the antiprotons has been sufficiently reduced, the antiprotons are transferred to the Accumulator where they are stored before they are finally transferred to the Main Ring for injection. The Accumulator is also a rounded triangular-shaped synchrotron with a mean radius of 75 m, and is located in the same enclosure as the Debuncher. While a store of protons and antiprotons are being circulated, the production of antiprotons continues in order to accumulate enough antiprotons for the next "run" of the Tevatron.

The Tevatron provides the final stage of acceleration, taking both protons and antiprotons to 900 GeV. During collider Run IB, the Tevatron was operated with the colliding beams grouped into six bunches of protons and six bunches of antiprotons which traverse the Tevatron's 6 km circumference at a rate of 50 kHz. The

[1] The idea is to sense the phase of a particle at some point in the ring, and send that information to the RF station before the particle arrives. This information is then used by the RF station to correct the motion of the particle.

superconducting dipole magnets provide a bending field of 4.4 Tesla. Electrostatic separators keep the proton and antiproton beams in different helical orbits to minimize the spreading of the beams from interaction. Special magnets called low beta quadrupoles focus the beam spot to about 60 μm across to increase the probability of a collision.

The number of events produced per second is the product of the cross section and the instantaneous luminosity. The cross section is proportional to the probability of particle interactions and is measured in units of *barns*: 1 b = 10^{-24} cm^2. The instantaneous luminosity is defined as the number of particles passing through the cross section of the interaction region per square centimeter per second (cm^{-2}s^{-1}).

The instantaneous luminosity is given by:

$$\mathcal{L} = \frac{N_p N_{\overline{p}} B f_0}{4\pi\sigma_A^2} \tag{3.1}$$

where $N_p \sim 2 \times 10^{11}$ and $N_{\overline{p}} \sim 6 \times 10^{10}$ are the numbers of protons and antiprotons in each bunch, $B = 6$ is the number of bunches of each type, $f_0 \sim 50$ kHz is the frequency of revolution, $\sigma_A \sim 30$ μm is the mean radius of the beam transverse profile at the interaction point.

During Run IB, instantaneous luminosities were achieved with an average of 1.6×10^{31} cm^{-2}s^{-1} (maximal to 2.80×10^{31} cm^{-2}s^{-1}), producing an average 2.5 interactions per beam crossing. Beams are kept circulating in the Tevatron for about 10 hours. The period of time in which colliding beams are present in the Tevatron is known as a "store". During this period, the luminosity will drop by an order of magnitude due to losses from proton-antiproton collisions and transverse spreading of the beam. The remaining beam is dumped when the luminosity becomes too low, and a new store of protons and antiprotons are injected into the Tevatron.

3.2 The Collider Detector at Fermilab

The Collider Detector at Fermilab (CDF) is a detector for studying the momentum, energy, and the identity of particles produced in $p\bar{p}$ interactions at the Tevatron, for as large a solid angle as possible around the interaction region. It is thus designed to be a forward-backward and azimuthally symmetric device with almost 4π coverage surrounding the interaction region. It measures approximately 27 meters long, 10 meters high, and weighs about 5000 tons.

The CDF detector can be viewed as being made up of three main functional sections: the tracking detectors, the calorimeters, and the muon chambers. Starting from the interaction region and moving radially outward, the CDF tracking detectors consists of the silicon vertex detector (SVX′), the vertex tracking chamber (VTX), and the central tracking chamber (CTC). The CTC is inside a superconducting solenoid, which provides 1.4 T axial magnetic field. The electromagnetic (EM) and hadronic (HAD) calorimeters surround the tracking detectors, and the muon chambers are the outmost layers. Farther forward are the plug and forward calorimeters, the beam-beam counters (BBC), and the forward muon system (FMU). A perspective view of three quarters of the CDF detector is shown in Figure 3.2. A one quarter view of the CDF detector is shown in Figure 3.3.

The CDF standard coordinate system is right-handed with the positive z-axis pointing in the proton beam direction, the x-axis is radially outward from the center of the Tevatron, and the positive y-axis in the upward vertical direction. The origin is in the geometrical center of the detector. The polar angle θ is measured from the positive z-axis.

In proton-antiproton collisions we expect that a large fraction of the longitudinal momenta/energy escapes the detector coverage in the forward region leading to an

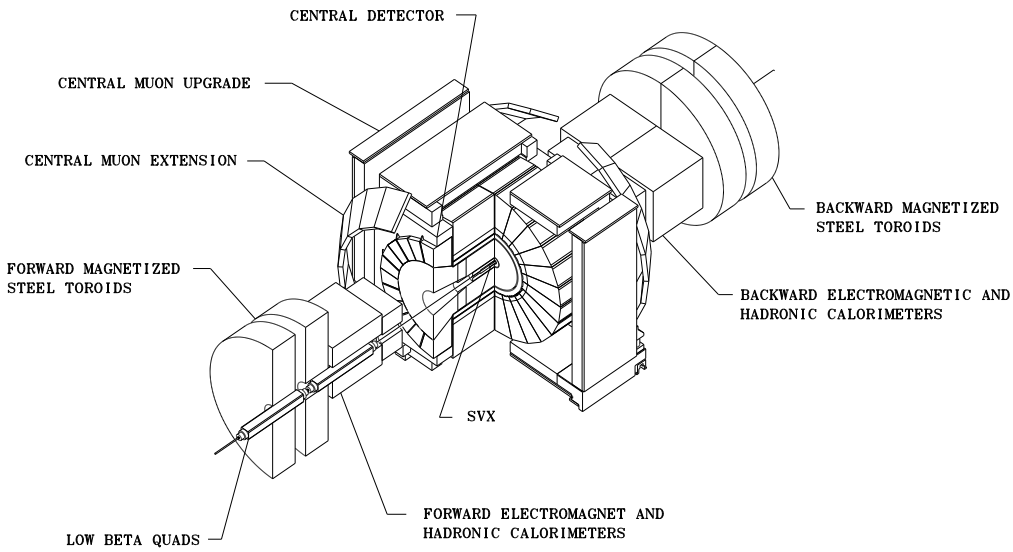

Figure 3.2: A perspective view of three quarters of the CDF detector.

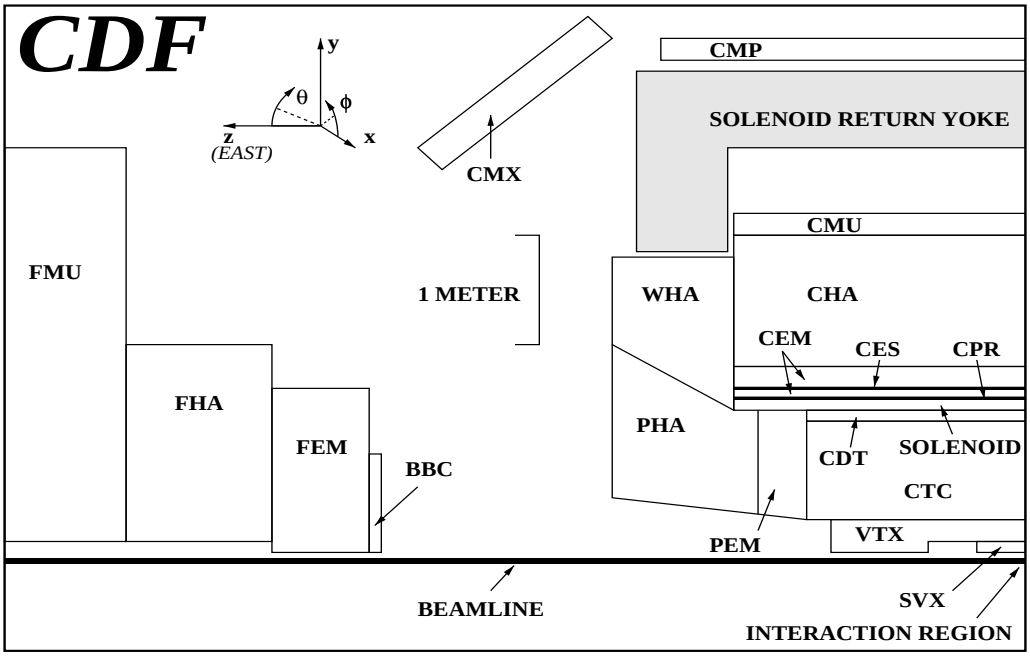

Figure 3.3: A one quarter view of the CDF detector. The interaction region is in the lower right corner. The CDF coordinate system is illustrated in the upper left corner. Leptons are detected and measured in CTC, CEM, PEM, CMU, CMP, and CMX. To determine the missing energy, information from the hadron calorimeters (CHA, WHA, PHA, FHA) and the forward electromagnetic (FEM) calorimeters are also used. The BBCs are used to measure the luminosity.

imbalance when summing up all momenta/energy of the particles observed in the detector. However the momenta and energy of particles transverse to the beam line should balance since the transverse momenta of the two interacting partons are negligibly small. The transverse momentum $\mathrm{p_T}$ and transverse energy E_T [2] are defined as:

$$\begin{aligned} \mathrm{p_T} &= |\mathbf{p}| \times \sin\theta \\ E_T &= E \times \sin\theta \end{aligned} \tag{3.2}$$

The polar angle θ is generally replaced by a variable η defined by

$$\eta \equiv -\ln(\tan\frac{\theta}{2}),$$

which maps $\theta \in (0, \frac{\pi}{2})$ onto $(-\infty, 0)$ and $\theta \in (\frac{\pi}{2}, \pi)$ onto $(0, \infty)$. The variable η is called pseudorapidity because for high energy particles it is a good approximation of the rapidity defined by

$$y \equiv \frac{1}{2}\ln(\frac{E+p_z}{E-p_z}), \tag{3.3}$$

where E is the energy of the particle and p_z is its momentum in the z direction ($p_z = |\mathbf{p}|\cos\theta$). For relativistic particles $p \gg mc$, $E \sim |\mathbf{p}|$; note $\sqrt{\frac{1-\cos\theta}{1+\cos\theta}} = \tan\frac{\theta}{2}$, thus $y \sim \eta$. The shape of the rapidity distribution is invariant under a Lorentz boost along the z-axis, since $y \to y + \tanh^{-1}\beta$ under a boost β in the z direction.

[2] For energetic particles such as electrons and muons produced in the CDF, the $\mathrm{p_T}$ and E_T are almost identical in value. However $\mathrm{p_T}$ refers to momentum measured in the central tracking chamber while E_T refers to energy measured in the calorimeter.

3.2.1 The Tracking Detectors

The CDF tracking detectors consist of the silicon vertex detector (SVX′), the vertex tracking chamber(VTX), and the central tracking chamber (CTC).

SVX′ - Silicon Vertex Detector

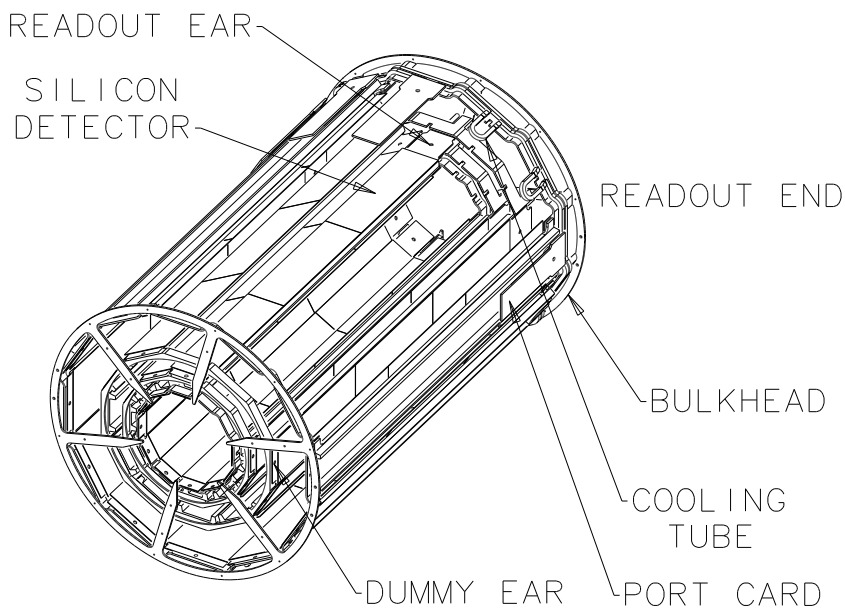

Figure 3.4: One of the SVX′ barrels. The dummy-ear sides of both barrels are located near $z = 0$.

The SVX′ is primarily used to measure the displacement of tracks from the primary vertex. It consists of two independent barrels of equal length aligned end-to-end along the beam line with a 2.15 cm gap at $z = 0$. Figure 3.4 illustrates one of the SVX′ barrels. Each barrel consists of four concentric layers of silicon strip detectors, with radii from 2.9 cm to 7.9 cm measured from the beam line. Each layer has 12 ladders of 25.5 cm in length, and each ladder is divided into three single sided silicon

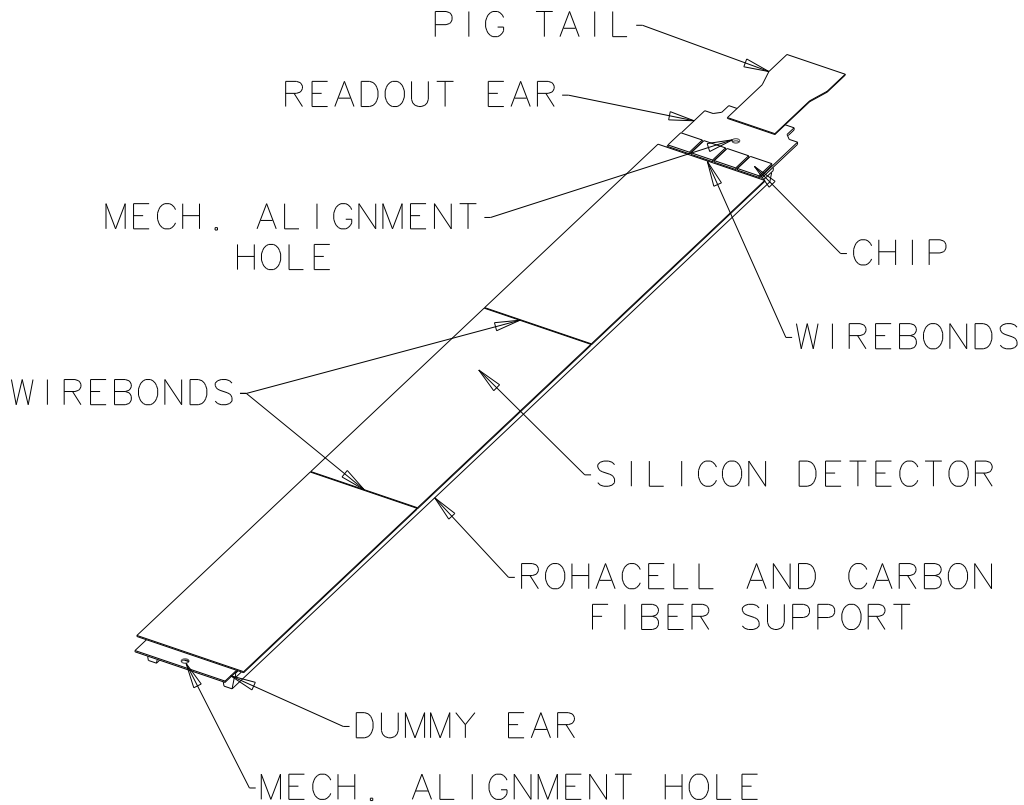

Figure 3.5: SVX′ ladder.

detectors of 8.5 cm long. Figure 3.5 illustrates one SVX′ ladder. The silicon detectors are aligned along the beam line - and thus provide $r - \phi$ tracking. The width of the silicon strips is 60 μm for the three inner layers, 55 μm for the fourth one. Unlike other tracking detectors where electric charge collected on a single wire serves as a measurement of a particle's trajectory, the SVX′ obtains the individual hit position by fitting the charge distribution of neighboring strips ("clusters"). The SVX′ single hit resolution is measured to be 13 μm in $r - \phi$ plane. The resolution of the impact parameter relative to the primary vertex is measured to be 17 μm.

VTX - Vertex Tracking Chamber

The VTX is primarily used to measure the z position of the primary vertex. It surrounds and provides mechanical support for the SVX′ detector. The VTX is 2.8

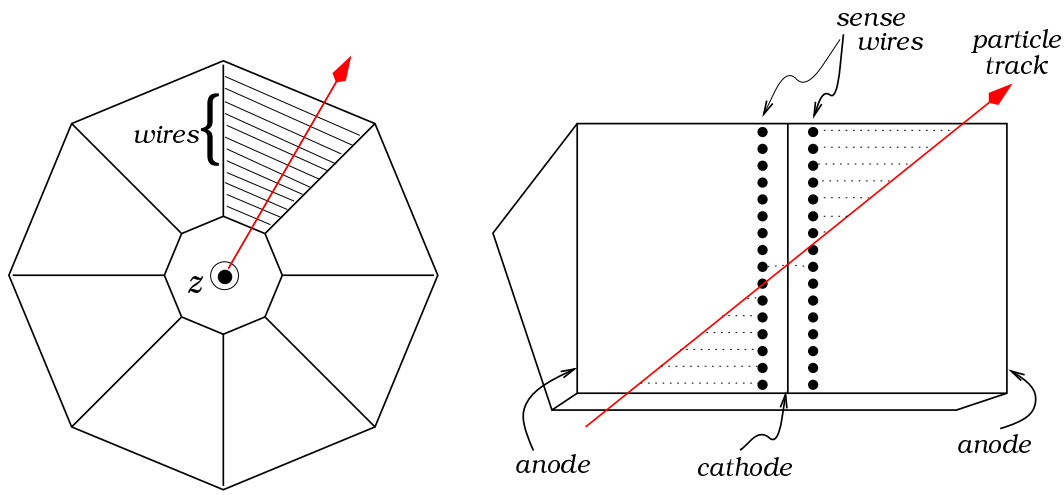

Figure 3.6: Diagram of the VTX. The left shows one drift module in the plane perpendicular to the beam line showing the orientation of the sense wires. The right shows the side view of one octant of a drift module.

m long and has an outer radius of 22 cm, providing a coverage of $\eta < 3.5$. It is a proportional wire chamber segmented into 28 modules along the beam line. The 18 central modules have 16 sense wires. The five modules on each end contain 24 sense wires. All sense wires are perpendicular to the radial direction. Each module is octagonal and composed of 8 wedges, each of which has a coverage of 45°, as illustrated in Figure 3.6. The VTX is filled with a gaseous mixture of 50% argon and 50% ethane bubbled through alcohol at -7 °C. Charged particles passing through the VTX ionize the gas and free electron-ion pairs which drift along the beam line to the sense wires. The wire position gives radial information and the time of arrival to each wire position gives z information. The z resolution of the VTX is measured to be 2 mm.

CTC - Central Tracking Chamber

The CTC is the principal tracking device of the CDF detector which is used to measure the curvature, azimuthal angle and polar angle of charged tracks to determine their momenta. The CTC is a 3.2 m long cylindrical drift chamber with a 554 mm

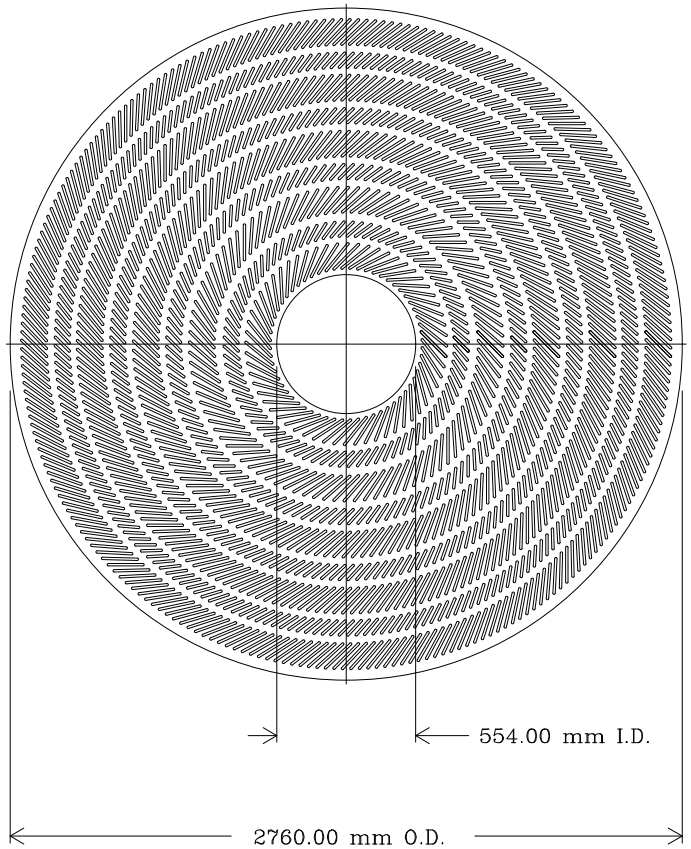

Figure 3.7: Diagram of the CTC endplate illustrates the alternating five axial superlayers and four stereo superlayers, viewed along the z axis.

inner diameter, a 2760 mm outer diameter, and is inside a 1.4 Tesla magnetic field. The CTC is filled with argon-ethane-ethanol gas mixture (49.6/49.6/0.8%). The gas in the CTC is ionized as charged particles pass through it. There are 36,504 wires parallel to the z axis, connecting the two endplates of the CTC. Among them 6,156 wires are 40 μm gold-plated tungsten sense wires used to collect the electrons which are formed from the ionization of the gas; the other wires are field shaping wires, which are used to achieve the desired shape of the electric field in which the electrons drift towards a sense wire.

The CTC has 84 layers of sense wires, which are grouped into 5 axial and 4 stereo

"superlayers", as illustrated in Figure 3.7. Each axial superlayer contains 12 radially separated layers of sense wires parallel to the z axis and provides $r-\phi$ information. Each stereo superlayer contains 6 radially separated layers of sense wires oriented with an approximately $\pm 3^\circ$ angle with respect to the z axis, and provides both $r-\phi$ and z information. The axial and stereo information is combined to form a 3d track and subsequently to determine the momentum of a charged particle.

The maximum drift time for ionized electrons to reach sense wires is around 800 ns, which is shorter than 3.5 μs between two bunch crossings. The individual wire resolution is about 200 μm and the two track resolution is about 5 mm. The momentum resolution of the CTC is $\frac{\delta p_T}{{p_T}^2} \leq 0.002$ (GeV/c)$^{-1}$. It is improved to $\frac{\delta p_T}{{p_T}^2} \leq 0.001$ (GeV/c)$^{-1}$ when the SVX$'$ tracking information is also used in the track fit. The combined information of SVX$'$, VTX and CTC is used to reconstruct final tracks in this analysis.

3.2.2 Calorimeters

The calorimeters are used to measure energy deposited by incident particles. There are two types of calorimeter in CDF: electromagnetic calorimeters measure the energy of electrons and photons, and hadronic calorimeters measure hadronic energies. Both electromagnetic and hadronic calorimeters consist of alternating layers of absorbing material (such as lead or steel) and active material. The incident particles interact with the absorbing material and cause particle cascades (showers). The active material [3] samples the number of charged particles generated in the shower at various depths and derive the incident particle energy.

A high-energy electron entering the electromagnetic calorimeters initiates an

[3]Scintillator sampling is chosen for the central and endwall regions because of its good energy resolution. Gas sampling is used for the plug and forward regions because energy resolution becomes less critical.

electromagnetic cascade in the absorbing material by emitting photons through bremsstrahlung [4]. The emitted photons promptly converts into e^+e^- pairs which can then emit photons through bremsstrahlung. A high-energy photon entering the electromagnetic calorimeters initiates the cascade by converting to an e^+e^- pair first, but otherwise the process is identical to the shower of an electron. The shower process continues until the energy of electrons/positrons is so low ($\sim$ 10 MeV) that they deposit energy through ionization rather than bremsstrahlung. When electrons and positrons generated in the electromagnetic cascades enter the scintillator layers, they produce light, which is collected by photomultiplier tubes. The total amount of light collected is proportional to the energy of the electron or photon that entered the calorimeter.

Hadrons can deposit energy in matter through strong inelastic collisions with nuclei. For example an incident hadron might produce several pions in its first nuclear collision; these pions can then collide with downstream nuclei, producing more particles. The process repeats until eventually the energy of particles is so low that the particles deposit energy through ionization. The hadron calorimeters are basically the same in operation as the electromagnetic calorimeters in front of them.

The CDF calorimeters use a projective tower geometry with towers of constant η which point back to the interaction region, covering 2π in ϕ and -4.2 to 4.2 in η. The most important calorimeters for this analysis are the central (CEM) and plug (PEM) electromagnetic calorimeters, covering the η regions $0 \leq |\eta| \leq 1.1$ and $1.1 \leq |\eta| \leq 2.4$ respectively, and the central (CHA), wall (WHA) and plug (PHA) hadronic calorimeters, covering the η regions $0 \leq |\eta| \leq 0.9$, $0.7 \leq |\eta| \leq 1.3$ and $1.3 \leq |\eta| \leq 2.4$ respectively. Figure 3.8 shows the $\eta - \phi$ segmentation of the

[4]Bremsstrahlung is electromagnetic radiation produced by the acceleration of a charged particle. In particular, the term is used here for radiation caused by decelerations of a charged particle (such as an electron) when passing through the field of atomic nuclei.

calorimeters. Table 3.1 summarizes the properties of the calorimeters. The depths in the electromagnetic calorimeters are described by radiation lengths; a radiation length is the mean distance over which a high-energy electron loses all but $1/e$ of its energy by bremsstrahlung. The depths in the hadronic calorimeters are described by interaction lengths; of N particles passing through one interaction length, all but N/e will interact with nucleus in the material.

Table 3.1: Summary of the properties of the CDF calorimeters. Energy resolutions for the EM calorimeters are for electrons and photons and the hadronic calorimeters are for pions. The symbol $\oplus$ denotes a quadrature sum, $a \oplus b \equiv \sqrt{a^2 + b^2}$. X_0 stands for radiation lengths. λ_0 stands for interaction lengths.

System	η Coverage	Energy Resolution	Thickness
CEM	$\lvert\eta\rvert < 1.1$	$13.5\%/\sqrt{E_T} \oplus 2\%$	18 X_0
PEM	$1.1 < \lvert\eta\rvert < 2.4$	$22\%/\sqrt{E_T} \oplus 2\%$	18-21 X_0
FEM	$2.2 < \lvert\eta\rvert < 4.2$	$26\%/\sqrt{E_T} \oplus 2\%$	25 X_0
CHA	$\lvert\eta\rvert < 0.9$	$50\%/\sqrt{E_T} \oplus 3\%$	4.5 λ_0
WHA	$0.7 < \lvert\eta\rvert < 1.3$	$75\%/\sqrt{E_T} \oplus 4\%$	4.5 λ_0
PHA	$1.3 < \lvert\eta\rvert < 2.4$	$106\%/\sqrt{E_T} \oplus 4\%$	5.7 λ_0
FHA	$2.4 < \lvert\eta\rvert < 4.2$	$137\%/\sqrt{E_T} \oplus 4\%$	7.7 λ_0

Electromagnetic Calorimeters

The Central ElectroMagnetic calorimeter (CEM) is composed of alternating layers of 3.2 mm thick lead absorber and 5 mm thick polystyrene scintillator. The CEM is optimized to detect electromagnetic showers generated by electrons and photons. The depth of the CEM is chosen so that most electron and photon showers will be completely contained in its volume.

The CEM is about 18 radiation lengths thick and is divided into 24 wedges with each wedge covering 15° in ϕ and 1 in η. Each wedge is divided into 10 towers along the beam line except one wedge which is notched to allow access to the coil and consequently has only 8 towers. Figure 3.9 illustrates one CEM wedge. Two

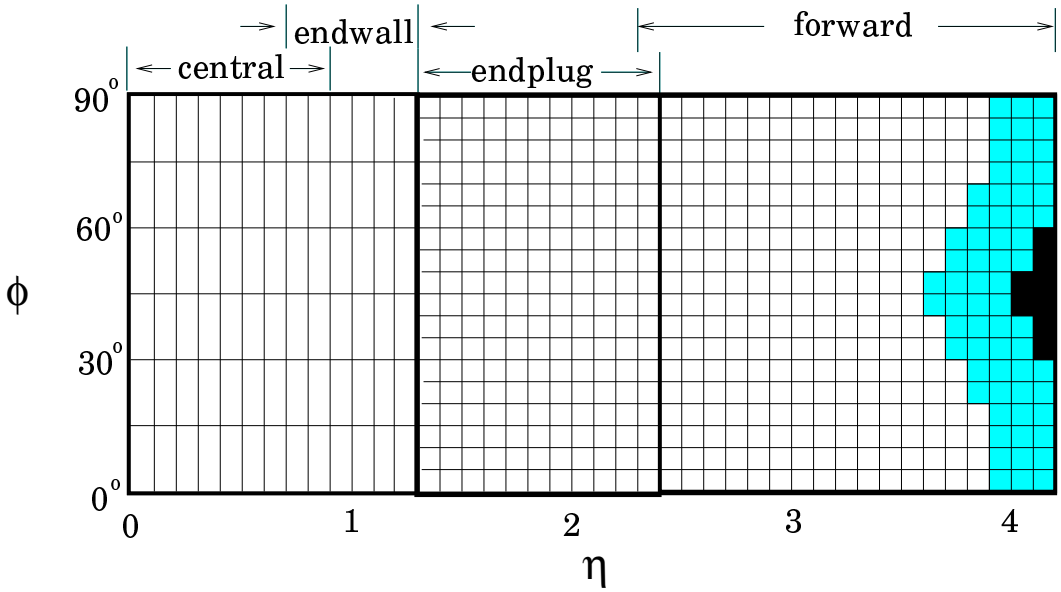

Figure 3.8: The $\eta - \phi$ segmentation of the calorimeters in the CDF detector. The central electromagnetic calorimeter (CEM) covers the η regions $0 \leq |\eta| \leq 1.1$. The plug electromagnetic calorimeter (PEM) covers the η regions $1.1 \leq |\eta| \leq 2.4$. The central (CHA), wall (WHA) and plug (PHA) hadronic calorimeters cover the η regions $0 \leq |\eta| \leq 0.9$, $0.7 \leq |\eta| \leq 1.3$ and $1.3 \leq |\eta| \leq 2.4$ respectively. In the Forward region the shaded region indicates electromagnetic coverage only, and the black region indicates no coverage at all (due to the presence of Tevatron magnets).

wavelength shifters direct the light from the scintillator to photomultiplier tubes for each tower.

The Central Preradiator detector (CPR) is a set of proportional chambers positioned between the CEM and the superconducting solenoid. The CPR samples early development of the electromagnetic showers caused by the material of the solenoid coil, and is used to distinguish between electrons and hadrons.

The Central Electromagnetic Strip Chamber (CES) is a set of proportional strip and wire chambers located six radiation lengths (r = 184.15 cm) deep into the CEM (a location which is approximately the shower maximum for electromagnetic showers). The CES provides both $r - \phi$ and z information about the shower and has resolution of ± 2 mm.

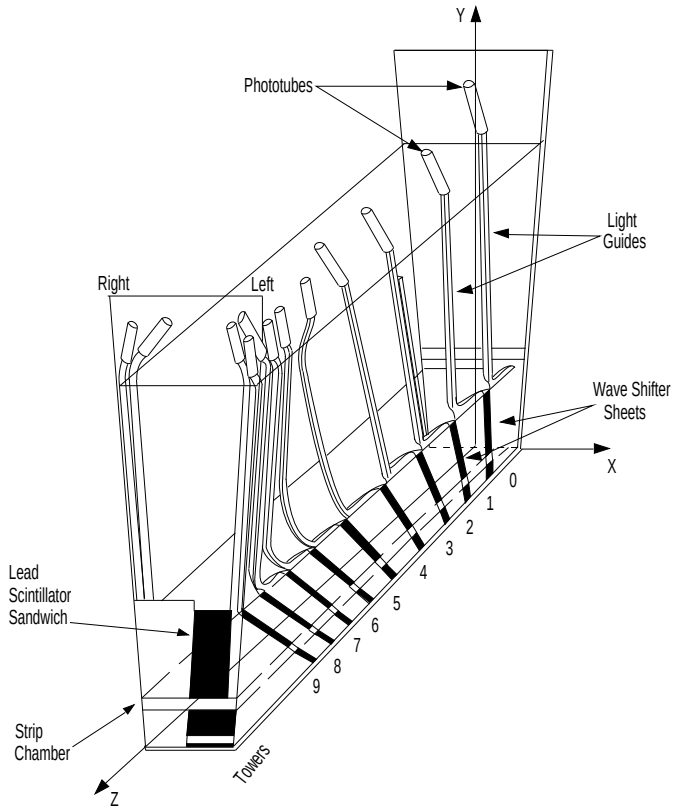

Figure 3.9: Diagram of the CEM light collection system in a single wedge of the CEM and CHA calorimeters. Each CEM wedge has 31 layers of 3.2 mm thick lead absorber alternating with 5 mm thick layers of plastic scintillator. Each CHA wedge has 32 layers of 2.5 cm thick steel absorber alternating with layers of 1 cm thick plastic scintillator.

The Plug ElectroMagnetic calorimeter (PEM) is a multi-wire gas proportional system with a 50%/50% mixture of argon/ethane gas as active material. The PEM is segmented into 72 5° ϕ wedges. There are 34 layers of proportional drift tube arrays interleaved with 2.7 mm thick layers of lead. The PEM is about 18 radiation lengths thick.

Hadronic Calorimeters

The hadron calorimeters consist of steel absorbers alternating with acrylic scintillators in the central and endwall regions and gas proportional chambers in the plug

region. The CHA has 32 layers of 2.5 cm thick steel absorbers and is about 4.5 interaction lengths thick. The WHA has 15 layers of 5.1 cm thick steel absorbers and is about 4.5 interaction lengths thick. The PHA has 20 layers of 5.1 cm thick steel absorbers and is about 5.7 interaction lengths thick.

3.2.3 The Muon Chambers

The muon chambers are the outermost layers of the CDF detector. The three central muon detectors are important for this analysis: the central muon detector (CMU), the central muon upgrade detector (CMP), and the central muon extension detector (CMX). Figure 3.10 shows the central muon detector $\eta - \phi$ coverage.

The CMU is located just outside the CHA at a distance of 3.47 m from the beam line. The CHA serves as a hadron absorber with approximately 5 interaction lengths. Muons are minimum-ionizing particles and are capable of penetrating large amount of dense matter. A muon of $p_T > 1.4$ GeV/c has sufficient momentum to pass through the calorimeters and enter the CMU.

The CMU covers 84% of the solid angle for the region $|\eta| < 0.6$ and is segmented into 12.6° wedges in ϕ. Each wedge is further divided into three modules of 4.2° each. Each module consists of four layers of four rectangular drift chambers. The drift cell wires run parallel to the z axis and alternate layers in the $r - \phi$ plane have their centers aligned with the geometrical center of the detector. This allows a rough momentum measurement of muons by the CMU. Muon tracks through the CMU are reconstructed [5] by using charge division in the longitudinal (z) direction and time-to-distance relationships in the drift (ϕ) direction. The position resolution of a muon track along the sense wire (z) direction is 1.2 mm. The position resolution

[5] A reconstructed muon track in the muon chambers is often referred to as a muon stub. Muons are identified by a track in the CTC which is matched to a muon stub in one of the CDF muon detectors.

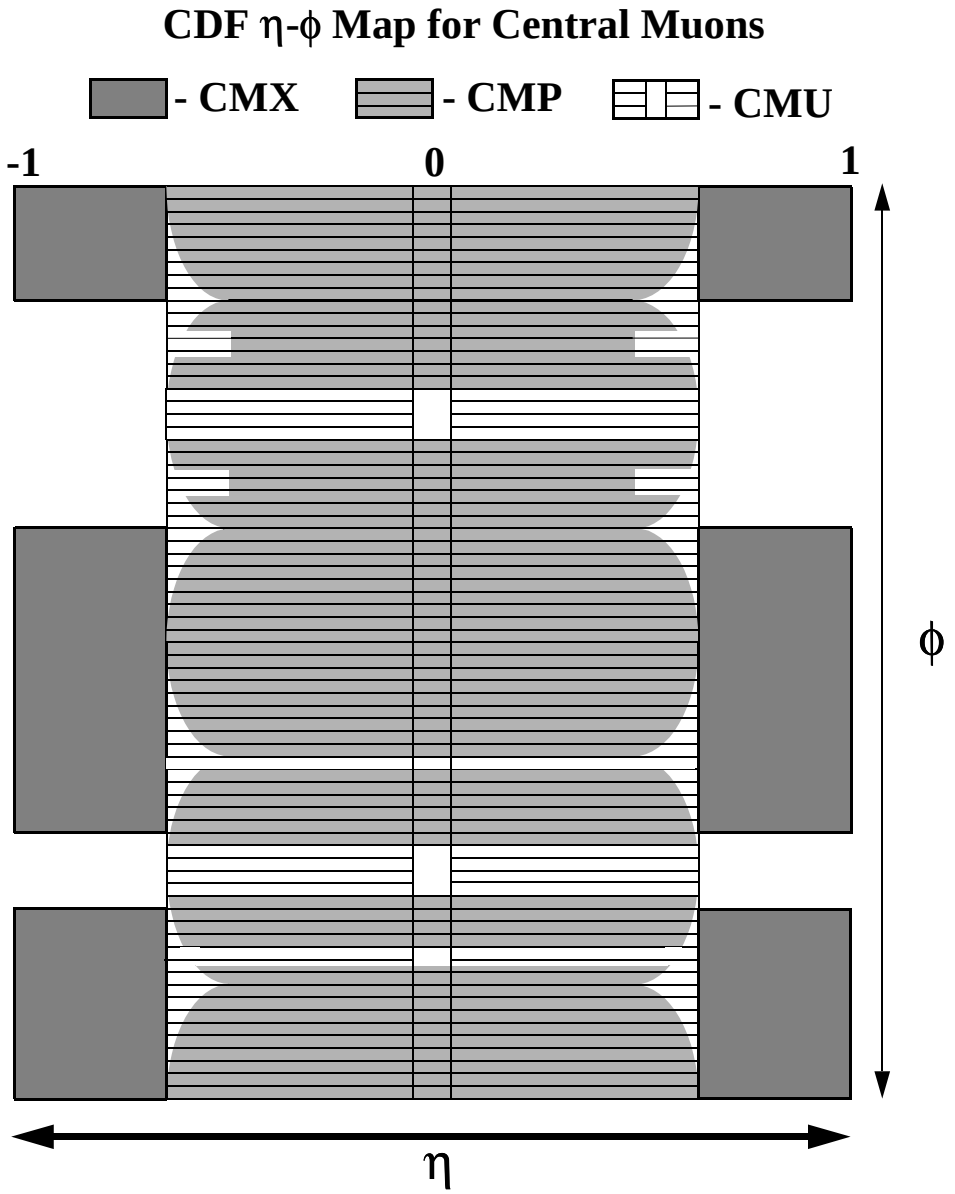

Figure 3.10: $\eta - \phi$ coverage of the muon system for the central region of the CDF detector. The ϕ gaps at $\phi \sim 90°$ and $\phi \sim 270°$ in the CMX coverage are where the CMX intersects Tevatron components (small gap) and the collision hall floor (large gap), respectively.

of a muon track along the drift (ϕ) direction is 250 μm.

Outside the CMU are located 0.6 m thick steel absorbers which provide an additional hadron absorbtion of approximately 3 interaction lengths. Outside the steel absorbers are four more layers of drift chambers (of similar construction to those in the CMU) known as the CMP, covering approximately 63% of the solid angle for the region $|\eta| < 0.6$. The CMU and the CMP overlap for 53% of the solid angle. Because the central calorimeters provide only 5 hadronic interaction lengths shielding, some energetic jets can punch through the calorimeters and reach the CMU, faking the signature of a muon. The CMP is very useful in reducing fake muons because of the extra steel absorbers.

The third muon detector is the CMX which is similar to the CMP but on alternate layers the wire centers are collinear with the geometrical center of the detector. It is behind approximately 5 hadronic interaction lengths shielding provided by the plug calorimeters. The CMX covers approximately 71% of the solid angle for the region $0.6 < |\eta| < 1.0$. The CMX has a 30° gap at the top of the detector due to the Main Ring and the solenoid cooling system, and a 90° gap at the bottom where it intersects the collision hall floor. The CMX is grouped into four stacks, and each stack consists of eight modules. Each module contains proportional drift chambers for muon detection, sandwiched between scintillators for triggering.

3.2.4 Beam-Beam Counters

The Beam-Beam counters (BBCs) are small scintillation detectors. There are two planes of BBCs located in front of the forward calorimeter, perpendicular to the beam line and at 5.8 m from the interaction point, covering $3.24 < |\eta| < 5.90$ ($0.32° < \theta < 4.47°$). Each plane consists 16 scintillation detectors. When at least one of the BBC scintillators on both planes is hit coinciding with the $p\bar{p}$ bunch crossing, the

minimum-bias trigger is activated meaning there is at least one interaction during the bunch crossing. Thus the BBC serves as a luminosity monitor, and the instantaneous luminosity is the rate of coincidences divided by the effective cross sectional area of the $p\bar{p}$ beam overlap.

3.2.5 The Trigger Systems

During a run at CDF, the proton and antiproton bunches cross every 3.5μs, which is equivalent to an interaction rate of 286 kHz assuming there is one interaction per crossing. A CDF event has an average data size of ~0.2 MB, thus events can only be written out to 8 mm magnetic tapes at a rate of approximately 10 Hz, which constitutes the primary limitation of the CDF data acquisition (DAQ) system. However, most of the interactions produce noise or uninteresting events that are not worth saving for offline processing. By selecting only interesting physics events, the CDF trigger system reduces the rate at which data are written to tape.

The CDF trigger is organized into a three level system to accommodate the $p\bar{p}$ collision rate and select interesting physics events with a $\sim$ 30,000:1 rejection factor. The trigger levels, as well as the data acquisition system, are controlled by the Trigger Supervisor (TS), the Buffer Manager (BM), and Timing Control (TC) (see Figure 3.11).

Level 1 Trigger

The Level 1 trigger system makes a decision on whether to accept or reject an event in less than the 3.5μs bunch crossing period to avoid causing dead time [6]. The fast decision is achieved by the analog read-out and processing of data from

[6] 'Dead time' here refers to the amount of time that the CDF DAQ system is unable to consider subsequent collision events.

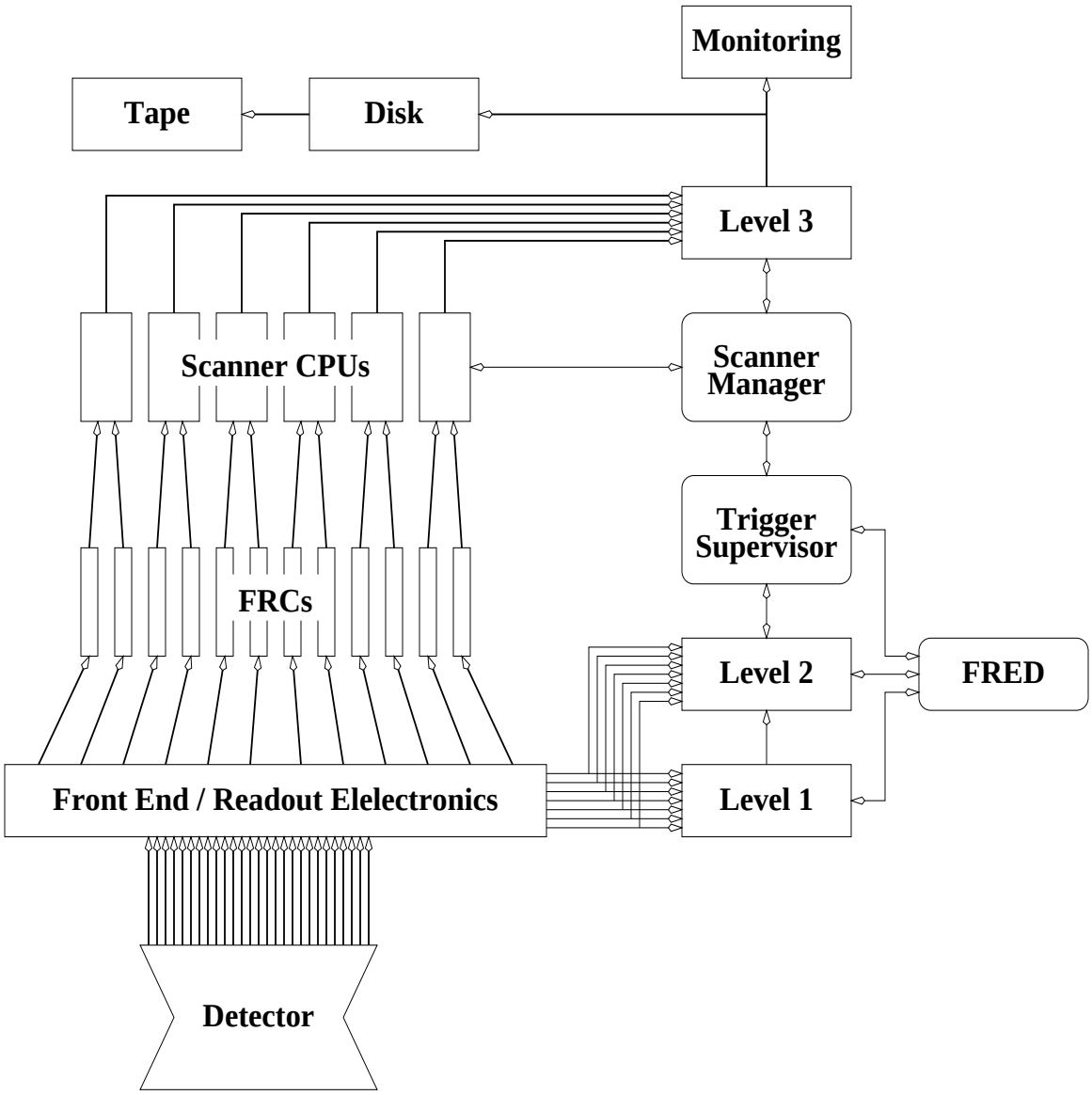

Figure 3.11: Schematic drawing of the principal elements of the CDF data acquisition pipeline. The L1 trigger and the L2 trigger have separate data paths coming from the readout electronics. The Trigger Supervisor controls the trigger logic through the L2 trigger. "FRED" is the logic combining L1 and L2 decisions. The Front Readout Controls (FRCs) read data from the electronics and pass onto the Scanner CPUs. The Scanner Manager and Scanner CPUs are part of the hub feeding Level 3. The L3 trigger uses a farm of commercial computers to reconstruct the events.

selected components with dedicated FASTBUS-based electronics. The Level 1 trigger acceptance rate is approximately 1 kHz (rejection rate is about 100 : 1). The Level 1 trigger primarily uses signals from the calorimeters and the muon systems, such as imbalance in the energy flow observed in the calorimeter or the existence of a high energy lepton.

There are two categories of lepton triggers in Level 1: single-lepton triggers with higher p_T thresholds and dilepton triggers with lower p_T thresholds. Muons are triggered upon the required muon chamber signals. Electrons are triggered upon the observation of energy in the EM calorimeters and not in the hadronic calorimeters.

The calorimeter triggers in Level 1 are determined based on the fast analog outputs from the calorimeter towers. Fast algorithms are implemented in a series of hardware modules to process these signals. The majority of the events are required to exceed a 10 GeV total energy threshold to trigger.

Level 2 Trigger

The Level 2 trigger examines the analog signals from the DAQ front end cards in more detail than the Level 1, and a decision is made every 20 μs. The typical Level 2 trigger rate is of the order of tens of Hz.

The central fast tracker (CFT) is a high speed hardware track processor that reconstructs high p_T charged tracks in the CTC. The CFT only examines hits in the five axial superlayers of the CTC to determine the transverse momentum and azimuth of a charged particle. The CFT constructs tracks by first examining hits in the outermost superlayers, and searches for hits on layers further-in along helical wedges calculated in advance. More than 95% of all tracks that would coincide with the prompt hit found in the outmost layer are thereby included. These tracks are sorted into 16 bins in transverse momentum and 144 bins in azimuthal angle.

The Level 2 trigger constructs "physics objects" including jets, photons, electrons, muons, neutrinos (missing transverse energy), and total transverse energy using information from calorimeters, CFT tracks, and muon stubs.

Level 3 Trigger

The Level 3 trigger system, also known as the Level 3 farm, uses 64 commercial processors manufactured by Silicon Graphics, Inc. running IRIX operating system. The processors reconstruct events with fast software algorithms and screened with a set of filters. The typical L3 trigger rate is approximately 10 Hz (rejection rate is about 3 : 1). If an event is accepted by the Level 3 trigger, it is written to 8-mm tapes for offline processing. Rarer processes and interesting events are written to disk in a separate data stream in addition to being recorded to magnetic tapes.

The offline processing can utilize better calibration and alignment parameters, more comprehensive run condition information, and reconstruct more detailed physics objects for analysis of the elementary particle physics.

Chapter 4

Search Strategy

In this chapter we describe the collider phenomenology of the MUED scenario and the "blind analysis" procedure.

4.1 Collider Phenomenology of the MUED Scenario

The heavier $n = 1$ KK states cascade decay into the LKP by emitting soft SM particles. The cascade decay of the $n = 1$ KK modes ends in the γ_1 LKP (Fig. 4.1, Ref. [34]). The lowest level KK partners carry a conserved quantum number, KK parity, which guarantees that the LKP γ_1 is stable. The LKP γ_1 escapes detection, resulting in a missing energy signature.

KK quarks and gluons have the largest production cross section among all stable KK states in TeV energy hadron colliders such as the Tevatron or the LHC (see Fig. 4.2). The $n = 1$ KK states are pair produced because of KK parity conservation. The KK production cross sections at the Tevatron and the LHC are calculated in

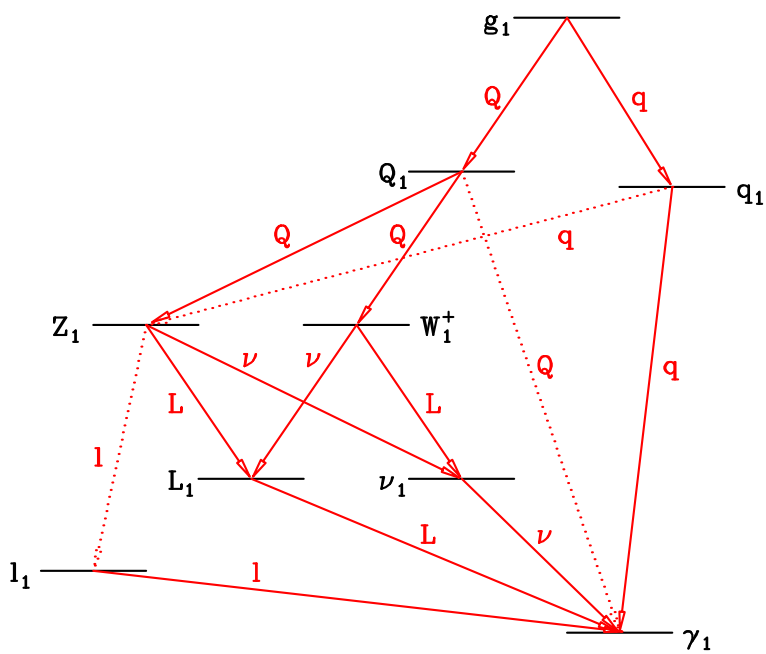

Figure 4.1: The $n = 1$ KK spectroscopy showing the dominant (solid) and rare (dotted) transitions and the resulting decay products. Ref [34]

[32, 42] [1].

The heaviest KK particle of the $n = 1$ modes is the KK gluon g_1. It decays to a KK quark and an ordinary quark. The branching ratios are $B(g_1 \rightarrow Q_1 Q_0) \simeq B(g_1 \rightarrow q_1 q_0) \simeq 0.5$ [34].

The SU(2)-singlet KK quarks (q_1) will decay to the $n = 0$ mode (ordinary) quarks and a γ_1. The signature is thus jets plus missing energy ($\not{E}_T$).

The SU(2)-doublet KK quarks (Q_1) will mostly decay to the $n = 0$ mode (ordinary) quark and a KK W_1 or KK Z_1 boson. KK W_1 or KK Z_1 bosons will then subsequently decay to KK leptons plus ordinary leptons. KK leptons will decay to an ordinary lepton and a γ_1. The final signature would be 3 leptons + 2 jets (from

[1]There are some errors in the formulas for amplitudes squared presented in [32]. However the figures (such as Fig. 4.2) are accurate since the errors in the formulas are consequence of some manipulations the authors performed in order to make them shorter for publication. Private communication with Cosmin Macesanu.

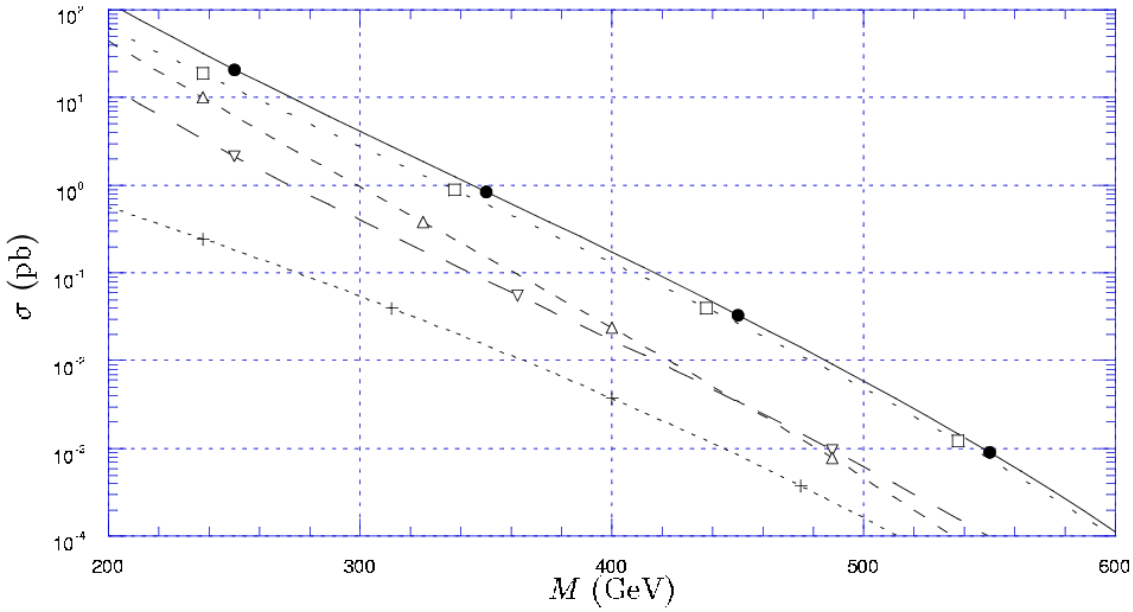

Figure 4.2: The cross section for the production of two stable KK final states is shown as a function of the KK mass for Tevatron Run I. The solid curve corresponds to the total contribution, while the dashed lines represent the partial contributions of KK quark pair (□), KK quark-gluon (△), and KK gluon pair (▽) production. For the case of double KK quark production, the final state consists of light quark KK excitations, excluding the top quark. Top production (+) has a different collider signature (namely, the top will subsequently decay into additional states). The production of KK quark pairs is dominant. From Ref. [32].

the $W_1^{\pm}Z_1$ channel), or 4 leptons + 2 jets (from the Z_1Z_1 channel) (see Fig. 4.3) [2]. In the limit $\sin\theta_1 \ll 1$ (see Figure 2.5), where θ_1 is the "Weinberg angle" for the $n = 1$ KK mode, $B(Q_1 \to W_1^{\pm}Q_0) \simeq 2B(Q_1 \to Z_1Q_0)$. Also

$$\frac{B(Q_1 \to Z_1Q_0)}{B(Q_1 \to \gamma_1Q_0)} \simeq \frac{g_2^2\, T_{3Q}^2\, (m_{Q_1}^2 - m_{Z_1}^2)}{g_1^2\, Y_Q^2\, (m_{Q_1}^2 - m_{\gamma_1}^2)}\ , \tag{4.1}$$

where g_2 (g_1) is the $SU(2)_L$ ($U(1)_Y$) gauge coupling, T_3 is the weak isospin, and Y is the hypercharge. The branching ratios are: $B(Q_1 \to W_1^{\pm}Q_0) \sim 65\%$, $B(Q_1 \to Z_1Q_0) \sim 33\%$ and $B(Q_1 \to \gamma_1Q_0) \sim 2\%$ [34]. $W_1^{\pm}$ and Z_1 decay to all lepton flavors

[2] In this analysis the "multi-lepton" signature means final decay products of three or more electrons/muons, and "lepton selection" stands for the selection of electrons/muons.

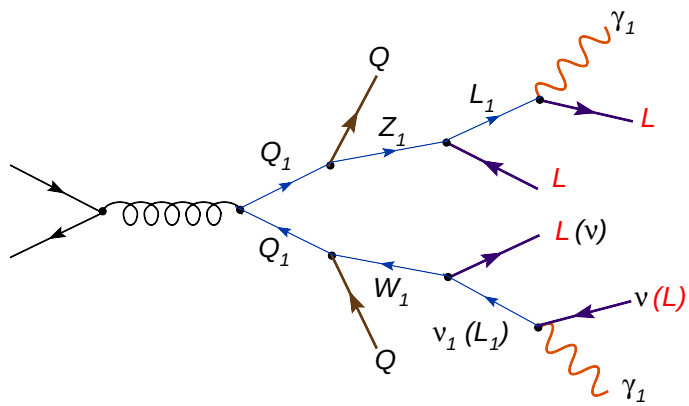

Figure 4.3: The Feynman diagram for n=1 KK quark pair production and subsequent decays to 3 or 4 lepton final state. The signature would be 3 leptons + $\not{E}_T$+ 2 jets ($W_1^{\pm}Z_1$), or 4 leptons + $\not{E}_T$+ 2 jets (Z_1Z_1).

with $B(W_1^{\pm} \to \nu_1 L_0^{\pm}) = B(W_1^{\pm} \to L_1^{\pm}\nu_0) = \frac{1}{6}$ and $B(Z_1 \to L_1^{\pm}L_0^{\mp}) = B(Z_1 \to \nu_1\overline{\nu}_0) \simeq \frac{1}{6}$ for each generation. $Z_1 \to l_1^{\pm}l_0^{\mp}$ decays are suppressed by $\sin^2\theta_1$ so they can be neglected.

Table 4.1: SU(2)-doublet KK quark decay branching ratio in each individual channel. Channels with a check mark are contributing to the signal search in our experiment.

channel	branching ratio	visible
$Q_1 \to W_1 \to \nu_{1e}e_0$	$\frac{2}{3} \times \frac{1}{6}$	✓
$Q_1 \to W_1 \to \nu_{1\mu}\mu_0$	$\frac{2}{3} \times \frac{1}{6}$	✓
$Q_1 \to W_1 \to \nu_{1\tau}\tau_0$	$\frac{2}{3} \times \frac{1}{6}$	
$Q_1 \to W_1 \to \nu_{0e}e_1$	$\frac{2}{3} \times \frac{1}{6}$	✓
$Q_1 \to W_1 \to \nu_{0\mu}\mu_1$	$\frac{2}{3} \times \frac{1}{6}$	✓
$Q_1 \to W_1 \to \nu_{0\tau}\tau_1$	$\frac{2}{3} \times \frac{1}{6}$	
$Q_1 \to Z_1 \to e_1e_0$	$\frac{1}{3} \times \frac{1}{6}$	✓
$Q_1 \to Z_1 \to \mu_1\mu_0$	$\frac{1}{3} \times \frac{1}{6}$	✓
$Q_1 \to Z_1 \to \tau_1\tau_0$	$\frac{1}{3} \times \frac{1}{6}$	
$Q_1 \to Z_1 \to \nu_{1e}\nu_{0e}$	$\frac{1}{3} \times \frac{1}{6}$	
$Q_1 \to Z_1 \to \nu_{1\mu}\nu_{0\mu}$	$\frac{1}{3} \times \frac{1}{6}$	
$Q_1 \to Z_1 \to \nu_{1\tau}\nu_{0\tau}$	$\frac{1}{3} \times \frac{1}{6}$	

Neglecting $Q_1 \to \gamma_1 Q_0$, the branching ratios for $Q_1 \to W_1$ and $Q_1 \to Z_1$ are about

$\frac{2}{3}$ and $\frac{1}{3}$ respectively. Table 4.1 lists the branching ratio in each individual channel. Only channels with a check mark contribute to the signal search in our experiment [3], and the effective ratio of $Q_1 \rightarrow \mathrm{W}_1$ to $Q_1 \rightarrow \mathrm{Z}_1$ is 4:1, thus in our signal Monte Carlo simulations we use an effective branching fraction of $B(Q_1 \rightarrow \mathrm{W}_1^{\pm} Q_0') \sim 80\%$ and $B(Q_1 \rightarrow \mathrm{Z}_1 Q_0) \sim 20\%$, and we force W_1 and Z_1 decay to the channels with a check mark only.

The final state signature for the MUED scenario at the Tevatron would be multiple leptons, jets, plus missing energy, which is similar to the squark and gluino searches in the R-parity conserving supersymmetry models. The largest overall signature from pair produced KK quarks would be at least two jets (ordinary quarks decayed from KK quarks) plus missing energy (carried away by γ_1). However the background is very large for this signal in hadron colliders. In our analysis we prefer the multilepton (ordinary electrons or muons from the $\mathrm{Z}_1\mathrm{Z}_1$ or $\mathrm{Z}_1\mathrm{W}_1$ channel) plus missing energy signature since it's much cleaner.

Pair produced $Q_1 Q_1$ will decay to $\mathrm{Z}_1\mathrm{Z}_1$, $\mathrm{W}_1^{\pm}\mathrm{Z}_1$ and $\mathrm{W}_1^{\pm}\mathrm{W}_1^{\pm}$. The detector signature for the $\mathrm{Z}_1\mathrm{Z}_1$ and $\mathrm{W}_1^{\pm}\mathrm{Z}_1$ events would be 4 or 3 energetic leptons respectively and substantial missing transverse energy. The main background with similar signature comes from $b\bar{b}/c\bar{c}$, $t\bar{t}$, WZ, ZZ production, and Drell-Yan and WW production with misidentified leptons. In order to study techniques for rejecting background, we use Monte Carlo techniques to study a large number of events of both signal and background processes.

The MUED collider signatures look very much like the SUSY collider signatures. The crucial difference is the spins of the heavy partner particles [43]. If signals suggesting the UED are discovered then it will be crucial to measure the spins of

[3] Some τ's decay via the channels $\tau \rightarrow \mu\overline{\nu}_\mu\nu_\tau$ and $\tau \rightarrow e\overline{\nu}_e\nu_\tau$. However the momentum of electrons/muons from these events will not be large enough to pass our lepton selection criteria.

the new particles to demonstrate if they are indeed the predicted KK particles. Measuring spins at hadron colliders is a significant experimental challenge [44].

The $n = 2$ KK particles can be either pair-produced or singly-produced. Pair production is the dominant mechanism as radiative corrections are small compared with tree-level couplings. The $n = 2$ KK particles can then decay either to two $n = 1$ KK particles or one zero mode particle plus one $n = 2$ KK particle. The $n = 2$ KK modes detection provides a way to differentiate UED from SUSY, however it is not as promising as the multi-lepton decay mode in the $n = 1$ KK pair-production due to the small cross sections.

4.2 "Blind Analysis" Procedure

The method used in this analysis is the "blind analysis" method. Its main objective is to avoid biased decisions involving the data selection. This goal is achieved by avoiding looking at the data sample until the signal signature and the total Standard Model backgrounds are evaluated. The complete procedure is described as follows:

1. Identify physics objects in the CDF detector, and select data sample containing three leptons passing certain criteria (Chapter 5).

2. Identify the Standard Model backgrounds that can yield a similar signature to the MUED signal (Chapter 6).

3. Use Monte Carlo to generate both the Standard Model backgrounds and the MUED signal events, then pass through the CDF detector simulation (Chapter 7).

4. Study the Monte Carlo events and develop selection criteria to enhance the MUED signal through suppressing the Standard Model backgrounds. The

event selection criteria are chosen according to the kinematic distribution of decay products to reject background with a minimal loss of signal acceptance, and optimization process is carried out for the final cuts to improve the results. We then apply the selection criteria to the data sample (Chapter 8).

5. Estimate the systematic, statistical and theoretical uncertainties on the number of expected signal and background events (Chapter 9).

6. Obtain a 95% confidence level upper limit on the number of MUED signal events from the number of observed data events, then translate it into an upper limit of MUED production cross section with additional information of branching ratio, total detection efficiency, and integrated luminosity (Chapter 10).

Chapter 5

Data Sample

The data used for this analysis were taken with the Collider Detector at Fermilab (CDF) in the years 1994-1996 (Run IB). We start with the same data set as the CDF trilepton analysis [45, 46], and impose the same trilepton skimming cuts to the data sample. We obtained the same sample size during the process: the Run IB SUSY dilepton data set [47] has 457,478 events, and 15,149 events pass the trilepton skimming cuts. Next we imposed similar analysis cuts except that we did not require leptons to be isolated [1] since leptons from a SU(2)-doublet KK quark decays are not well isolated due to the two quark jets (as determined from our Monte Carlo study, see Fig. 7.3). We obtained 1120 events after our trilepton analysis cuts, which is a larger sample compared with 247 events of the CDF trilepton analysis [45, 46]. Details of this procedure follow below.

[1] Isolation in this analysis is defined as the total energy in a cone (with cone size $\Delta R \equiv \sqrt{\Delta\phi^2 + \Delta\eta^2} = 0.4$) minus the energy of electron or muon.

5.1 Run IB Dilepton Sample

We begin with the 87.5 pb^{-1} Run IB exotic dilepton XDLB_5P data set containing 3,270,488 events. This data set is created using the TDLFLT module[2], which requires events to have a central electron ($|\eta^e| < 1.1$) with $E_T > 8$ GeV or central muon ($|\eta^\mu| < 0.6$) with $p_T > 8$ GeV/c and a second electron ($|\eta^e| < 2.4$) with $E_T > 3$ GeV or muon ($|\eta^\mu| < 1.0$) with $p_T > 3$ GeV/c. This data set contains 3,270,488 events and is written on 63 tapes.

Next, the Run IB SUSY dilepton data set is selected from the exotic dilepton sample by requiring:

- At least one central lepton (CEM, CMU, CMP)[3] passing tight requirements listed in Table 5.1 (electron) or Table 5.2 (muon).
- At least one additional lepton (CEM, PEM, CMU, CMP, CMX, CMIO)[4] passing loose requirements listed in Table 5.1 (electron) or Table 5.2 (muon).

Note that no isolation cut is applied.

A total of 457,478 events [5] are selected for the Run IB SUSY dilepton data set. This is the starting sample for our analysis.

The lepton requirements are explained below:

Electron Identification Cuts The electrons are identified by using calorimeters and the associated track measured in the CTC.

[2]TDLFLT module utilizes the level 3 exotic dilepton trigger (COMBINED_EXOB_DIL [48]).

[3]CEM stands for Central ElectroMagnetic calorimeter. CMU stands for Central MUon detector. CMP stands for Central Muon uPgrade detector.

[4]PEM stands for Plug ElectroMagnetic calorimeter. CMX stands for Central Muon eXtension detector. CMIO stands for Central Minimum Ionizing Object.

[5]These events are written on 8 tapes: RK8876, RK8880, RK8885, RK8895, RK8897, RK8899, RK8921, RK9198.

Table 5.1: Selection criteria for CEM and PEM electrons. Electron candidates are categorized as Tight Central Electron (TCE), Loose Central Electron (LCE) and Loose Plug Electron (LPE).

Lepton	Tight	Loose	
Cut variables	TCE	LCE	LPE
p_T (GeV/c)	≥ 6.0	≥ 2.8	—
E_T (GeV)	≥ 8.0	≥ 4.0	≥ 4.0
E/p	≤ 2.0	≤ 2.0	—
E_{HAD}/E_{EM}	≤ 0.05	$\leq 0.055 + 0.045 \times \frac{E}{100}$	≤ 0.1
L_{SHR}	≤ 0.2	≤ 0.2	—
$\|\Delta x\|$ (cm)	≤ 3.0	≤ 3.0	—
$\|\Delta z\|$ (cm)	≤ 5.0	≤ 5.0	—
χ^2_{strip}	≤ 10.0	≤ 15.0	—
$\chi^2_{3\times3}$	—	—	≤ 3.0
VTX Occupancy	—	—	≥ 0.5

Table 5.2: Selection criteria for CMU/P, CMX, and CMIO muons. Muon candidates are categorized as Tight Central Muon (TCM), Loose Central Muon (LCM), Loose eXtension Muon (LXM) and Loose CMIO Muon (LMI).

Lepton	Tight	Loose		
Cut variables	TCM	LCM	LXM	LMI
p_T (GeV/c)	≥ 7.5	≥ 2.8	≥ 2.8	≥ 10
E_{EM} (GeV)	≤ 2.0	≤ 2.0	≤ 2.0	≤ 2.0
E_{HAD} (GeV)	≤ 6.0	≤ 6.0	≤ 6.0	≤ 6.0
d_0 raw (cm)	≤ 0.5	≤ 0.8	≤ 0.8	≤ 0.8
CMU Matching	$\|\Delta x\| \leq 2$ cm or $\chi^2_{CTC} \leq 9$	$\|\Delta x\| \leq 2$ cm or $\chi^2_{CTC} \leq 9$	—	—
CMP Matching	$\|\Delta x\| \leq 5$ cm or $\chi^2_{CTC} \leq 9$	$\|\Delta x\| \leq 5$ cm or $\chi^2_{CTC} \leq 9$	—	—
CMX Matching	—	—	$\|\Delta x\| \leq 5$ cm or $\chi^2_{CTC} \leq 9$	—

p_T is the transverse momentum of the track associated with the electron candidate measured in the CTC. A p_T cut is applied only to CEM electron candidates since PEM electrons will not travel through the entire CTC thus their p_T measurement is not accurate.

E_T is the transverse energy of the electromagnetic calorimeter cluster associated with the electron candidate.

E/p is the ratio of the electron candidate's energy to its momentum. The electron candidate of interest has energies in the GeV scale thus its momentum is about the same as its energy. The $E/p < 2$ requirement assures that the electron energy and its momentum agree and allows rejection of photons from π^0 decays. E/p cut is not applied to PEM electrons.

E_{HAD}/E_{EM} is the ratio of the hadronic energy to the electromagnetic energy associated with the cluster. For electrons, most of the energy is deposited in the electromagnetic calorimeter so we require $E_{HAD}/E_{EM} \leq 0.05$ for a tight electron, $E_{HAD}/E_{EM} \leq 0.055 + 0.045 \times \frac{E}{100}$ for a loose CEM and $E_{HAD}/E_{EM} \leq 0.1$ for a loose PEM. The sliding cut for loose CEM electrons is chosen with a historical reason and it allows electron candidates to have greater average energy leakage with higher energies. The constant term dominates for low energy electrons and the cut is always looser than the fixed cut used for the tight electron.

L_{SHR} is the lateral shower profile of the electromagnetic shower. To take into account the fact that electron showers sometimes spread over more than one

electromagnetic tower, we define variable L_{SHR} to be

$$L_{SHR} \equiv 0.14 \sum_i \frac{E_i^{\mathrm{adj}} - E_i^{\mathrm{prob}}}{\sqrt{0.14^2 E + (\Delta E_i^{\mathrm{prob}})^2}}$$

where E_i^{adj} and E_i^{prob} are the measured and expected energy in a tower adjacent to the seed tower, $0.14\sqrt{E}$ is the uncertainty of the energy measurement, $\Delta E_i^{\mathrm{prob}}$ is the uncertainty of the energy estimate, E_i^{prob} is calculated using a parameterization from test beam data, and the sum goes over all towers in the electromagnetic cluster. All energies are measured in GeV. Hadrons generally have different shower profiles from electrons, and thus are rejected by this cut. L_{SHR} cut is not applied to PEM electrons.

$|\Delta x|$ **and** $|\Delta z|$ are the track to shower matching variables. An alignment corrected CTC track is extrapolated to the Central Electromagnetic Strip chambers (CES) and compared with the shower position. $|\Delta x|$ is the matching in the $r - \phi$ plane and $|\Delta z|$ is the matching in the z direction. Background from overlapping neutral or charged hadrons can be rejected by requiring a good matching. This cut is not applied to PEM electrons.

χ^2_{strip} is the strip chamber profile comparison variable. It is a fit of the energy deposited in the CES strips using the 11 strips in z-direction per CES chamber to the profile determined during the test beam. χ^2_{strip} cut ensures that the electron candidate exhibits the same characteristics as its test beam counterpart. This cut is not applied to PEM candidates.

$\chi^2_{3\times3}$ is a fit of the lateral sharing of energy in the three towers in η by the three towers in ϕ around the electron cluster's center to the profile determined during the test beam. This cut is applied only to PEM electrons.

VTX occupancy is the ratio of layers in the VTX where the electron deposits energy to the number of layers where the electron should deposit energy according to its trajectory. We use this cut to ensure the presence of a charged track, thus reject photons from the PEM electron candidates. VTX occupancy cut is only applied to PEM candidates.

Muon Identification Cuts The muon identification cuts are based on information obtained from the CTC and the muon chambers. The calorimeter data is also used for verification of a minimal ionizing particle passing through the detector.

p_T is the transverse momentum of the track associated with the muon candidate as measured by the CTC. Note that the CMIO cut is 10 GeV/c since the CMIO bank is created for tracks with $p_T \geq 10$ GeV/c.

E_{EM}, E_{HAD} is the energy deposited in the electromagnetic and hadronic calorimeters respectively. A high p_T muon will not deposit substantial amounts of energy in any calorimeter. The hadronic calorimeters contain more absorber material than the electromagnetic calorimeters so a muon could deposit more energy in hadronic calorimeters than electromagnetic calorimeters.

d_0 **raw** is the muon impact parameter, *i.e.* the distance of the closest approach of the reconstructed muon track to the beam line. It requires the muon to originate from near the nominal interaction region. This cut mainly rejects cosmic muons in the sample.

Matching requires a good match between the extrapolation of the CTC track and the muon chamber stub. We require that either the $r-\phi$ distance between the extrapolation of the CTC track and the muon stub ($|\Delta x|$) be less than 2 cm

for CMU and 5 cm for CMP/CMX, or the χ^2_x of a fit from the CTC track to the muon stub be less than 9.0. This cut is not applied to CMIO muons.

5.2 Run IB Trilepton Skimming Selection

Next we require that events have a third lepton passing loose requirements listed in Table 5.1 (electron) or Table 5.2 (muon). Thus our trilepton skimming selection requires:

- At least one central lepton (CEM, CMU, CMP) passing tight requirements listed in Table 5.1 (electron) or Table 5.2 (muon).
- Two additional leptons (CEM, PEM, CMU, CMP, CMX, CMIO) passing loose requirements listed in Table 5.1 (electron) or Table 5.2 (muon).

A total of 15,149 events passed our trilepton skimming cuts. This sample is referred as the loose trilepton sample.

5.3 Run IB Trilepton Analysis Selection

Our skimmed trilepton data sample still contains a significant fraction of events that are not candidates for our search. We further clean up our sample by imposing tighter identification cuts listed in Tables 5.3 and 5.4 for electrons and muons.

Electron identification cuts

E_T is increased from 8 GeV to 11 GeV for the tight electron and from 4 GeV to 5 GeV for the loose electron. This change will reject more background events with minimal effect on signal acceptance.

Table 5.3: Analysis lepton selection cuts for CEM and PEM electrons.

Lepton	Tight	Loose	
Cut variables	TCE	LCE	LPE
E_T (GeV)	≥ 11	≥ 5	≥ 5
E/p	≤ 2	≤ 2	—
HAD/EM	≤ 0.05	$\leq 0.055 + 0.045 \times \frac{E}{100}$	≤ 0.1
L_{SHR}	≤ 0.2	≤ 0.2	—
$\lvert\Delta x\rvert$ (cm)	≤ 3	≤ 3	—
$\lvert\Delta z\rvert$ (cm)	≤ 5	≤ 5	—
χ^2_{strip}	≤ 10	≤ 15	—
$\chi^2_{3\times3}$	—	—	≤ 3
VTX occupancy	—	—	≥ 0.5
Conversion removal	Yes	Yes	Yes
Fiducial Area	Yes	Yes	Yes

Table 5.4: Analysis lepton selection cuts for CMU/P, CMX and CMIO muons.

Lepton	Tight	Loose		
Cut variables	TCM	LCM	LMX	LMI
p_T (GeV/c)	≥ 11	≥ 4	≥ 4	≥ 10
EM (GeV)	≤ 2	≤ 2	≤ 2	≤ 2
Had (GeV)	≤ 6	≤ 6	≤ 6	≤ 6
d_0 raw (cm)	≤ 0.5	≤ 0.8	≤ 0.8	≤ 0.8
d_0 beam (cm)	≤ 0.2	≤ 0.5	≤ 0.5	≤ 0.5
CMU Matching	$\lvert\Delta x\rvert \leq 2$ cm or $\chi^2_{CTC} \leq 9$	$\lvert\Delta x\rvert \leq 2$ cm or $\chi^2_{CTC} \leq 9$	—	—
CMP Matching	$\lvert\Delta x\rvert \leq 5$ cm or $\chi^2_{CTC} \leq 9$	$\lvert\Delta x\rvert \leq 5$ cm or $\chi^2_{CTC} \leq 9$	—	—
CMX Matching	—	—	$\lvert\Delta x\rvert \leq 5$ cm or $\chi^2_{CTC} \leq 9$	—
EM+Had (GeV)	≥ 0.1	≥ 0.1	≥ 0.1	≥ 0.1
Not Fiducial Area	—	—	—	Yes

Conversion removal is to remove electrons that are from photon conversion. An electron is rejected if there are two opposite-sign tracks pointing to the electron cluster, since it is likely to be a photon that converted into a pair of electron and positron.

Fiducial Area requires the electron is in a region that CEM or PEM is known to function well.

Muon identification cuts

p_T is increased from 7.5 GeV to 11 GeV/c for tight CMU/P muon and from 2.8 GeV/c to 4 GeV/c for loose CMU/P or CMX muon. This change will reject more background events with minimal effect on signal acceptance.

d_0 **raw** is the muon impact parameter *i.e.* the distance of the closest approach of the reconstructed muon track to the beam line. In early CDF trilepton analysis [45, 46] this cut is tightened from 0.8 cm to 0.5 cm for loose CMU/P, CMX or CMIO muons, however it is not necessary to tighten this cut because a d_0 beam cut will be used. Later multi-lepton analysis did not tighten d_0 raw cut, and we do not tighten this cut in this analysis either.

d_0 **beam** is the beam constrained impact parameter which is determined by using the beam position (in z). We require a tight CMU/P muon to have d_0 beam ≤ 0.2 cm and a loose CMU/P, CMX or CMIO muon to have d_0 beam ≤ 0.5 cm.

EM + Had requires the muon deposit at least 100 MeV in the calorimeters.

Not Fiducial Area requires that a CMIO muon does not point at a muon chamber, since it would have made a muon stub otherwise.

All of these requirements are the same as used in the CDF trilepton analysis [45, 46] except those we have mentioned above (isolation requirement and d_0 raw). After the 3 lepton analysis requirements we are left with 1120 events. This sample is referred as the tight trilepton sample.

Chapter 6

Standard Model Backgrounds

There are several SM processes which can produce a multi-lepton final state. The main source of multi-lepton events are events with three or more real leptons, and events with two real leptons plus a misidentified lepton. This misidentified lepton [1] may come from unrelated parts of the event, e.g. a real lepton from the underlying event, or a hadronic track misidentified as a lepton. Events with three real leptons include $W^{\pm}Z^0$, Z^0Z^0, $t\bar{t}$ and $b\bar{b}$. Events with two real leptons include $W^{\pm}W^{\mp}$, $c\bar{c}$ and Drell-Yan (γ^* and Z^0). Some of these background sources have very small production cross sections while other backgrounds have distinctive signatures. In addition, cosmic rays constantly passing through our detector and manifest themselves as dimuon events with back-to-back CTC tracks, thus become a potential background in our analysis [2]. By comparing the kinematics of signal and background events, we can use a series of cuts to reject background with minimal effect on signal acceptance.

In order to determine the contribution of real leptons from the SM processes to the signal we used the CDF SUSY group MC samples (Appendix B). In this chapter

[1] Sometimes we call misidentified leptons "fake" leptons since they are not the leptons of our interests.

[2] CDF Run IB detector simulation program QFL does not properly simulate cosmic muons.

the branching ratio numbers are from the Particle Data Group [49]. The cross section numbers for $b\bar{b}$ and boson pair production are from theoretical calculations and for $t\bar{t}$ and Drell-Yan are from CDF measurements [50, 51, 52, 53, 54, 55, 56, 57, 58].

6.1 Real Multi-Lepton events

Processes that can produce three or more real leptons include

1. $b\bar{b}$ Production
2. $t\bar{t}$ Production
3. Dibosons (ZZ, WZ) Production

In our analysis we count real multi-lepton background events by requiring at least one central lepton passing tight requirements listed in Table 5.3 or Table 5.4 and two additional leptons passing loose requirements listed in Table 5.3 or Table 5.4. [3]

$b\bar{b}$ Production The $b\bar{b}/c\bar{c}$ productions are illustrated in Figure 6.1. A b quark can decay via $b \to Wc \to W(Wd)$. Each W has 11% chance of decaying to an e and 11% chance of decaying to a μ. Thus the probability of both Ws decay leptonically is about 4%. If either of the W from the $\bar{b}$ also decays leptonically, we will have three real leptons in the event. Since b quarks are produced at the Tevatron abundantly (the production cross section for $b\bar{b}$ is very high: $\sigma = 3.52 \pm 0.38(stat) \pm 0.46(syst)$ μb [50, 51]), $b\bar{b}$ can be a substantial background. We are able to remove most $b\bar{b}$ (and $c\bar{c}$) background by requiring the invariant mass of the two closest[4]

[3] It is possible that events with a hadron passing the lepton ID requirements are included and those events will be removed with later cuts.

[4] We calculated the spatial angles between any two of the three lepton candidates regardless of charge or flavor, and choose the two leptons that form the smallest angle to calculate the invariant mass. The two closest leptons are most likely to be from the same b quark. The invariant mass is $m(l_1, l_2) = \sqrt{(E(l_1) + E(l_2))^2 - |\vec{p}(l_1) + \vec{p}(l_2)|^2}$.

leptons to be greater than 5 GeV/c^2 (see Fig.8.1), since the invariant mass of the two leptons coming from the same b hadron is less than 5 GeV/c^2.

Since the MUED signal event has at least one opposite sign pair of the same flavor leptons (*i.e.* a $\mu^+\mu^-$ or e^+e^- pair), while the flavor of the leptons from the b and c decays are not correlated, we require at least one opposite sign pair of the same flavor leptons to further reduce $b\bar{b}/c\bar{c}$ background in the invariant mass > 5 GeV/c^2 region.

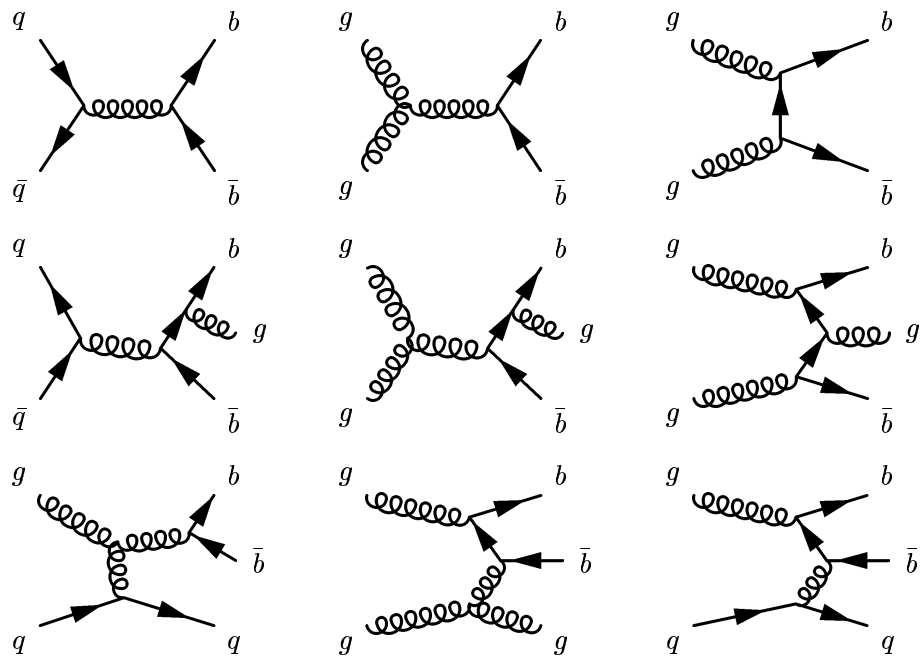

Figure 6.1: The Feynman diagrams for leading and some higher order production of $b\bar{b}$. The production of $c\bar{c}$ is obtained by replacing b with c.

$t\bar{t}$ Production The production of $t\bar{t}$ is illustrated in Figure 6.2. A top quark can decay via $t \to W^{\pm}b$. We can get up to two leptons from the $W^{\pm}$ decays (one from the t and the other from the $\bar{t}$) and at least a third lepton from the semi-leptonic decay of a b quark. The production cross section for $t\bar{t}$ is $6.5^{+1.7}_{-1.4}$ pb [52], so small that this background is negligible.

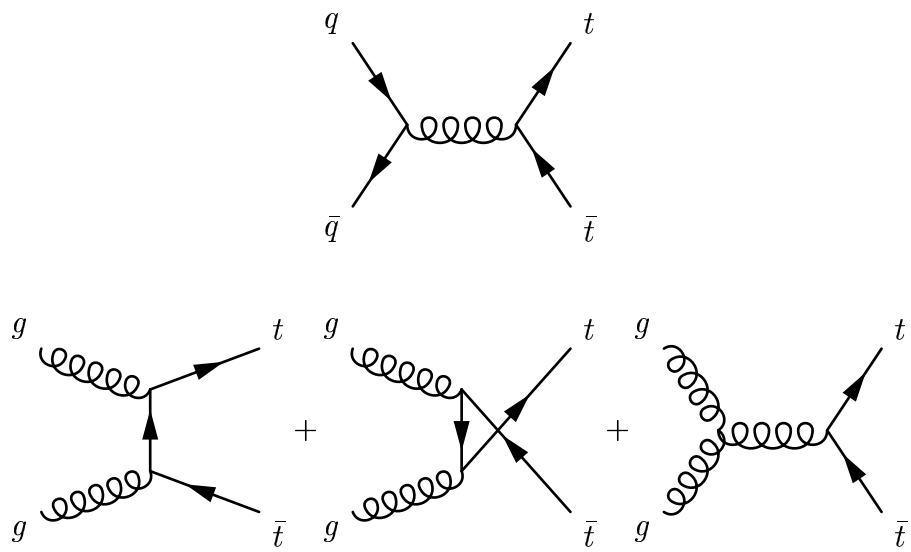

Figure 6.2: The Feynman diagrams of tree-level $t\bar{t}$ production.

Diboson Production: Z^0Z^0 and $W^{\pm}Z^0$ Some higher order weak diboson productions are illustrated in Figure 6.3. Both the production cross section of Z^0Z^0 ($\sigma(ZZ) = 1.08$ pb [53, 56], BR = 0.45% to e or μ) and $W^{\pm}Z^0$ ($\sigma(WZ) = 2.5$ pb [54, 56], BR = 1.44% to e or μ) and the branching ratio to three lepton final states are small. However this background produces a signature very similar to the MUED signal, so we need to remove this background. A Z^0 is contained in both types of productions, so we can use a Z^0 mass window cut to remove them. We remove an event if any same-flavor opposite-sign lepton-pair two-body masses are in the range 76 GeV/c^2 $\leq M_{\ell\ell} \leq$ 106 GeV/c^2.

6.2 Dilepton Plus Misidentified Lepton Events

Processes which can produce two real leptons include Drell-Yan (γ^* and Z^0) and W^+W^- production.

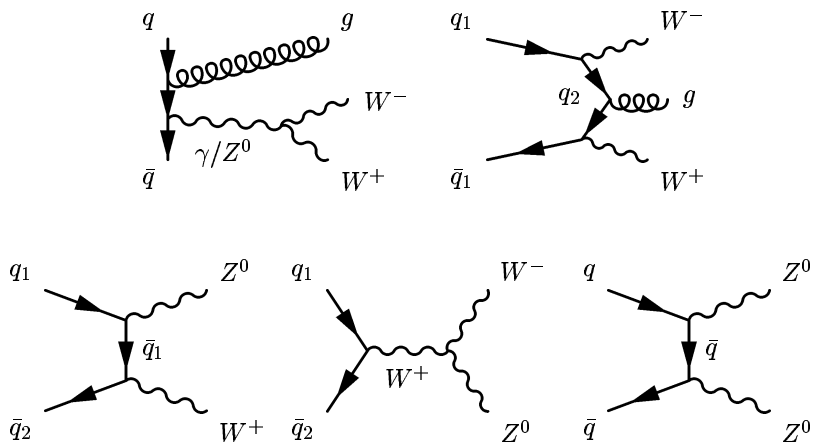

Figure 6.3: The Feynman diagrams of some higher order weak diboson production.

Drell-Yan (Z^0 and γ^*) Production The Feynman diagrams for leading and some higher order Drell-Yan productions are shown in Figure 6.4. The Drell-Yan background can be split up into three categories: γ^* production ($\overline{q}q \rightarrow \gamma^* \rightarrow l^+l^-$), low-$p_T$ and high-p_T Z^0 production ($\overline{q}q \rightarrow Z^0 \rightarrow l^+l^-$). The high mass Drell-Yan events (with Z^0 mediator) production cross section from the CDF published measurement is: $\sigma(Z^0) = 6.94 \pm 0.53$ nb and $\sigma \cdot Br(Z^0 \rightarrow \mu^+\mu^-) = 233 \pm 18$ pb [57]. The low mass Drell-Yan events (with γ^* mediator) production cross section from the CDF published measurement is 259 ± 57 pb [58]. Events from γ^* production can be removed with an opening angle cut. Low-p_T Z^0 will produce leptons that are back-to-back, so they can also be removed with an opening angle cut. Leptons from high-p_T Z^0 decays will not be back to back so we remove them with a Z^0 mass window cut.

To remove this type background, we require the opening angle between the two highest p_T leptons be less than 2.96 radians (170°). In addition we require the event not have a same-flavor opposite-sign lepton-pair two-body mass in the range 76 GeV/c^2 $\leq M_{\ell\ell} \leq$ 106 GeV/c^2.

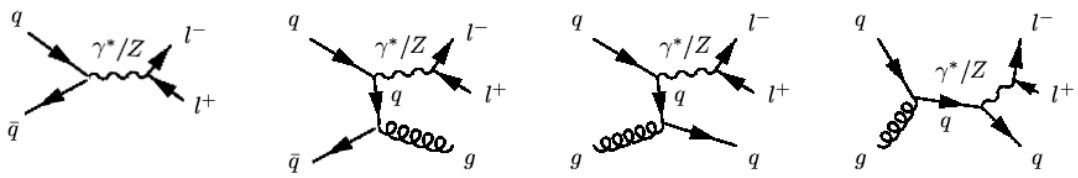

Figure 6.4: The Feynman diagrams for leading and some higher order Drell-Yan production.

W^+W^- Production W^+W^- production has a small production cross section ($\sigma(WW) = 9.53$ pb [55, 56]). Each $W^\pm$ can decay to either an electron or a muon, consequently W^+W^- decays will produce only two real leptons, thus a fake lepton must be present in an event to be accepted. The probability of such an event occurring our sample is very small. Furthermore, we reduce W^+W^- background by 50% by requiring the event to have a $\mu^+\mu^-$ or e^+e^- pair, since each $W^\pm$ has equal probability to decay to either an electron or a muon.

Measurement of the misidentified lepton rate The calculation of misidentified lepton rate can be carried out based on the overall number of events or on an event-by-event basis. In this analysis we use the first approach to estimate the misidentified lepton rate.

A study based on the $W^\pm$ sample [59] was performed in the CDF-trilepton analysis [46]. First, the *CleanW* analysis module prepares a sample of 16,596 $W^\pm$ events where the only leptons expected are from $W^\pm$ decays (10,861 $W^\pm \to e\nu$ events and 5,735 $W^\pm \to \mu\nu$ events) [5]. Next, the *LeptCount* analysis module counts the leptons,

[5]The W events are required to have leptons with the same tight lepton selection criteria and additional requirements:

- a lepton with $\mathrm{p_T} > 20$ GeV/c,
- missing transverse energy $\not\!\!E_T > 20$ GeV,
- a transverse mass of lepton: 40 GeV/c^2 $< M_T(\mathrm{p_T}, \not\!\!E_T) <$ 100 GeV/c^2.

apart from the $W^{\pm}$ leptons. 48 fake leptons were found by LeptCount, never more than one per event. Thus the probability that a $W^{\pm}$ event will contain a fake lepton is 0.289%±0.042%. Since no events with two fake leptons were found, background from (single lepton + two fakes) is not considered.

The fake lepton rate has been re-examined in the CDF multi-lepton analysis [60]. In this study leptons are not required to be isolated, and as a result a higher number of fake leptons are found: 68 events containing CEM electrons and 73 events containing CMUO muons out of 17,336 events passing CleanW filter. Thus the fake lepton rate is 0.81%±0.07%.

Assuming no p_T dependence on the rate of fake leptons, we use 0.81%±0.07% as the probability that any event will have a fake lepton.

To calculate the number of multi-lepton events due to (dilepton + fake) we require one tight lepton and one loose lepton. We then use the probability of each event having a fake lepton times the number of dilepton events as the number of expected background due to (dilepton + fake).

Chapter 7

Monte Carlo Simulations

Monte Carlo (MC) simulation is a commonly used and important technique. It attempts to include all theoretical and experimental knowledge and uses computer programs to generate events of the physical processes of our interests. It is called Monte Carlo technique because random numbers are used in the simulation programs.

In this analysis we use the Monte Carlo technique to obtain a large number of events of both the MUED signal and the SM background processes. Event generators (ISAJET [61], PYTHIA [62], etc.) simulate the desired process and write the events to a generator level data bank [1] which contains momentum, energy, flavor, charge, parent, daughter etc. information for every particle generated in the event. The event generation is done in the CDF Run II framework. [2] CDF Run II uses ROOT data format while CDF Run I uses YBOS data format. The conversion between ROOT format and YBOS format can be done using standard CDF Run II module BankTools [3]. Detector effects (such as resolution and smearing) are addressed by

[1] GENP bank for ISAJET and HEPG bank for PYTHIA.

[2] This study began as a CDF Run II analysis thus the MUED Monte Carlo event generation was done in the CDF Run II framework. However the Run II was behind schedule, while the Run I data is valuable yet not analyzed for MUED study. So later this study became a Run I data analysis.

[3] http://cdfkits.fnal.gov/CdfCode/source/BankTools/

detector simulation. All simulated events used in this analysis were processed with a fast CDF detector simulation software QFL [63]. After generation and QFL detector simulation, the events have the same format as data taken with the detector. Thus we can use the same program to analyze both data and Monte Carlo events.

7.1 The MUED Signal Simulation

We have studied the MUED scenario by using Pythia 6.203 to produce MC samples with various radii of the extra dimension R^{-1} (see Appendix C for an example Pythia tcl file). We used the default Pythia structure function CTEQ-5L [64]. In order to reduce the statistical uncertainties, at each MC point we generated about 25,000 signal events (more than 200 times larger than we would expect in our actual data).

We examined mass spectra of $n = 1$ KK particles for different choices of R^{-1} and Λ as listed in Table 7.1. The relevant formulas used to calculate the radiative corrections to KK masses are listed in Appendix A.

Table 7.1: MUED Monte Carlo points for $n = 1$ KK particles of different values of R and ΛR. The Higgs mass is fixed at $m_h = 120$ GeV. The relevant formulas used to calculate the radiative corrections to KK masses are listed in Appendix A.

R^{-1}	ΛR	M_{γ_1}	M_{L_1}	M_{W_1}	M_{Z_1}	M_{Q_1}	M_{g_1}
250	20	250.3	257.0	276.6	276.9	298.4	320.5
250	50	250.4	259.1	280.7	281.0	313.2	339.1
300	20	300.3	308.3	327.6	327.8	358.1	384.6
300	50	300.3	310.9	332.6	332.8	375.8	406.9
350	20	350.3	359.7	379.1	379.2	417.7	448.7
350	50	350.3	362.7	385.1	385.2	438.5	474.8
400	20	400.2	411.1	431.0	431.1	477.4	512.7
400	50	400.2	414.5	437.8	437.9	501.1	542.6
450	20	450.2	462.5	483.1	483.2	537.1	576.8
450	50	450.2	466.3	490.8	490.9	563.7	610.4
500	20	500.2	513.9	535.4	535.4	596.8	640.9
500	50	500.2	518.2	543.9	544.0	626.4	678.2

We are interested in 3-lepton (from $W_1^{\pm}Z_1$) or 4-lepton (from Z_1Z_1) events. With effective branching fraction of $B(Q_1 \rightarrow W_1^{\pm}Q_0') \sim 80\%$ and $B(Q_1 \rightarrow Z_1Q_0) \sim 20\%$, a KK quark pair will have a 4% chance decay to Z_1Z_1 pair, a 32% chance decay to $W_1^{\pm}Z_1$ pair, and a 64% chance decay to $W_1^{\pm}W_1^{\mp}$ pair.

Figure 7.1, 7.2, 7.3, 7.4 shows the distribution of important kinematic variables for the MUED signal events at R^{-1}=350 GeV.

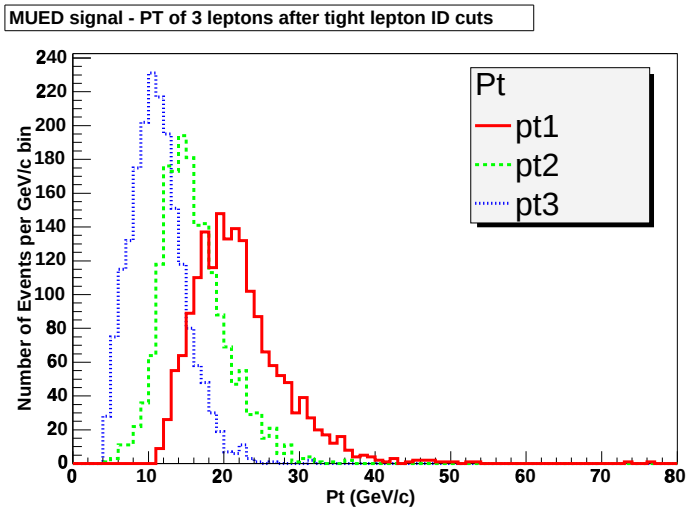

Figure 7.1: MUED signal MC transverse momentum of three leptons after tight lepton cuts (as described in Section 5.3). pt1, pt2, pt3 are the transverse momenta of the three leptons from the highest to the lowest transverse momentum respectively.

7.2 The Standard Model Background Simulation

The SUSY working group has generated large background Monte Carlo samples for Run IB analyses with ISAJET version 7_06 and 7_20. Five different structure functions have been used in the generation. Each MC sample corresponds to a different integrated luminosity and the number of MC events need to be scaled before comparing with the data. The contribution of background in each category ($b\bar{b}/c\bar{c}$, Drell-Yan, boson pair, $t\bar{t}$) is obtained by averaging over structure functions and then

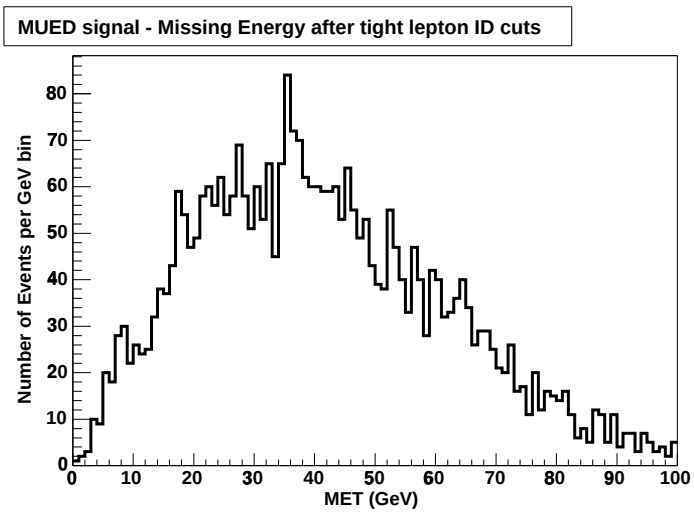

Figure 7.2: MUED signal MC missing energy after tight lepton cuts (as described in Section 5.3).

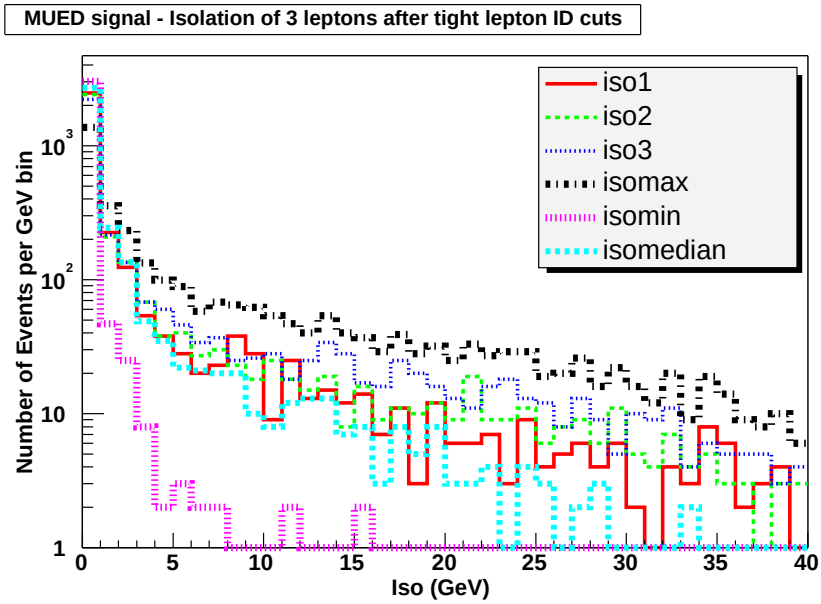

Figure 7.3: MUED signal MC isolation of three leptons after tight lepton cuts (as described in Section 5.3). Isolation is defined as the energy in a cone of $\Delta R \equiv \sqrt{\Delta\phi^2 + \Delta\eta^2} = 0.4$ minus the electron or muon energy. iso1, iso2, iso3 are the isolations of the three leptons from the highest to the lowest transverse momentum respectively. isomax, isomin and isomedian are the maximum, minimum and median of the three isolations respectively.

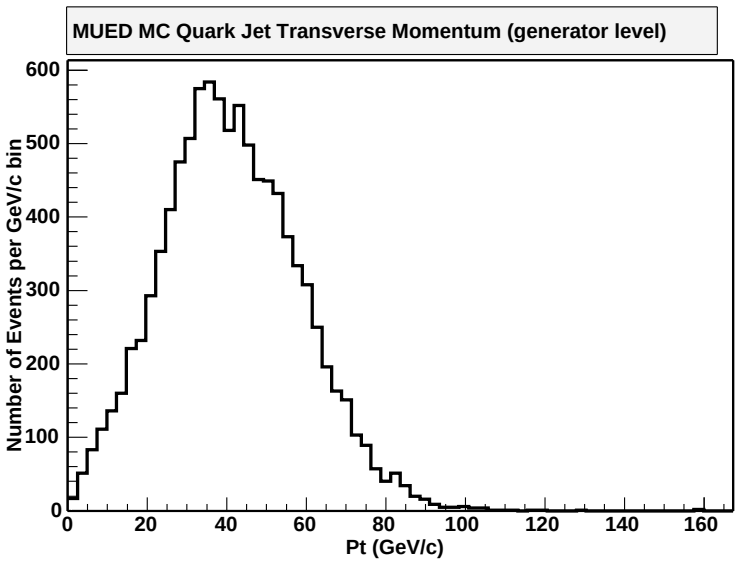

Figure 7.4: MUED signal MC transverse momentum of the quark jets from decays of SU(2)-doublet KK quarks.

summing over runs. The total expected background is the sum of all categories. For details on SUSY working group Run IB SM background simulation see Appendix B.

7.3 Monte Carlo Efficiency Corrections

Our detector simulation program QFL does not model trigger efficiencies or isolation efficiencies, and tends to be over-efficient in lepton identification. Thus we need to determine those corrections and apply them to both signal and background MC events.

7.3.1 Trigger Efficiencies

The data needs to pass various triggers to enter the final data set. In order to compare MC events with data, we need to check each lepton candidate of the MC event to determine which triggers it would have most likely activated.

A trigger efficiency study has been done in Ref. [46]. Each individual trigger's efficiency is coded into trigger simulation routine MC_WGT. The trigger efficiency correction of the MC events are determined on an event-by-event basis: for each event, the lepton candidate's E_T (P_T) and η are examined, and the routine MC_WGT returns the Level 1 trigger efficiency, the Level 2 trigger efficiency and the Level 3 trigger efficiency. The total trigger efficiency of this MC event is the product of three different trigger level efficiencies, and it is the weighting factor that needs to be applied to this event. The trigger efficiency correction is applied to both the background and signal MC calculation.

7.3.2 Lepton Identification Efficiencies

QFL tends to overestimate the lepton identification efficiency due to not including subtle detector efforts (such as detector aging). The efficiency corrections including lepton identification, conversion electron removal, "good" CTC track requirement, and cosmic muon removal have been studied in Ref. [65].

In Table 7.2 we summarize the detector-by-detector detection efficiencies for data and MC, and correction factors. We want to obtain an overall lepton identification efficiency correction factor that will be applied to every MC event, rather than an event-by-event correction since the differences are small. We take the most conservative approach and combine the correction factors that will give us the largest correction (that deviates from 1). For our analysis, an event with a central electron that passes the tight lepton ID cuts, and two loose electrons that pass the loose electron ID cuts will likely have the largest correction. The overall correction factor is 0.86±0.02 (±2%) ($0.944 \times 0.954 \times 0.954 = 0.86$, $\sqrt{(1.08\%)^2 + (1.00\% + 1.00\%)^2} = 2\%$, $0.86 \times 2\% = 0.02$). This factor is applied to both the background and signal MC calculation.

Table 7.2: Summary of efficiencies including lepton identification, photon-conversion removal (TCE and LCE only), "good" CTC track (not LPE), and cosmic ray removal (muons only). data/MC is used to calculate the efficiency correction factor for the Monte Carlo. Leptons are categorized by Tight Central Electron (TCE), Loose Central Electron (LCE), Loose Plug Electron (LPE), Tight Central Muon (TCM), Loose Central Muon (LCM), Loose eXtension Muon (LXM) and Loose CMIO Muon (LMI). Table 16 of Ref. [65] lists Eff. (Drell-Yan MC) and Eff. (Run IB Z^0 inclusive electron and muon data sample) with absolute uncertainties, we have calculated IB/MC and all relative uncertainties in this table.

	Eff. (Drell-Yan MC)	Eff. (Run IB Z^0 data sample)	Correction (data/MC)
TCE	0.863 ± 0.004 (0.46%)	0.815 ± 0.008 (0.98%)	0.944 ± 0.010 (1.08%)
LCE	0.888 ± 0.003 (0.34%)	0.847 ± 0.008 (0.94%)	0.954 ± 0.010 (1.00%)
LPE	0.924 ± 0.004 (0.43%)	0.920 ± 0.007 (0.76%)	0.996 ± 0.009 (0.87%)
TCM	0.977 ± 0.003 (0.31%)	0.929 ± 0.007 (0.75%)	0.951 ± 0.008 (0.81%)
LCM	0.976 ± 0.003 (0.31%)	0.937 ± 0.006 (0.64%)	0.960 ± 0.007 (0.71%)
LMX	0.957 ± 0.005 (0.52%)	0.929 ± 0.010 (1.08%)	0.971 ± 0.012 (1.19%)
LMI	0.880 ± 0.008 (0.91%)	0.912 ± 0.014 (1.54%)	1.036 ± 0.019 (1.79%)

7.3.3 Isolation Efficiencies

During CDF Run IB data taking period, multiple interactions occur at high instantaneous luminosity, which can affect the lepton isolations [4] but are not considered by QFL simulation. Therefore a correction factor (the ratio of MC and data isolation efficiency) must be applied to all MC events. Efficiencies of calorimeter and track isolation cuts for leptons are determined using the Run IB Z^0 events in Ref. [66]. For calorimeter isolation cuts at 4 GeV with the presence of 2 jets, the isolation correction factors for electrons and muons can be obtained from comparing the last columns of Table 7.3 and Table 7.4. We are cutting on the maximum isolation of the three lepton candidates for our analysis, thus an event with a muon having the maximum isolation will result in the largest isolation efficiency correction of 0.92 (0.904/0.980),

[4] Isolation in this analysis is defined as the total energy in a cone (with cone size $\Delta R \equiv \sqrt{\Delta\phi^2 + \Delta\eta^2} = 0.4$) minus the energy of electron or muon.

with relative uncertainty of 4.7% ($\sqrt{(0.041/0.904)^2 + (0.011/0.980)^2} = 4.7\%$). We only apply isolation requirement at the final stage of our analysis.

Table 7.3: Summary of calorimeter isolation efficiency $ISO^{cal} < 4$ GeV for jet multiplicity of cone size R = 0.7 (0.4) of Run IB Z^0 data events. From Table 9 of Ref. [66].

Object	$\eta_j^{0.7(0.4)} = 0$	$\eta_j^{0.7(0.4)} = 1$	$\eta_j^{0.7(0.4)} \geq 2$
e^{CEM}	0.970 ± 0.005 (0.970 ± 0.004)	0.958 ± 0.010 (0.956 ± 0.012)	0.953 ± 0.021 (0.936 ± 0.028)
e^{PEM}	0.981 ± 0.003 (0.977 ± 0.004)	0.962 ± 0.009 (0.967 ± 0.010)	0.941 ± 0.022 (0.971 ± 0.020)
μ	0.970 ± 0.005 (0.971 ± 0.005)	0.967 ± 0.010 (0.966 ± 0.011)	0.937 ± 0.027 (0.904 ± 0.041)

Table 7.4: Summary of calorimeter isolation efficiency $ISO^{cal} < 4$ GeV for jet multiplicity of cone size R = 0.7 (0.4) of ISAJET+QFL Drell-Yan MC events. From Table 13 of Ref. [66].

Object	$\eta_j^{0.7(0.4)} = 0$	$\eta_j^{0.7(0.4)} = 1$	$\eta_j^{0.7(0.4)} \geq 2$
e^{CEM}	0.981 ± 0.002 (0.991 ± 0.002)	0.987 ± 0.004 (0.990 ± 0.004)	0.967 ± 0.012 (0.994 ± 0.006)
e^{PEM}	0.995 ± 0.001 (0.995 ± 0.001)	0.993 ± 0.002 (0.995 ± 0.003)	0.985 ± 0.009 (0.991 ± 0.009)
μ	0.986 ± 0.002 (0.989 ± 0.002)	0.991 ± 0.003 (0.985 ± 0.004)	0.991 ± 0.008 (0.980 ± 0.011)

Chapter 8

Data Analysis

Our analysis includes the identification of events with three good leptons and the rejection of the Standard Model background events.

8.1 Bad Run Removal

In addition to the lepton identification cuts there are several new constraints. Our data sample includes events from runs in which part of the detector was turned off or the data were taken with bad beam conditions. All events from these runs were rejected using the CDF standard offline routine BADRUN [67]. This routine checks a database containing information about the state of the detector during a data taking run. We only accept runs for which BADRUN reports a fully operational detector.

After removing bad runs we are left with 1068 events.

8.2 Cosmic Ray Removal

Cosmic rays are constantly passing the atmosphere and they create showers of particles which often decay to muons. These muons passing through our detector are a

substantial background to our analysis.

From the detector's point of view, a cosmic ray manifests itself as a dimuon event with CTC tracks that are back-to-back in η and ϕ, and often has a large impact parameter. In addition, since the cosmic ray travels through the detector (rather than originating at the interaction point and travelling outward), the difference in the timing signals measured by the Time to Digital Converter (TDC) for the two legs will be roughly equal to the speed-of-light transit time from one side of the calorimeter to the other.

Two techniques are used to remove cosmic rays: a CDF standard routine CMCOS [68] and a custom routine that examines the opening angle between the muons[1] and the difference in the time when each particle passed through the hadron calorimeter[2].

CDF Run IB detector simulation program QFL does not properly simulate the hadron calorimeter TDC. Therefore cosmic ray removal is not applied to MC samples.

After cosmic removal, we are left with 750 events.

8.3 Vertex Requirements

The primary vertex for an event is the $p\bar{p}$ interaction point. We impose two vertex requirements:

- All three leptons have $z_{vertex} < 60$ cm, to ensure high quality tracks in the CTC.

- All three leptons are associated with tracks that are within 10 cm of the same

[1]Events are removed if the opening angle is greater than 3 radians

[2]The Hadron Time-to-Digital-Converters (HTDCs) are important for the removal of cosmic ray background by measuring the time elapsed between the firing of a discriminator in the hadron calorimeter and a common stop signal. The HTDCs have a 700 ns range and a 0.5 ns resolution. Events are removed if the difference in time for the two opposite muons is greater than 12 ns

z-vertex, to remove events with leptons that do not originate from the primary vertex. This is not applied to PEM electrons because they may not be associated with a good track.

After vertex requirements we are left with 683 events.

8.4 Charge Sum and Lepton Pair Requirements

Events of interest are 3-lepton ($W_1^{\pm}Z_1$ channel) or 4-lepton (Z_1Z_1 channel) events, thus we expect at least one e^+e^- or $\mu^+\mu^-$ pair from the three lepton candidates with their charges satisfying $|q_1 + q_2 + q_3| < 3$.

After charge sum and lepton pair requirements we are left with 545 events.

8.5 Invariant Mass Requirements

$b\bar{b}/c\bar{c}$ background events are a substantial background to our analysis (see Section 6.1). We require the invariant mass of the two closest [3] leptons to be greater than 5 GeV/c^2 (see Fig. 8.1). This allows us to reject $b\bar{b}/c\bar{c}$ background without sacrificing much of the signal. Our result shows that this cut also removes all e^+e^- or $\mu^+\mu^-$ events that originate from the J/ψ.

After invariant mass requirements we are left with 68 events.

By looking at Fig. 8.1, we noticed that in the invariant mass less than 5 GeV/c^2 region where $b\bar{b}/c\bar{c}$ background dominates, the background Monte Carlo and data do not agree with each other. The $b\bar{b}/c\bar{c}$ background was not modeled correctly because old structure functions were used, thus an overall scale factor needs to be applied

[3] We calculated the spatial angles between any two of the three lepton candidates regardless of charge or flavor, and choose the two leptons that form the smallest angle to calculate the invariant mass.

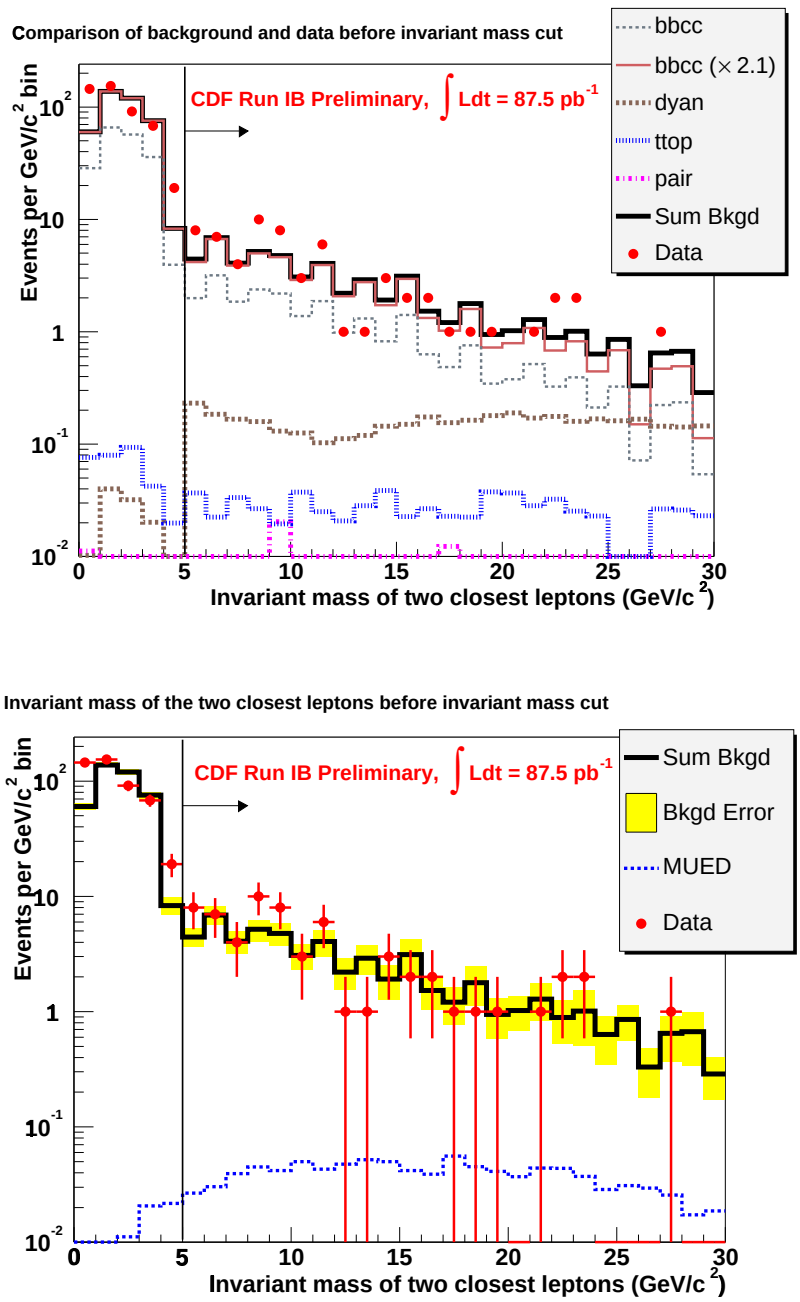

Figure 8.1: Distributions of invariant mass of the two closest leptons. The top figure shows data and each type of background. The bottom figures shows the MUED signal, data and the total background with error band. The scale factor 2.1 is applied to $b\bar{b}/c\bar{c}$ background, and the total background includes $b\bar{b}/c\bar{c}$ background with scale factor 2.1 applied, Drell-Yan, $t\bar{t}$, and boson pairs. The vertical straight lines indicate the cut value and the arrows indicate the accepted values. Background MC samples are generated by the SUSY working group (Appendix B).

to $b\bar{b}/c\bar{c}$ background. This scale factor is determined to be 2.1 (see Appendix D), which is then applied to the $b\bar{b}/c\bar{c}$ background over the entire mass range. For the remainder of this analysis the scale factor 2.1 is applied to $b\bar{b}/c\bar{c}$ background, and the total background includes $b\bar{b}/c\bar{c}$ background with scale factor 2.1 applied, Drell-Yan, $t\bar{t}$, and boson pairs.

8.6 Resonance Removal

So far our data sample still contains e^+e^- or $\mu^+\mu^-$ events that could originate from Z^0 boson or Υ.

These events are removed by an invariant mass cut for the e^+e^- or $\mu^+\mu^-$ pair: $9 \leq m(e^+e^- \; or \; \mu^+\mu^-) \leq 11$ GeV/c^2 for Υ, and $76 \leq m(e^+e^- \; or \; \mu^+\mu^-) \leq 106$ GeV/c^2 for Z^0. An event will be removed if any possible e^+e^- or $\mu^+\mu^-$ pair two-body masses (out of 3 lepton candidates) are in those ranges.

After resonance removal, we are left with 48 events.

8.7 $\Delta\phi_{\ell_1\ell_2}$ Requirements

The Drell-Yan background events from γ^* production and low-$\mathrm{p_T}$ Z^0 can be removed with an opening angle cut(see Section 6.2). We require the opening angle between the two highest $\mathrm{p_T}$ leptons be less than 2.96 radians (170°). See Fig. 8.2.

After $\Delta\phi$ requirements we are left with 43 events.

8.8 Lepton Candidates Combinations Selection

It is helpful to study the signal MC and the SM background distribution, and examine the three lepton candidates combinations. Fig. 8.3 and Fig. 8.4 show the number

of events in the eee, $ee\mu$, $e\mu\mu$, $\mu\mu\mu$ channels for the SM background and signal MC respectively and how they change after each cut [4].

After $\Delta\phi_{\ell_1\ell_2}$ cut, we have 0.64 signal events and 21.02 total background events in the non-$\mu\mu\mu$ channels (namely eee, $ee\mu$, and $e\mu\mu$), compared with 0.26 signal events and 22.99 total background events in the $\mu\mu\mu$ channel. Clearly the non-$\mu\mu\mu$ channels are the better choice for our analysis, therefore we veto $\mu\mu\mu$ events. Results from all channels including eee, $ee\mu$, $e\mu\mu$ and $\mu\mu\mu$ are summarized in Appendix E. Results from the $\mu\mu\mu$ channel are summarized in Appendix F. Fig. 8.5 and Fig. 8.6 show the invariant mass of the two closest leptons and the opening angle of the two highest transverse momentum leptons respectively, in the non-$\mu\mu\mu$ channels.

8.9 Final Optimization Cuts

After all the cuts above are applied, we still have background events remaining. We can further reduce these backgrounds by using isolation[5] and $\not{E}_T$ [6] cuts.

We use the Punzi [69] method to optimize

$$\mathbb{A} \equiv \frac{\epsilon(t)}{a/2 + \sqrt{B(t)}} \tag{8.1}$$

where t indicates the whole set of cuts, ϵ is the efficiency of the chosen cuts on the signal, a is the number of sigmas corresponding to one-sided Gaussian tests at

[4] All MC events are reconstructed and properly weighted for integrated luminosity, lepton ID efficiency, and trigger efficiency. We add 1 to the number of muons in the Drell-Yan MC events, assuming the fake (third) lepton is most likely a muon.

[5] A lepton's isolation is defined as the energy in a cone of $\Delta R \equiv \sqrt{\Delta\phi^2 + \Delta\eta^2} = 0.4$ minus the electron or muon energy. We require the maximum isolation of the three lepton candidates to be less than our isolation (ISO) cut value. We have considered using the medium or minimum isolation of the three lepton candidates, however the Punzi optimization procedure that we will introduce in this section shows that in order to achieve comparable result as using maximum isolation, the medium or minimum isolation cut has to be less than 1 GeV, which is clearly not a good choice.

[6] $\not{E}_T$ is missing transverse energy. Conservation of energy and momentum allows one to extract the energy and direction of non-interacting particles.

significance α, and B is the expected number of background events.

$\mathbb{A}$ is independent of the cross section of the new process, thus suitable for searches of new signals and the optimization of the cuts.

We conducted a 2-D search on a cut matrix (Table 8.1) with isolation range from 2 GeV to 10 GeV with a step size of 1 GeV, and $\not\!\!E_T$ range from 10 GeV to 30 GeV with a step size of 1 GeV.

Table 8.1: Optimization grid: rows - Isolation (GeV), columns - $\not\!\!E_T$ (GeV). An integer number is assigned to each combination of isolation and $\not\!\!E_T$ cut, and will be used to denote grid point for the Punzi cut optimization plot Fig. E.1. Although we used step size of 1 GeV for isolation and $\not\!\!E_T$ in the actual search, here we use a larger step size for the Table and Figure so they are readable.

Isolation	$\not\!\!E_T$ (GeV)				
(GeV)	10	15	20	25	30
2	1	2	3	4	5
4	6	7	8	9	10
6	11	12	13	14	15
8	16	17	18	19	20
10	21	22	23	24	25

In Fig. 8.7, we plot the optimization value $\mathbb{A}$, where $a = 95\%$. We found the following cuts maximize $\mathbb{A}$:

$$ISO < 4 \text{ GeV}, \ \not\!\!E_T > 15 \text{ GeV} \tag{8.2}$$

Fig. 8.8, 8.9 shows the isolation and $\not\!\!E_T$ distribution respectively, of the MUED signal Monte Carlo, the SM background, and data, before imposing the final optimization cuts, in the non-$\mu\mu\mu$ channels. Fig. 8.10 shows $\not\!\!E_T$ distribution of the MUED signal Monte Carlo, the SM background, and data after the isolation cut in the non-$\mu\mu\mu$ channels.

8.10 Summary of Events Selection Path, Expected Background and MUED Signal

Table 8.2 lists the number of events expected after each cut from each type of background, the sum of all background, the number of data events and a sample MUED MC point ($R^{-1} = 350$ GeV, $\Lambda R = 20$, the Higgs mass $m_h = 120$ GeV).

Table 8.2: Number of expected background events contributions from $b\bar{b}/c\bar{c}$, Drell-Yan, $t\bar{t}$ and boson pair, total number of expected background, data and MUED MC ($R^{-1} = 350$ GeV, $\Lambda R = 20$, the Higgs mass $m_h = 120$ GeV) events left after each cut. Both background and signal Monte Carlo are weighted by luminosity of 87.5 pb^{-1} , corrected with trigger efficiency, and scaled by the MC correction factor 0.86/event as described in Section 7.3.2. An overall scale factor of 2.1 is applied to $b\bar{b}/c\bar{c}$ background. The fake lepton rate 0.0081/event is applied to Drell-Yan background, thus the numbers in the table for Drell-Yan background is the fake lepton rate times the number of dilepton Drell-Yan events.

Cut	Events remaining after each cut						
	$b\bar{b}/c\bar{c}$	Drell-Yan	$t\bar{t}$	Boson Pair	Sum BG	Data	MUED MC
3 lepton requirement	577.58	33.53	2.03	0.40	613.54	1120	1.18
good run requirement	577.58	33.53	2.03	0.40	613.54	1068	1.18
cosmic removal	577.58	33.53	2.03	0.40	613.54	750	1.18
$\lvert z_{vertex}\rvert < 60$ cm	556.23	32.03	1.99	0.38	590.63	725	1.14
Vertex Requirements	555.70	32.03	1.99	0.38	590.10	683	1.14
$\lvert Q_1+Q_2+Q_3\rvert < 3$	539.47	32.03	1.91	0.36	573.77	604	1.14
Require e^+e^- or $\mu^+\mu^-$	454.08	30.72	1.52	0.34	486.66	545	1.10
Invariant Mass > 5 GeV/c^2	52.90	30.61	1.20	0.32	85.03	68	1.02
Z^0 removal (76-106 GeV/c^2)	52.42	7.70	1.04	0.07	61.23	55	1.02
Υ removal (9-11 GeV/c^2)	46.16	7.44	1.02	0.06	54.68	48	0.96
$\Delta\phi_{\ell_1\ell_2} < 170°$	38.14	4.87	0.96	0.05	44.02	43	0.90
Veto $\mu\mu\mu$ events	20.43	0.06	0.52	0.01	21.02	23	0.64
$ISO < 4$ GeV	0.44	0.04	0.04	0.00	0.52	3	0.42
$\not\!\!E_T > 15$ GeV	0.00	0.01	0.04	0.00	0.05	0	0.38

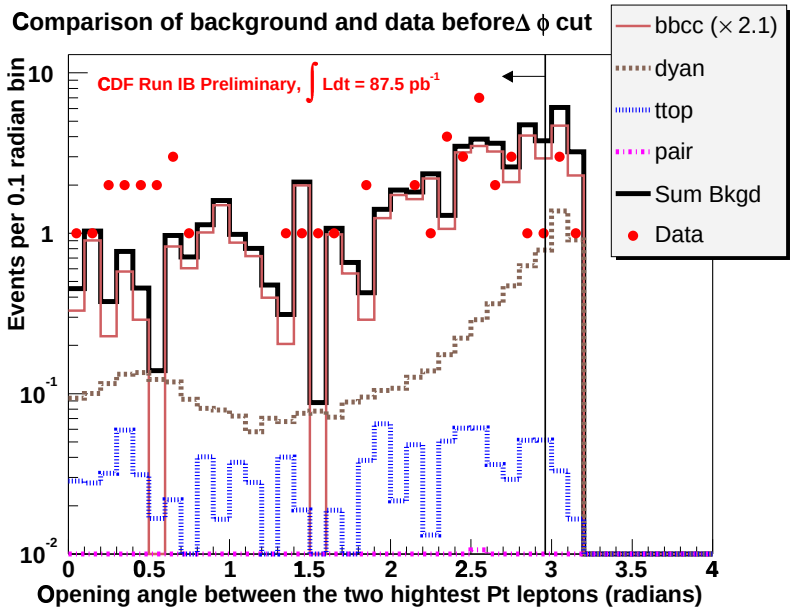

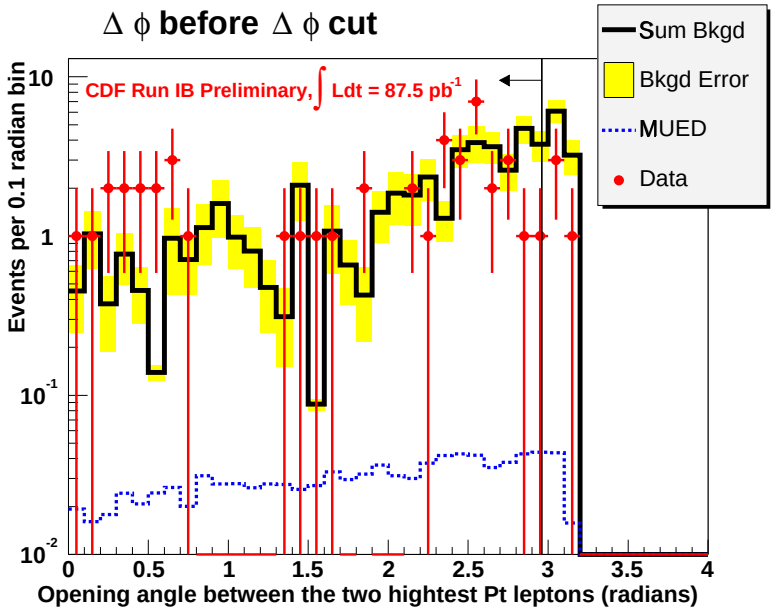

Figure 8.2: Distributions of opening angle of the two highest transverse momentum leptons. The top figure shows data and each type of background. The bottom figures shows the MUED signal, data and the total background with error band. The scale factor 2.1 is applied to $b\bar{b}/c\bar{c}$ background, and the total background includes $b\bar{b}/c\bar{c}$ background with scale factor 2.1 applied, Drell-Yan, $t\bar{t}$, and boson pairs. The vertical straight lines indicate the cut value and the arrows indicate the accepted values. Background MC samples are generated by the SUSY working group (Appendix B).

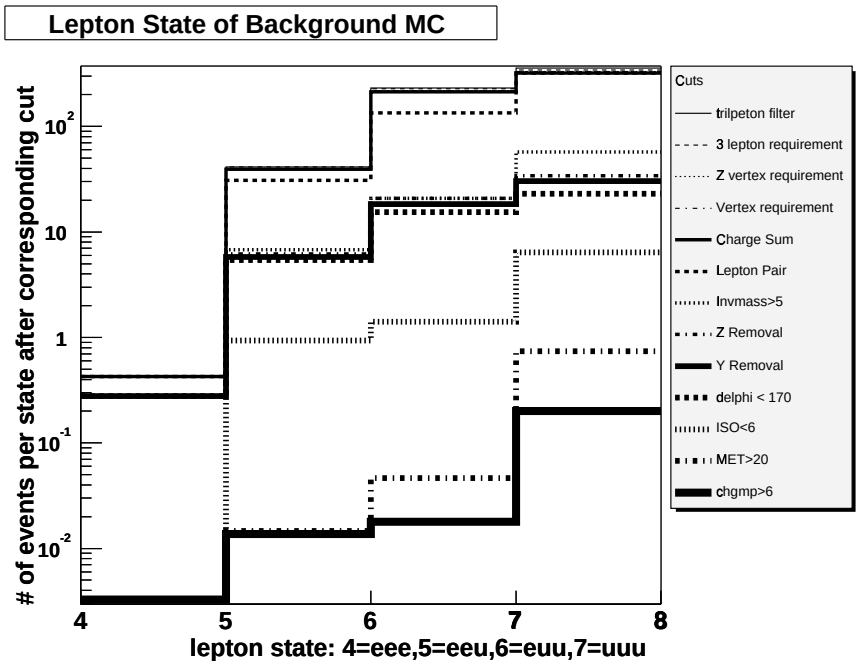

Figure 8.3: Lepton state distribution of reconstructed SM background MC

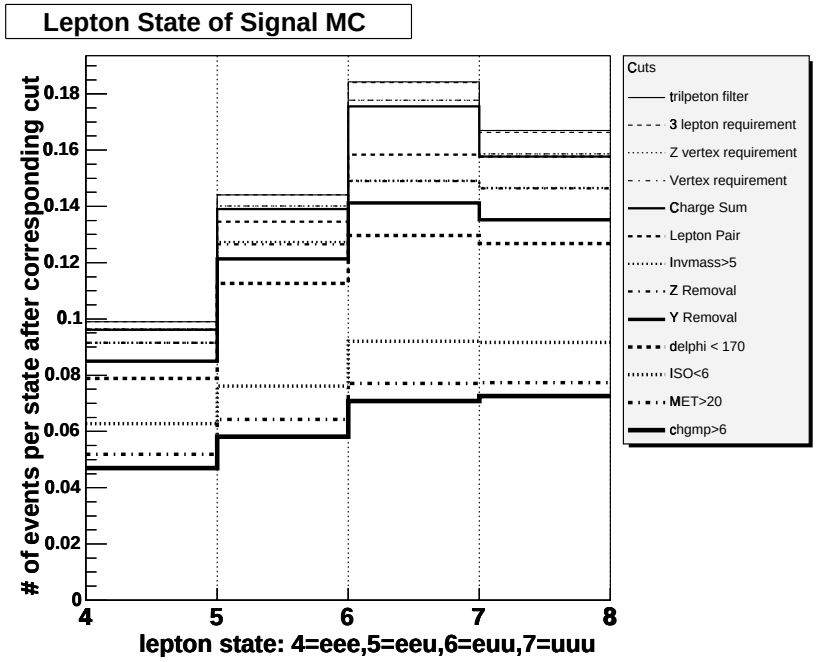

Figure 8.4: Lepton state distribution of reconstructed signal MC

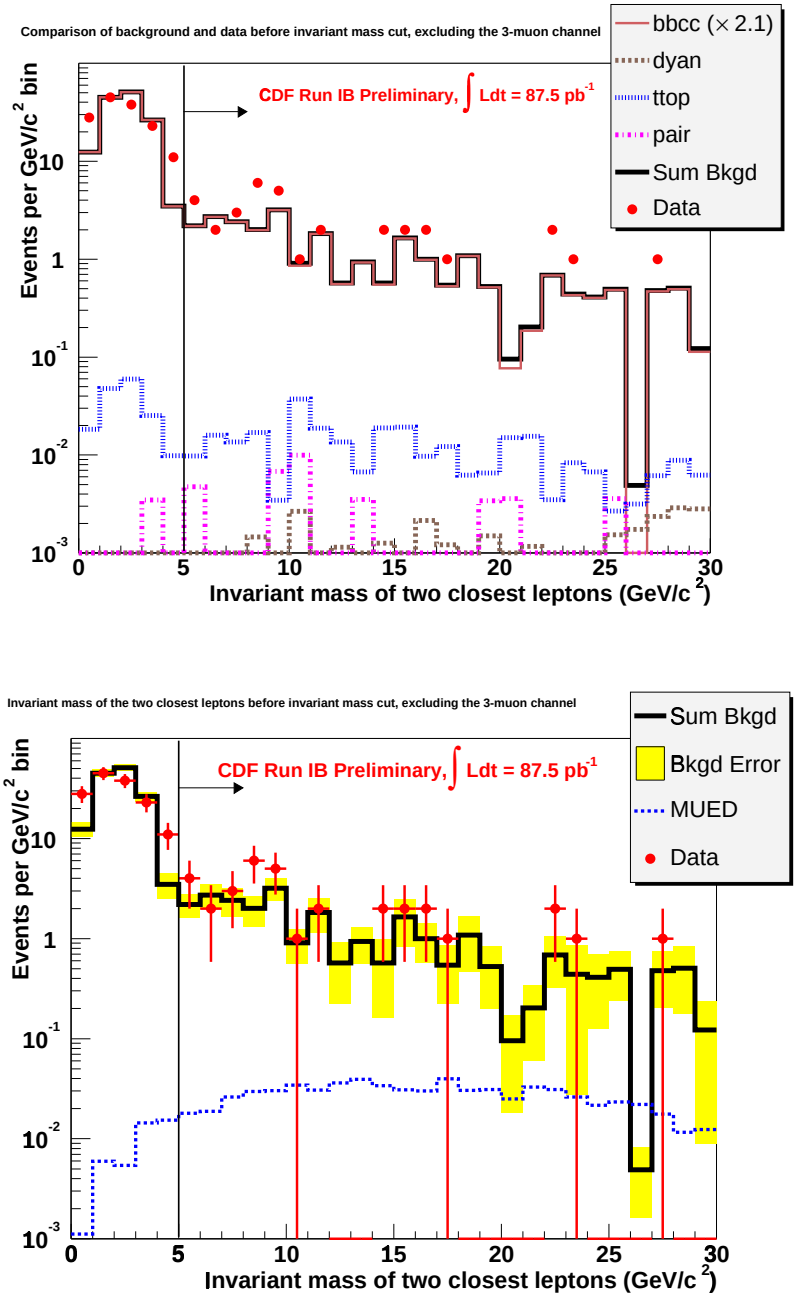

Figure 8.5: Distributions of invariant mass of the two closest leptons in the non-$\mu\mu\mu$ channels. The top figure shows data and each type of background. The bottom figures shows the MUED signal, data and the total background with error band. The scale factor 2.1 is applied to $b\bar{b}/c\bar{c}$ background, and the total background includes $b\bar{b}/c\bar{c}$ background with scale factor 2.1 applied, Drell-Yan, $t\bar{t}$, and boson pairs. The vertical straight lines indicate the cut value and the arrows indicate the accepted values. Background MC samples are generated by the SUSY working group (Appendix B).

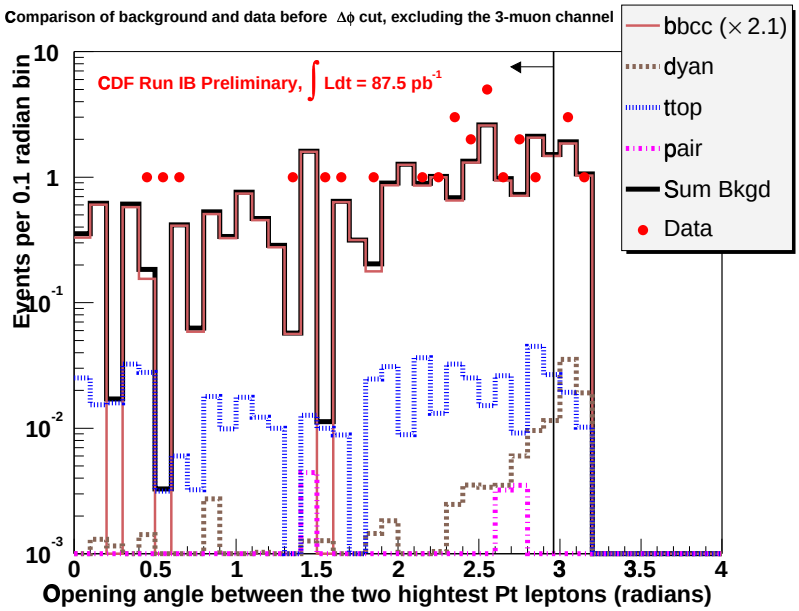

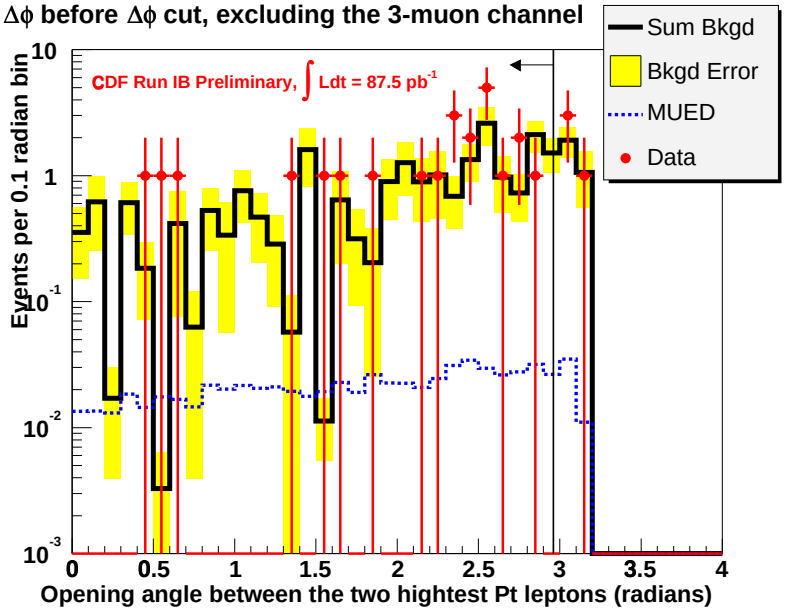

Figure 8.6: Distributions of opening angle of the two highest transverse momentum leptons in the non-$\mu\mu\mu$ channels. The top figure shows data and each type of background. The bottom figures shows the MUED signal, data and the total background with error band. The scale factor 2.1 is applied to $b\bar{b}/c\bar{c}$ background, and the total background includes $b\bar{b}/c\bar{c}$ background with scale factor 2.1 applied, Drell-Yan, $t\bar{t}$, and boson pairs. The vertical straight lines indicate the cut value and the arrows indicate the accepted values. Background MC samples are generated by the SUSY working group (Appendix B).

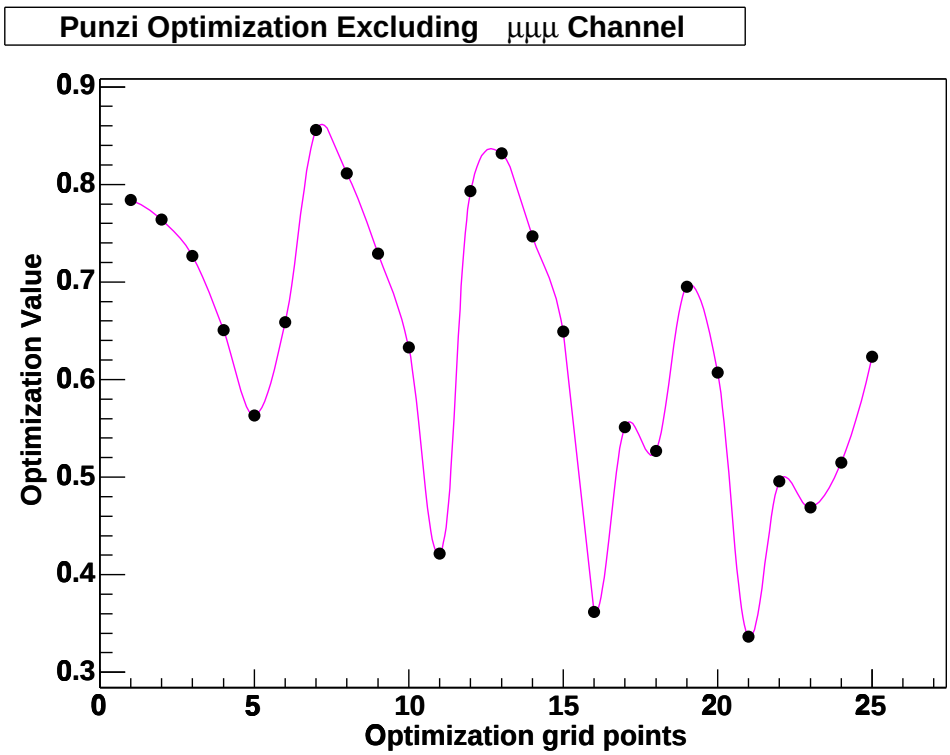

Figure 8.7: Punzi search in non-$\mu\mu\mu$ channel of the cut matrix to optimize value $\mathbb{A}$ (y axis), with $a = 95\%$. See Table. 8.1 for (x axis) grid points.

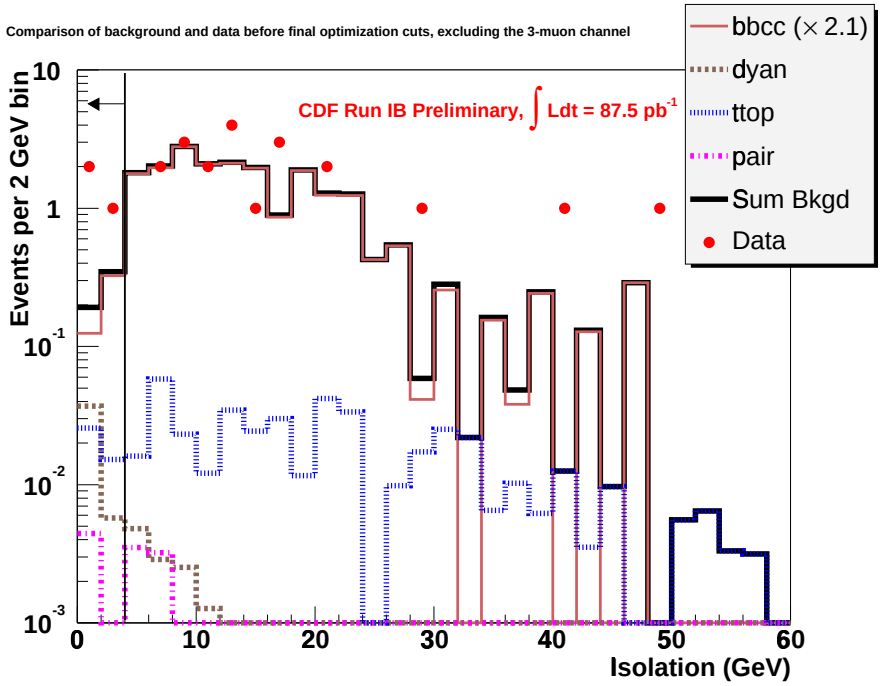

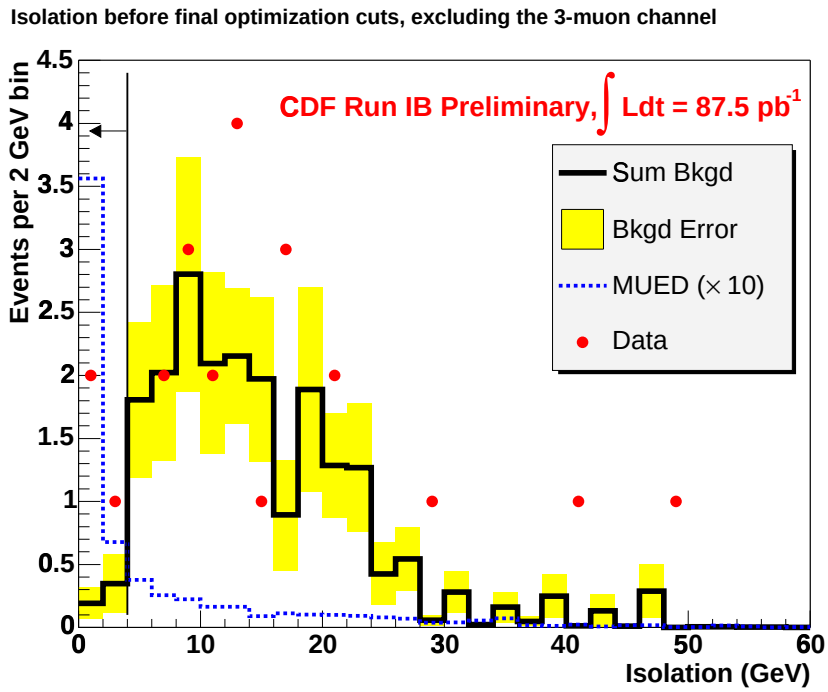

Figure 8.8: Distributions of isolation in the non-$\mu\mu\mu$ channels. The top figure shows data and each type of background. The bottom figures shows the MUED signal, data and the total background with error band. The scale factor 2.1 is applied to $b\bar{b}/c\bar{c}$ background, and the total background includes $b\bar{b}/c\bar{c}$ background with scale factor 2.1 applied, Drell-Yan, $t\bar{t}$, and boson pairs. The vertical straight lines indicate the cut value and the arrows indicate the accepted values. Background MC samples are generated by the SUSY working group (Appendix B).

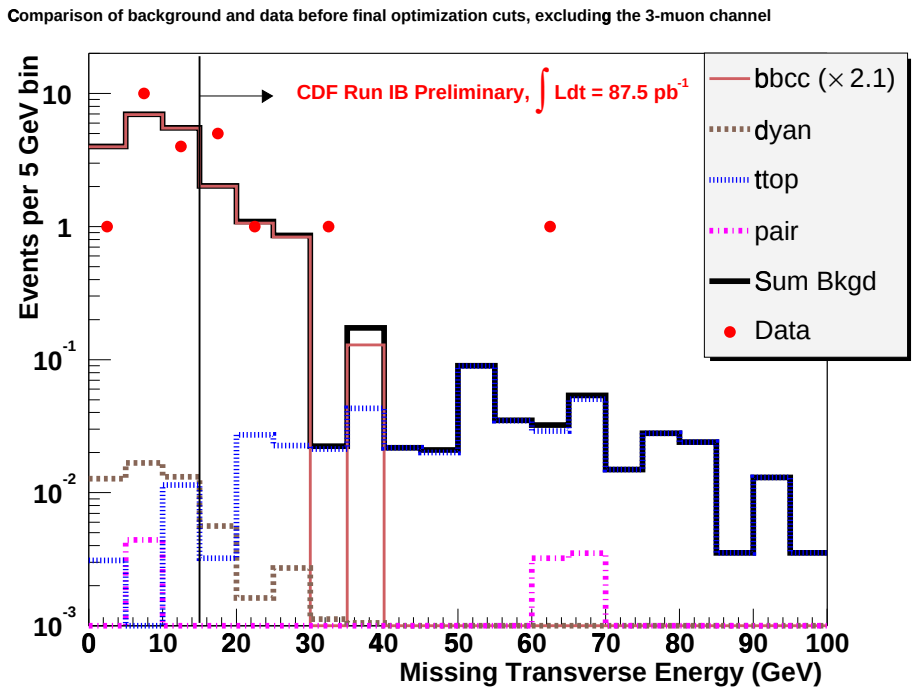

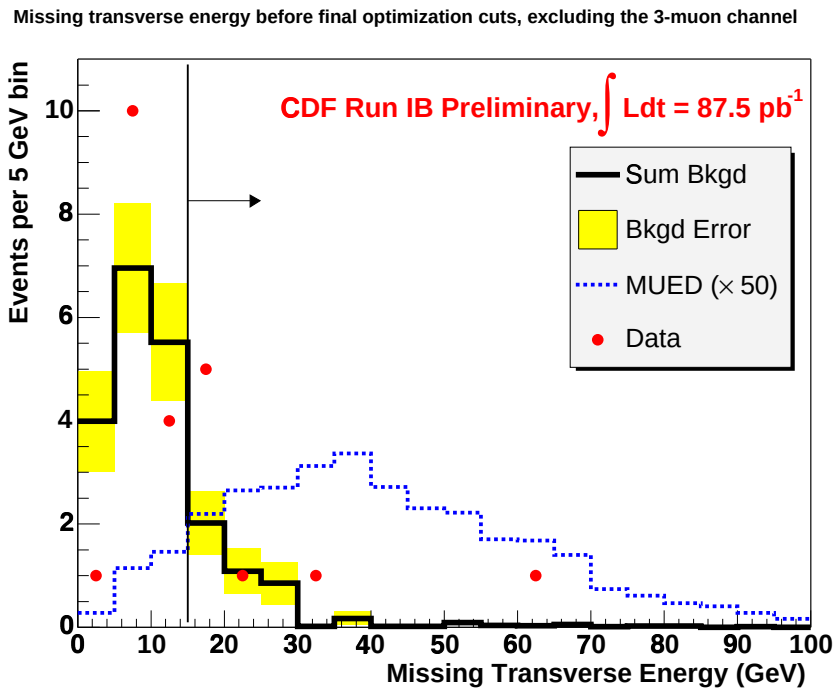

Figure 8.9: Distributions of missing transverse energy in the non-$\mu\mu\mu$ channels. The top figure shows data and each type of background. The bottom figures shows the MUED signal, data and the total background with error band. The scale factor 2.1 is applied to $b\bar{b}/c\bar{c}$ background, and the total background includes $b\bar{b}/c\bar{c}$ background with scale factor 2.1 applied, Drell-Yan, $t\bar{t}$, and boson pairs. The vertical straight lines indicate the cut value and the arrows indicate the accepted values. Background MC samples are generated by the SUSY working group (Appendix B).

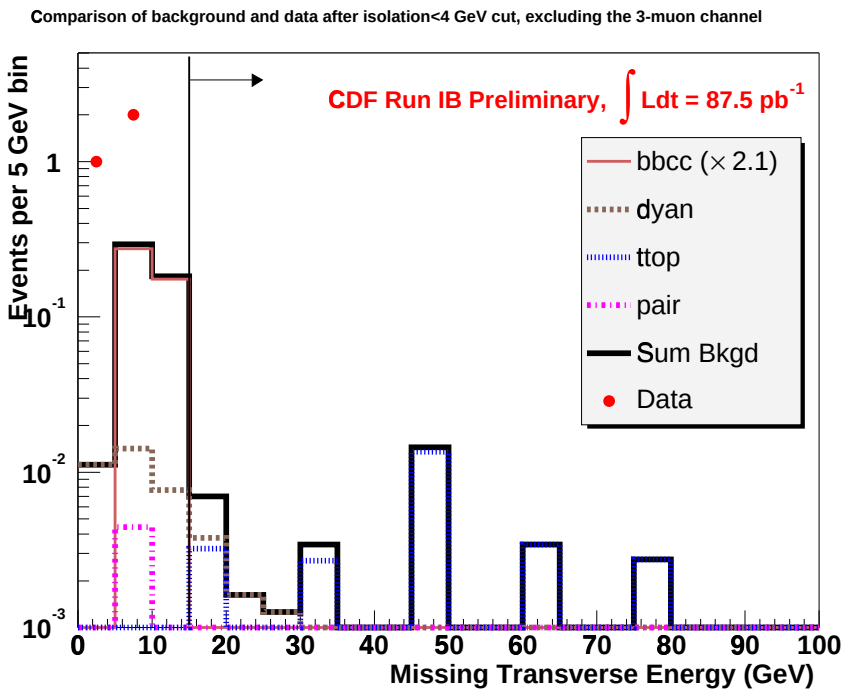

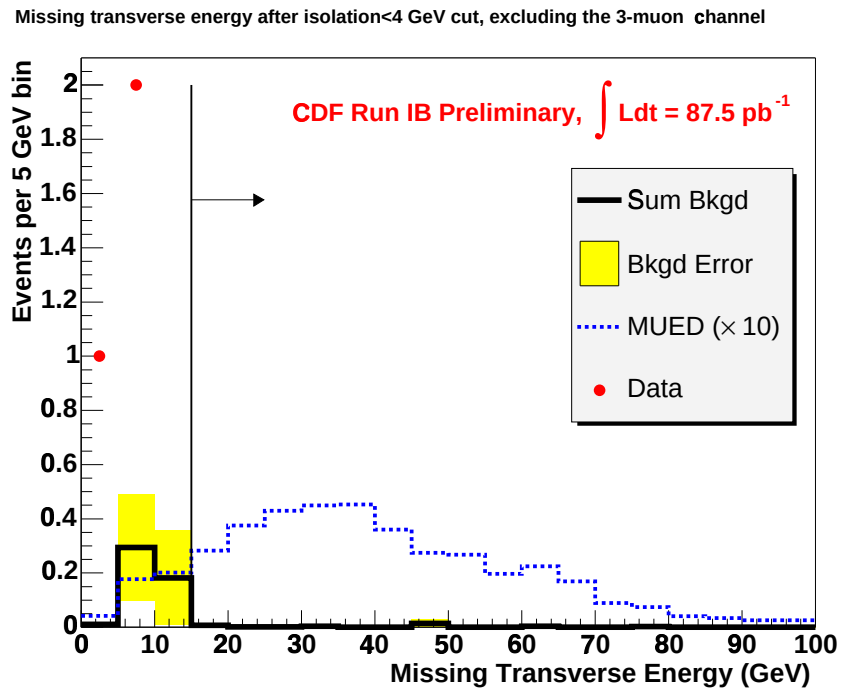

Figure 8.10: Distributions of missing transverse energy after isolation < 4 GeV cut in the non-$\mu\mu\mu$ channels. The top figure shows data and each type of background. The bottom figures shows the MUED signal, data and the total background with error band. The scale factor 2.1 is applied to $b\bar{b}/c\bar{c}$ background, and the total background includes $b\bar{b}/c\bar{c}$ background with scale factor 2.1 applied, Drell-Yan, $t\bar{t}$, and boson pairs. The vertical straight lines indicate the cut value and the arrows indicate the accepted values. Background MC samples are generated by the SUSY working group (Appendix B).

Chapter 9

Uncertainties

In this chapter we describe the uncertainties relevant to the analysis.

9.1 Systematic Uncertainty

The systematic uncertainty has several components:

- The Run IB integrated luminosity uncertainty. The uncertainty of the luminosity measurement mainly comes from Beam Beam Counter (BBC) normalization error, because cross sections at CDF are defined with respect to the BBC rate. The reported total uncertainty on the Run IB integrated luminosity is 4.1% [70]. This uncertainty affects both expected number of signal and background events.

- Trigger efficiency uncertainty. The uncertainty in the trigger efficiency has been studied in the previous trilepton analysis [46]: 5.6%. This uncertainty affects both expected number of signal and background events.

- Lepton identification efficiency uncertainty. Our analysis requires one tight lepton and two loose leptons. The highest uncertainty in lepton identification from

Table 7.2 comes from the tight lepton being a tight central electron (0.98%) and loose leptons being loose CMIO muons(1.54%). Thus overall uncertainty in lepton identification is 3.2% ($\sqrt{(0.98\%)^2 + (1.54\% + 1.54\%)^2}$). This uncertainty affects both expected number of signal and background events.

- Isolation cut efficiency uncertainty. QFL does not simulate lepton isolation correctly due to multiple interactions at high instantaneous luminosity. The highest uncertainty of isolation efficiency at the presence of 2 or more jets is from a muon of 0.904 ± 0.041, which gives us 4.5% uncertainty (see Section 7.3.3). We are picking out the maximum isolation from the three lepton candidates and cutting on that variable. If we can always pick out the correct maximum lepton isolation, then the systematic uncertainty would be 4.5% at most. If we pick the wrong lepton candidate, the isolation uncertainty can only be smaller. So taking 4.5% as the isolation cut efficiency uncertainty is the most conservative approach. This uncertainty affects both expected number of signal and background events.

- Uncertainty from the fake leptons. We used 0.81%±0.07% as the probability that a Drell-Yan dilepton event will have an additional fake lepton (see Section 6.2). The 0.07% error is the statistical error due to the number of leptons used to calculate the fake rate. The relative uncertainty is then 8.6%. In addition, a significant systematic error arises from the definition of a good $W^{\pm}$ event, lepton selection cuts and the use of MC programs, which cannot be easily obtained. We take the total uncertainty of fake leptons as 17.2% by doubling 8.6% as a conservative approach. This uncertainty affects the expected number of background events only.

9.2 Statistical Uncertainty

The number of expected MC events $n^{MCexpected}$ (non-integer) is

$$n^{MCexpected} = \sum_{i=1}^{n^{gen}} wgt_i \tag{9.1}$$

where the integer number n^{gen} is the number of events remaining after all cuts, and wgt_i is the weight of the corresponding event which includes the appropriate luminosity weighting [1] and various efficiency corrections (see Chapter 7.3).

Since events are statistically independent and each event has a weight, wgt_i, the absolute uncertainty of $n^{MCexpected}$ is obtained by summing up each event's weight in quadrature:

$$\Delta n^{MCexpected} = \sqrt{\sum_{i=1}^{n^{gen}} (wgt_i)^2} \tag{9.2}$$

After final cuts we have 0.54 signal events with absolute uncertainty of 0.014 event, and 0.80 background with absolute uncertainty of 0.018 event. Thus the relative statistical uncertainty of the signal is 2.6% and the relative statistical uncertainty of the background is 2.3%.

9.3 Theoretical Uncertainty

The theoretical uncertainty has two components:

- Uncertainty in the structure functions. For the MUED signal Monte Carlo we use the Pythia 6.203 default structure function CTEQ-5L. To study the uncertainty due to this choice, we generated samples with structure function

[1] We generated large integrated luminosity MC samples and we scale them to the integrated luminosity of the search data sample.

CTEQ-3L and GRV-94L for MC point $R^{-1} = 350$ GeV. After final cuts we have 0.54 signal events (luminosity scaled and MC weighted from a final sample size of 1527 events) from CTEQ-5L, 0.53 signal events (luminosity scaled and MC weighted from a final sample size of 1519 events) from CTEQ-3L, and 0.51 signal events (luminosity scaled and MC weighted from a final sample size of 1450 events) from GRV-94L. The average number of events is 0.53 events, and the largest difference between the average and the number from each structure function is 4%. Thus the uncertainty for the expected number of signal events from the structure functions is 4%. For background Monte Carlo generation CTEQ-3L, CTEQ-2L, MRSD0', and GRV-LO structure functions are used, and the uncertainty for the expected number of background events from the structure functions is 7%.

- Uncertainty from initial-state/final-state radiation. For the MUED signal Monte Carlo we enable initial-state and final-state radiation in Pythia generator by default. To study the uncertainty due to this choice, we generated samples with initial-state/final-state radiation turned off, and after final cuts we have 0.52 signal events (luminosity scaled and MC weighted from a final sample size of 1500 events). Comparing with 0.54 signal events (luminosity scaled and MC weighted from a final sample size of 1527 events) with initial-state and final-state radiation on, the average number of events is 0.53 ± 0.01. Thus the uncertainty due to the choice of initial-state/final-state radiation is 2%. This number is applied to MUED signal only.

Total Uncertainties The uncertainties combine in quadrature for a total signal relative uncertainty of 10.3% [2] and total background relative uncertainty of 20.7% [3].

[2] $\sqrt{0.041^2 + 0.056^2 + 0.032^2 + 0.045^2 + 0.026^2 + 0.04^2 + 0.02^2} = 10.3\%$

[3] $\sqrt{0.041^2 + 0.056^2 + 0.032^2 + 0.045^2 + 0.172^2 + 0.023^2 + 0.07^2} = 20.7\%$

Chapter 10

Limits on UED

In this section we describe the limit setting method and obtain the production cross section limit of the MUED scenario.

10.1 Limit Setting Method

The (integer) number of observed events n_0 from an experiment follows a Poisson distribution. If the mean number of events expected is μ (real), then the probability of observing n_0 events is given by

$$P(n_0; \mu) = \frac{\mu^{n_0} e^{-\mu}}{n_0!} \tag{10.1}$$

In new searches we want to determine a real number N for μ as an upper limit, such that we have probability p to observe n_0 or fewer events. The confidence level is $1 - p$ (the probability to observe more than n_0 events). p can be calculated as

$$p = \sum_{n=0}^{n_0} P(n; N) = \sum_{n=0}^{n_0} \frac{N^n e^{-N}}{n!} \tag{10.2}$$

If we know that μ_B expected background events are among the n_0 observed events, and the number of background events present in the sample is less than or equal to n_0, then we can obtain p as

$$p = \frac{\sum_{n=0}^{n_0} P(n; N + \mu_B)}{\sum_{n=0}^{n_0} P(n; \mu_B)} \tag{10.3}$$

If the expected number of background events, μ_B, has an uncertainty of σ_B and the expected number of signal events, μ_S, has an uncertainty of σ_S, we assume they both have Gaussian distributions: $G(\mu_B, \sigma_B) = \frac{1}{\sqrt{2\pi\sigma_B^2}} e^{-\frac{(x-\mu_B)^2}{2\sigma_B^2}}$, $G(\mu_S, \sigma_S) = \frac{1}{\sqrt{2\pi\sigma_S^2}} e^{-\frac{(x-\mu_S)^2}{2\sigma_S^2}}$. We want to determine a real number N for μ_S such that the probability p can be calculated as

$$p = \frac{\sum_{n=0}^{n_0} \frac{1}{\sqrt{2\pi\sigma_N^2}} \int_0^\infty \int_0^\infty P(n; \mu'_B + \mu'_S) e^{-\frac{(\mu_B - \mu'_B)^2}{2\sigma_B^2}} e^{-\frac{(N - \mu'_S)^2}{2\sigma_N^2}} d\mu'_B d\mu'_S}{\sum_{n=0}^{n_0} \int_0^\infty P(n; \mu_B) e^{-\frac{(\mu_B - \mu'_B)^2}{2\sigma_B^2}} d\mu'_B} \tag{10.4}$$

where $\sigma_N = N\sigma_A/A$ (σ_A is the uncertainty of signal acceptance and A is the signal acceptance), as the relative uncertainty on μ_S comes from the relative uncertainty of the signal acceptance.

The upper limit N can be obtained using either frequentist method or Bayesian method. For the frequentist algorithm we start from an arbitrary initial value N_i, and do toy experiments such that the expected number of signal and background follows a Gaussian distribution. We vary N_i until the desired p is reached, and count how many times signal + background $> n_0$ is recorded.

In this analysis, we obtain the upper limit N on a Poisson process using Bayesian

method, which treats the unknown expected mean number of signal events as a random variable with "prior" probability density function $\mathcal{P}(\mu_S)$. Given the observation of n_0 events, a "posterior" probability density function $\mathcal{P}(\mu_S; n_0, \mu_B)$ can be constructed from the likelihood $\mathcal{L}(n_0; \mu_S + \mu_B)$ for observing n_0 events given μ_S expected signal and μ_B expected background.

$$\mathcal{P}(\mu_S; n_0, \mu_B) = \frac{1}{2\pi\sigma_B\sigma_S}\int_0^\infty\int_0^\infty \mathcal{L}(n_0; \mu'_B+\mu'_S)e^{-\frac{(\mu_B-\mu'_B)^2}{2\sigma_B^2}}e^{-\frac{(\mu_S-\mu'_S)^2}{2\sigma_S^2}}d\mu'_B d\mu'_S \quad (10.5)$$

The upper limit N_{exp} on μ_S can be obtained from p as

$$p = \frac{\int_{N_{exp}}^\infty \mathcal{P}(\mu_S; n_0, \mu_B)d\mu_S}{\int_0^\infty \mathcal{P}(\mu_S; n_0, \mu_B)d\mu_S} \quad (10.6)$$

For a detailed discussion see [71], and we use program bayes.f in this reference for our calculation.

10.2 Cross Section Limit of KK Q_1Q_1 Pair Production

The total signal relative uncertainty is 10.3% and the total background relative uncertainty is 20.7%.

Having observed 0 events with 0.05 expected background events in the non-$\mu\mu\mu$ channels, we obtain $N_{exp} = 3.08$ (2.36) at Confidence Level of 95% (90%). [1]

We use the formula

[1] If we use charged multiplicity cut described in Appendix G, we would observe 0 events with 0.02 expected background events, thus $N_{exp} = 3.08$ (2.36) at Confidence Level of 95% (90%).

$$\sigma_{Q_1Q_1} \cdot \mathrm{BR}(Q_1Q_1 \to lll + X) \quad < \quad \frac{N_{exp}}{\epsilon^{tot} \cdot \int \mathcal{L}dt} \tag{10.7}$$

to set the upper limit for Q_1Q_1 production cross section times the branching ratio to trilepton [2] final states with the number of expected events divided by the detection efficiency times the integrated luminosity.

The detection efficiency is the combination of geometric acceptance, kinematic acceptance and trigger efficiency. At signal MC point ($R^{-1} = 350$ GeV, $\Lambda R = 20$, the Higgs mass $m_h = 120$ GeV) we started with 25,000 events. After the trilepton analysis selection (see Section 5.3) we have 3391 events, thus $\epsilon_1 = 13.6\%$. After final cuts (with trigger efficiency factor, lepton ID efficiency factor and isolation efficiency factor applied) we have 1247.0 events, thus $\epsilon_2 = 36.8\%$. The combined detection efficiency is thus $\epsilon^{tot} = 5.0\%$. There are 879.8 events in the non-$\mu\mu\mu$ channels after final cuts, corresponding to a total detection efficiency of 3.5%.

We generated $b_1\bar{b}_1$ pairs in our signal MC sample, and there are total of 5 flavors produced excluding the top quark. In order to compare with other quark flavors, we generated a signal MC sample of $u_1\bar{u}_1$ pairs at $R^{-1} = 350$ GeV and obtained $\epsilon^{tot} = 4.9\%$ (3.5% for the non-$\mu\mu\mu$ channels). The difference of total detection efficiency using different quark flavors is negligible. We take 3.5% for the non-$\mu\mu\mu$ channels as the detection efficiency.

From Table 4.1, we obtain $\mathrm{BR}(Q_1Q_1 \to lll + X) = \frac{5}{9} \times \frac{5}{9} = \frac{25}{81}$. For Run IB, $\int \mathcal{L}dt = 87.5$ pb^{-1}.

At signal MC point ($R^{-1} = 350$ GeV, $\Lambda R = 20$, the Higgs mass $m_h = 120$ GeV),

[2] Here we only consider electrons and muons

the Q_1Q_1 production cross section limit at Confidence Level of 95% (90%) is:

$$\sigma_{Q_1Q_1} \quad < 3.3 \text{ pb } (2.5 \text{ pb}) \; ; \tag{10.8}$$

The Q_1Q_1 production cross section is $\frac{1}{2}$ of the total KK quark production cross section (see Chapter 4), thus the KK quark (excluding KK top) production cross section limit at Confidence Level of 95% (90%) is 6.6 pb (5.0 pb). Converting this to an extra dimension radius limit according to Fig. 4.2 we have $R^{-1} >$ 270 GeV (280 GeV) (R $< 3.7 \times 10^{-19}$ m (3.5×10^{-19} m)).

10.3 Cross Section Limit of KK Quark Pair Production + KK Gluon-Quark Production + KK Gluon Pair Production

Till now we only considered KK quark pairs production since they have the largest cross section among all KK states (see Fig. 4.2). If we consider KK gluon-quark production and KK gluon pair production, equation (10.7) would become:

$$\begin{aligned} N_{exp} > (\epsilon_{Q_1Q_1} \cdot \sigma_{\text{KK quark pair}} \cdot \text{BR}(\text{KK quark pair} \rightarrow lll + X) + \\ \epsilon_{g_1Q_1} \cdot \sigma_{\text{KK gluon}-\text{quark}} \cdot \text{BR}(\text{KK gluon} - \text{quark} \rightarrow lll + X) + \\ \epsilon_{g_1g_1} \cdot \sigma_{\text{KK quark pair}} \cdot \text{BR}(\text{KK quark pair} \rightarrow lll + X)) \\ \cdot \int \mathcal{L} dt \end{aligned}$$

We generated KK gluon-quark sample and KK gluon pair sample at 350 GeV.

Using the same cuts as we did for KK quark pairs, we obtained the total detection efficiency for the KK gluon-quark and KK gluon pair samples listed in Table 10.1.

Table 10.1: Total detection efficiency in the non-$\mu\mu\mu$ Channels.

Sample	Total Detection Efficiency in the non-$\mu\mu\mu$ Channels
Q_1Q_1	3.5%
g_1Q_1	2.1%
g_1g_1	2.0%

What we care about is how many SU(2)-doublet KK quarks are produced:

- 1/2 of the $n = 1$ mode KK quark pairs are Q_1Q_1 (if we ignore the small mass splitting between doublets and singlets).
- 1/2 of the $n = 1$ mode KK gluon-quark produced are g_1Q_1, and 1/2 of the KK g_1 decay to Q_1Q_0, so overall 1/4 of the KK gluon-quark contribute three or four leptons.
- 1/4 of the $n = 1$ mode KK gluon pairs would decay to $Q_1Q_0Q_1Q_0$

At 350 GeV, the production cross section for KK quark pairs, gluon-quark, gluon pairs are 0.7 pb, 0.15 pb, and 0.08 pb respectively(see Fig. 4.2) [3], thus $\sigma_{\text{KK gluon-quark}} = 0.21\sigma_{\text{KK quark pair}}$, $\sigma_{\text{KK gluon pair}} = 0.11\sigma_{\text{KK quark pair}}$.

For the non-$\mu\mu\mu$ channels we have:

$$\begin{aligned} N_{exp} = (0.035 \times \sigma_{\text{KK quark pair}} \times \frac{1}{2} \times \text{BR}(Q_1Q_1 \to lll + X) + \\ 0.021 \times 0.21 \times \sigma_{\text{KK quark pair}} \times \frac{1}{4} \times \text{BR}(Q_1Q_1 \to lll + X) + \\ 0.020 \times 0.11 \times \sigma_{\text{KK quark pair}} \times \frac{1}{4} \times \text{BR}(Q_1Q_1 \to lll + X)) \\ \cdot \int \mathcal{L} dt \end{aligned}$$

[3]The production cross section relevant for the trilepton signal is 1/2 * 0.7 + 1/4 * 0.15 + 1/4 * 0.08 = 0.4075 pb.

We obtain $\sigma_{\text{KK quark pair}} < 6.0$ pb (4.6 pb) at Confidence Level of 95% (90%)

Ignoring KK top production,

$\sigma_{KK} = \sigma_{\text{KK quark pair}} + \sigma_{\text{KK gluon}-\text{quark}} + \sigma_{\text{KK gluon pair}} < 7.9$ pb (6.0 pb)

Converting this to an extra dimension radius limit according to Fig. 4.2 we have $R^{-1} >$ 280 GeV (290 GeV) (R $< 3.5 \times 10^{-19}$ m (3.4×10^{-19} m)).

Chapter 11

Conclusion

We have searched for evidence of Universal Extra Dimensions from $p\bar{p}$ collisions at $\sqrt{s}$=1.8 TeV using the CDF detector and the Fermilab Tevatron. In the Minimal Universal Extra Dimensions scenario, Kaluza-Klein excitations of standard particles would be pair produced at the Tevatron and would undergo cascade decays into their zero mode counterparts and the LKP γ_1. The LKP is stable and will escape the detector resulting in a missing energy signature. In this thesis we search for $n = 1$ mode pair production of KK quarks and gluons, the production modes which have the largest production cross section among all KK states at the Tevatron. The signature of the cascade decay of a SU(2)-doublet KK quark in the detector would be three or four standard leptons, two quark jets and missing energy. The Standard Model background similar to the MUED signature is dominated by $b\bar{b}/c\bar{c}$ production and Drell-Yan events, while other backgrounds from $t\bar{t}$, WW, WZ, and ZZ are negligible. Both background and MUED signal Monte Carlo samples are generated and passed through detector simulation, and the event selection criteria are chosen according to the kinematic distribution of decay products determined from Monte Carlo studies, optimized to reject background with a minimal loss of signal acceptance. We searched

for three charged leptons and missing transverse energy in an integrated luminosity of 87.5 pb^{-1} data collected during CDF Run IB period, and find no evidence for $n = 1$ mode direct KK pair production. We set an upper limit of total KK production cross section $\sigma_{KK} < 7.9$ pb at 95% confidence level, corresponding to a minimum extra dimension energy scale of 280 GeV (maximum radius of 3.5×10^{-19} m).

More data have been collected in CDF Run II ($\sqrt{s}$=1.96 TeV), and an analysis in Run II can be done using the same analysis technique once the SM background samples are in place. Assuming the Run II limit on $n = 1$ direct KK pair production cross section depends primarily on statistics, we can expect an improvement of around a factor of 10 in the cross section limit [32], corresponding to a minimum extra dimension energy scale of 400 GeV (maximum radius of 2.5×10^{-19} m). The LHC provides much better prospects for the discovery of KK production, where both the KK production cross sections at the LHC energy and the expected luminosity are higher than the Tevatron. The discovery reach of KK production in the LHC is expected to correspond to a minimum extra dimension energy scale around 2 TeV (maximum radius of 5×10^{-20} m). Either KK production of the UED scenario will be discovered at the Tevatron Run II or the LHC, or the lower bound on the energy scale of the extra dimension (1/R) will be raised greatly.

Appendix A

MUED Radiative Corrections to Kaluza-Klein Masses

The radiative corrections to the KK mass spectrum were calculated by Cheng, Matchev and Schmaltz [35] using the one-loop leading log approximation. The corrections to the masses of the KK modes contains both bulk terms and boundary terms.

The bulk corrections are:

$$
\begin{aligned}
\delta\left(m_{B_n}^2\right) &= -\frac{39}{2}\,\frac{g'^2\,\zeta(3)}{16\pi^4}\left(\frac{1}{R}\right)^2, \\
\delta\left(m_{W_n}^2\right) &= -\frac{5}{2}\,\frac{g_2^2\,\zeta(3)}{16\pi^4}\left(\frac{1}{R}\right)^2, \\
\delta\left(m_{g_n}^2\right) &= -\frac{3}{2}\,\frac{g_3^2\,\zeta(3)}{16\pi^4}\left(\frac{1}{R}\right)^2, \\
\delta(m_{f_n}) &= 0, \\
\delta(m_{H_n}^2) &= 0
\end{aligned}
\tag{A.1}
$$

The boundary corrections are:

$$
\begin{aligned}
\bar{\delta}\,(m^2_{B_n}) &= m_n^2 \left(-\frac{1}{6}\right) \frac{g'^2}{16\pi^2} \ln \frac{\Lambda^2}{\mu^2}, \\
\bar{\delta}\,(m^2_{W_n}) &= m_n^2 \, \frac{15}{2} \, \frac{g_2^2}{16\pi^2} \ln \frac{\Lambda^2}{\mu^2}, \\
\bar{\delta}\,(m^2_{g_n}) &= m_n^2 \, \frac{23}{2} \, \frac{g_3^2}{16\pi^2} \ln \frac{\Lambda^2}{\mu^2}, \\
\bar{\delta}\, m_{Q_n} &= m_n \left(3 \, \frac{g_3^2}{16\pi^2} + \frac{27}{16} \, \frac{g_2^2}{16\pi^2} + \frac{1}{16} \, \frac{g'^2}{16\pi^2}\right) \ln \frac{\Lambda^2}{\mu^2}, \\
\bar{\delta}\, m_{L_n} &= m_n \left(\frac{27}{16} \, \frac{g_2^2}{16\pi^2} + \frac{9}{16} \, \frac{g'^2}{16\pi^2}\right) \ln \frac{\Lambda^2}{\mu^2} \; . \qquad \text{(A.2)}
\end{aligned}
$$

Here B_n are the KK U(1) hypercharge gauge bosons, W_n are the KK $\mathrm{SU(2)_W}$ gauge bosons, g_n are the KK gluons, Q_n are the KK SU(2)-doublet quarks, and L_n are the KK SU(2)-doublet leptons. The renormalization scale μ should be taken to be approximately the mass of the corresponding KK mode. g_3, g_2, g' are $\mathrm{SU(3)_C}$, $\mathrm{SU(2)_L}$, and $\mathrm{U(1)_Y}$ couplings respectively, and $\alpha_s = g_3^2/4\pi$, $\alpha_{EM} = e^2/4\pi$, $e = g_2 \sin\theta_{\mathrm{W}}$, $\sin^2\theta_{\mathrm{W}} = (\mathrm{g}')^2/(\mathrm{g}_2^2 + (\mathrm{g}')^2)$.

Appendix B

Run IB Standard Model Background Monte Carlo

The CDF SUSY working group has generated a large background Monte Carlo samples for Run IB analysis with ISAJET version 7_06 and 7_20. Files with two digit run-numbers are generated with version 7_06 using parton distribution function [1] CTEQ-2L, MRSD0', and GRV-LO, and files with three digit run-numbers are generated with version 7_20 using parton distribution function CTEQ-3L and GRV-94LO.

Some of the samples have a selection applied on generator level. For the $b\bar{b}$, $c\bar{c}$ samples at least one b or c quark with $\mathrm{p_T} > 10$ GeV/c in $|y| < 4.0$ [2] was required. The $b\bar{b}$, $c\bar{c}$, and Drell-Yan samples are required to have at least one high-$\mathrm{p_T}$ lepton ($\mathrm{p_T} > 9.0$ GeV/c and $|\eta| < 1.5$) or two low-pT leptons ($\mathrm{p_T} > 2.8$ GeV/c and $|\eta| < 3.0$). (Lepton stands for electron or muon.)

The production of $b\bar{b}/c\bar{c}$ MC sample was split up into 3 generation processes:

[1] Parton Distribution Functions, PDFs, are used to calculate the cross section of processes which have hadrons (such as protons) in the initial state. The PDFs give the probability density distribution of quarks and gluons as a function of the fraction of the proton's momentum it carries.

[2] y denotes rapidity. The definition is $y \equiv \frac{1}{2}\ln(\frac{E+p_z}{E-p_z})$, where E is the energy of the particle and p_z is its momentum along the z axis.

direct three lepton production, initial state gluon radiation (ISR) and final state gluon radiation (FSR). Each of these processes was again split up in three areas according to the exchanged momentum with p_T ranging from 10 to 500 GeV/c. The nine data sets were each generated as a separate run. For each of the runs the event generation was performed with at least three different parton distribution functions.

The production of Drell-Yan was split up into 3 processes according to the exchanged particle: γ events with p_T ranging from 5 to 500 GeV/c; Drell-Yan Z^0 events with p_T ranging from 0.1 to 5 GeV/c and 5 to 500 GeV/c.

The production of $t\bar{t}$ events was generated with a p_T range of 0.1 to 500 GeV/c.

The production of Diboson W^+W^-, Z^0Z^0 and $W^\pm Z^0$ events was generated with a p_T range of 0.1 to 500 GeV/c.

Table B.1, B.2, B.3, B.4 list the background sample used in this analysis and give details on the event generation. A few of the original files were on physically damaged tapes thus were excluded, with the corresponding total luminosity adjusted.

Table B.1: SM $b\bar{b}/c\bar{c}$ background M.C. used in our analysis

Run Number	Type of Production	q range [GeV]	Structure Function	file sequence	lumi [pb^{-1}]	production tape
81	direct	[10, 25]	CTEQ2L	ka-kt	62.7	RK7442
			MRSD0'	la-lt	53.3	RK7625
			GRV_LO	ma-mt	59.1	RK7626
82	direct	[25, 50]	CTEQ2L	ka-kt	88.1	RK7628
						RK7872
			MRSD0'	la-lt	76.0	RK7865
						RK7872
			GRV_LO	ma-mt	98.3	RK7867
						RK7872
082			CTEQ3L	qa-qt	85.9	RK8364
						RK8367
			GRV_94	ra-rt	94.4	RK8463
						RK8465
83	direct	[50,500]	CTEQ2L	kp-kt	133.4	RK7874
			MRSD0'	la-lj	248.9	RK7872
			GRV_LO	ma-mj	336.7	RK7874
083			CTEQ3L	qa-qj	282.1	RK8367
						RK8369
84	ISR	[10, 25]	CTEQ2L	ka-kt	133.5	RK7634
			MRSD0'	la-lj	94.9	RK7934
			GRV_LO	ma-mj	58.2	RK7934
85	ISR	[25, 50]	CTEQ2L	ka-kt	132.9	RK7936
						RK7937
			MRSD0'	la-lt	157.3	RK7937
						RK7938
			GRV_LO	ma-mt	145.4	RK7938
						RK7939
085			CTEQ3L	qa-qt	145.6	RK8363
						RK8364
86	ISR	[50,500]	CTEQ2L	ka-kj	304.9	RK7940
			MRSD0'	la-lj	382.5	RK7940
						RK8003
			GRV_LO	ma-mj	387.9	RK8003
						RK8005
086			CTEQ3L	qj-qt	427.5	RK8370
87	FSR	[15, 25]	CTEQ2L	ka-ke	104.2	RK8005
			MRSD0'	la-le	92.5	RK8005
			GRV_LO	ma-md	89.8	RK8005
88	FSR	[25, 50]	CTEQ2L	ka-kt	60.5	RK8008
						RK8010
			MRSD0'	la-lt	54.4	RK8010
						RK8086
			GRV_LO	ma-mt	70.8	RK8086
						RK8087
088			CTEQ3L	qa-qt	167.4	RK8370
						RK8371
			GRV_94	ra-rt	192.8	RK8465
						RK8467
89	FSR	[50,500]	CTEQ2L	ka-kt	110.2	RK8087
						RK8089
						RK8090
			MRSD0'	la-lt	105.9	RK8090
						RK8094
			GRV_LO	ma-mt	142.0	RK8094
						RK8095
			CTEQ2L	na-nt	109.4	RK8266
						RK8267
			MRSD0'	oa-ot	105.5	RK8267
						RK8269
			GRV_LO	pa-pt	141.7	RK8273
						RK8363
089			CTEQ3L	qa-qt	321.3	RK8372
						RK8462
			GRV_94	ra-rt	389.9	RK8467
						RK8471

Table B.2: SM Drell-Yan background M.C. used in our analysis

Run Number	**Exchanged Particle**	**q range [GeV]**	**Structure Function**	**file sequence**	**lumi** [pb^{-1}]	**production tape**
92	gamma	m=[5,500] t=[5,500]	CTEQ2L	ka-kt	483.7	RK7629
			MRSD0'	la-lt	431.8	RK7866
			GRV_LO	ma-mt	501.7	RK7868
092			CTEQ3L	qa-qj	241.3	RK8471
						RK8549
			GRV_94	ra-rj	254.8	RKB836
93	Z	m=[5,500] t=[5,500]	CTEQ2L	ka-kt	424.8	RK7869
			MRSD0'	la-lt	403.7	RK7871
			GRV_LO	ma-mt	446.3	RK7873
94	Z	m=[5,500] t=[0.1,5]	CTEQ2L	ka-kj	195.5	RKB840
			MRSD0'	la-lj	176.0	RKB841
			GRV_LO	ma-mj	217.3	RK7932

Table B.3: SM $t\bar{t}$ background M.C. used in our analysis

Run Number	**q range [GeV]**	**Structure Function**	**file sequence**	**lumi** [pb^{-1}]	**production tape**
90	[0.1,500] m=175	CTEQ2L	ka-ke	5316.0	RK7627
		MRSD0'	la-le	5538.0	RK7627
		GRV_LO	ma-me	5558.0	RK7939
090		CTEQ3L	qa-qe	5430.0	RK8462
91	[0.1,500] m=175 noGLr	CTEQ3L	qa-qe	5466.0	RK9820

Table B.4: SM boson pair background M.C. used in our analysis

Run Number	**Diboson Particle**	**q range [GeV]**	**Structure Function**	**file sequence**	**lumi** [pb^{-1}]	**production tape**
95	WW	[0.1,500]	CTEQ2L	ka-kc	2343.0	RKB843
			MRSD0'	la-lc	2154.0	RK7932
			GRV_LO	ma-mc	2373.0	RK7932
96	WZ	[0.1,500]	CTEQ2L	ka	5819.0	RK7932
			MRSD0'	la	5169.0	RK7932
			GRV_LO	ma	5696.0	RK7932
97	ZZ	[0.1,500]	CTEQ2L	ka	6843.0	RK7627
			MRSD0'	la	6590.0	RK8005
			GRV_LO	ma	7149.0	RK8269

Appendix C

MUED Signal Monte Carlo Pythia TCL File

```
# Set the process name for objects we create
creator set XDIM
set useRCP t
# input module for generators
mod input GenInputManager
# enable generator
mod enable Pythia

talk Pythia
PythiaMenu
cmEnergy set 1800
msel set 0
commonMenu
```

```
set_ckin -index=1 -value=900.
set_ckin -index=9 -value=-2
set_ckin -index=10 -value=2
set_ckin -index=11 -value=-2
set_ckin -index=12 -value=2

# Decays of a b_1 quark
# b_1→ b + Z_1, c + W_1^-
# Z_1→ μ^∓ + μ_1^±, e^∓ + e_1^±
# W_1^+→ μ^+ + ν_μ1, e^+ + ν_e1, μ_1^+ + ν_μ, e_1^+ + ν_e
# μ_1→ μ + γ_1, ν_μ1→ ν_μ + γ_1
# e_1→ e + γ_1, ν_e1→ ν_e + γ_1

# Particle code
# 7 = b_1, 32 = Z_1, 34 = W_1, 4000011 = e_1/μ_1, 4000012 = ν_μ1/ν_e1, 16 = γ_1
# 5 = b, 4 = c, 13 = μ, 11 = e, 14 = ν_μ, 12 = ν_e

# Set mass of resonance
set_pmas -masscode=7 -mass=417.7 -width=2. -maxdev=20.
set_pmas -masscode=32 -mass=379.2 -width=2. -maxdev=20.
set_pmas -masscode=34 -mass=379.1 -width=2. -maxdev=20.
set_pmas -masscode=4000011 -mass=359.7 -width=2. -maxdev=20.
set_pmas -masscode=4000012 -mass=359.7 -width=2. -maxdev=20.
set_pmas -masscode=16 -mass=350.3

# decay of particle b_1
```

```
set_kfdp -channelIndex=65 -products=32,5
set_brat -channelIndex=65 -brRatio=0.2
set_mdme -channelIndex=65 -decayType=1 -matrix=0
set_kfdp -channelIndex=64 -products=-34,4
set_brat -channelIndex=64 -brRatio=0.8
set_mdme -channelIndex=64 -decayType=1 -matrix=0

# Set all other b_1 decays to unphysical (decayType=-1) or close (decayType=0)
set_mdme -channelIndex=56 -decayType=-1
set_mdme -channelIndex=57 -decayType=-1
set_mdme -channelIndex=58 -decayType=-1
set_mdme -channelIndex=59 -decayType=-1
set_mdme -channelIndex=60 -decayType=-1
set_mdme -channelIndex=61 -decayType=-1
set_mdme -channelIndex=62 -decayType=-1
set_mdme -channelIndex=63 -decayType=-1

# decay of particle Z_1
set_kfdp -channelIndex=301 -products=13,-4000011
set_brat -channelIndex=301 -brRatio=0.25
set_mdme -channelIndex=301 -decayType=1 -matrix=0
set_kfdp -channelIndex=299 -products=-13,4000011
set_brat -channelIndex=299 -brRatio=0.25
set_mdme -channelIndex=299 -decayType=1 -matrix=0
set_kfdp -channelIndex=297 -products=11,-4000011
set_brat -channelIndex=297 -brRatio=0.25
```

```
set_mdme -channelIndex=297 -decayType=1 -matrix=0
set_kfdp -channelIndex=303 -products=-11,4000011
set_brat -channelIndex=303 -brRatio=0.25
set_mdme -channelIndex=303 -decayType=1 -matrix=0

# Set all other Z_1 decays to unphysical
set_mdme -channelIndex=289 -decayType=-1
set_mdme -channelIndex=290 -decayType=-1
set_mdme -channelIndex=291 -decayType=-1
set_mdme -channelIndex=292 -decayType=-1
set_mdme -channelIndex=293 -decayType=-1
set_mdme -channelIndex=294 -decayType=-1
set_mdme -channelIndex=295 -decayType=-1
set_mdme -channelIndex=296 -decayType=-1
set_mdme -channelIndex=298 -decayType=-1
set_mdme -channelIndex=300 -decayType=-1
set_mdme -channelIndex=302 -decayType=-1
set_mdme -channelIndex=304 -decayType=-1
set_mdme -channelIndex=305 -decayType=-1
set_mdme -channelIndex=306 -decayType=-1
set_mdme -channelIndex=307 -decayType=-1
set_mdme -channelIndex=308 -decayType=-1
set_mdme -channelIndex=309 -decayType=-1
set_mdme -channelIndex=310 -decayType=-1

# decay of particle W_1^+
```

```
set_kfdp -channelIndex=330 -products=-13,-4000012
set_brat -channelIndex=330 -brRatio=0.25
set_mdme -channelIndex=330 -decayType=1 -matrix=0
set_kfdp -channelIndex=329 -products=-11,-4000012
set_brat -channelIndex=329 -brRatio=0.25
set_mdme -channelIndex=329 -decayType=1 -matrix=0
set_kfdp -channelIndex=328 -products=-4000011,-14
set_brat -channelIndex=328 -brRatio=0.25
set_mdme -channelIndex=328 -decayType=1 -matrix=0
set_kfdp -channelIndex=327 -products=-4000011,-12
set_brat -channelIndex=327 -brRatio=0.25
set_mdme -channelIndex=327 -decayType=1 -matrix=0

# Set all other W_1^+ decays to unphysical
set_mdme -channelIndex=311 -decayType=-1
set_mdme -channelIndex=312 -decayType=-1
set_mdme -channelIndex=313 -decayType=-1
set_mdme -channelIndex=314 -decayType=-1
set_mdme -channelIndex=315 -decayType=-1
set_mdme -channelIndex=316 -decayType=-1
set_mdme -channelIndex=317 -decayType=-1
set_mdme -channelIndex=318 -decayType=-1
set_mdme -channelIndex=319 -decayType=-1
set_mdme -channelIndex=320 -decayType=-1
set_mdme -channelIndex=321 -decayType=-1
set_mdme -channelIndex=322 -decayType=-1
```

```
set_mdme -channelIndex=323 -decayType=-1
set_mdme -channelIndex=324 -decayType=-1
set_mdme -channelIndex=325 -decayType=-1
set_mdme -channelIndex=326 -decayType=-1
set_mdme -channelIndex=331 -decayType=-1
set_mdme -channelIndex=332 -decayType=-1
set_mdme -channelIndex=333 -decayType=-1
set_brat -channelIndex=311 -brRatio=0
set_brat -channelIndex=312 -brRatio=0
set_brat -channelIndex=313 -brRatio=0
set_brat -channelIndex=314 -brRatio=0
set_brat -channelIndex=315 -brRatio=0
set_brat -channelIndex=316 -brRatio=0
set_brat -channelIndex=317 -brRatio=0
set_brat -channelIndex=318 -brRatio=0
set_brat -channelIndex=319 -brRatio=0
set_brat -channelIndex=320 -brRatio=0
set_brat -channelIndex=321 -brRatio=0
set_brat -channelIndex=322 -brRatio=0
set_brat -channelIndex=323 -brRatio=0
set_brat -channelIndex=324 -brRatio=0
set_brat -channelIndex=325 -brRatio=0
set_brat -channelIndex=326 -brRatio=0
set_brat -channelIndex=331 -brRatio=0
set_brat -channelIndex=332 -brRatio=0
set_brat -channelIndex=333 -brRatio=0
```

```
# decay of particle ℓ1
set_kfdp -channelIndex=3858 -products=11,16
set_brat -channelIndex=3858 -brRatio=0.5
set_mdme -channelIndex=3858 -decayType=1 -matrix=0
set_kfdp -channelIndex=3859 -products=13,16
set_brat -channelIndex=3859 -brRatio=0.5
set_mdme -channelIndex=3859 -decayType=1 -matrix=0
# Set all other ℓ1 decays to unphysical
set_mdme -channelIndex=3857 -decayType=-1

set_kfdp -channelIndex=3860 -products=14,16
set_brat -channelIndex=3860 -brRatio=0.5
set_mdme -channelIndex=3860 -decayType=1 -matrix=0
set_kfdp -channelIndex=3861 -products=12,16
set_brat -channelIndex=3861 -brRatio=0.5
set_mdme -channelIndex=3861 -decayType=1 -matrix=0

set_mstp -index=7 -value=7
set_msub -index=81 -value=1
set_msub -index=82 -value=1

exit
exit
exit
```

```
talk Pythia
PythiaMenu
statListLevel set 2
commonMenu
show_mdcy
show_kfdp
show_mdme
show_brat
exit
exit
exit

talk FileOutput
output create main_stream b1pair_350_10.sim
output path main_stream AllPath
output keepList main_stream
LRID_StorableBank LRIH_StorableBank EVCL_StorableBank
HEPG_StorableBank OBSP_StorableBank OBSV_StorableBank
exit

begin -nev 100000
show timer

exit
```

Note:

The above TCL file is written for the CDF Run II analysis framework. We used a custom *generatorMods* package (with *FillRun1BanksModule*) to create the LRID and EVCL banks that are required by the Run I Framework. After generating the Monte Carlo sample in Run II ROOT data format, we use the *BankTools* package to convert the sample to Run I YBOS data format and pass through Run I CDF detector simulation program QFL. For Run II analysis, this TCL file can be used directly with Run II detector simulation package *cdfSim*.

Appendix D

$b\bar{b}/c\bar{c}$ Background Scale Factor

Note that in Fig. 8.1, in the invariant mass less than 5 GeV/c^2 region where $b\bar{b}/c\bar{c}$ background dominates, the background Monte Carlo and data do not agree with each other. The $b\bar{b}/c\bar{c}$ background was not modeled correctly because old structure functions were used, thus an overall scale factor needs to be applied to $b\bar{b}/c\bar{c}$ background.

We examined the invariant mass of the two closest leptons in the less than 5 GeV/c^2 region by their lepton pair types, see Figure D.1, D.2, D.3, D.4.

For a closer look at the same sign lepton pair invariant mass, see Figure D.5, D.6.

Our conclusions are:

1. There are significant number of fakes from same sign (S.S.) lepton pairs in data, especially the low invariant mass region. These S.S. events in the data look nothing like real $b\bar{b}$, and that we expect them to be dominated by fakes, which are roughly sign-symmetric.

2. J/psi estimation from other sources is not significant. There are even less J/psi's in data than $b\bar{b}/c\bar{c}$ generated.

3. The exact invariant mass distribution from $b\bar{b}/c\bar{c}$ depends upon getting not just

the inclusive muon and electron branching ratios correct, but the particular exclusive decay modes as well. This is why we'd rather take all data below 5 GeV/c^2, rather than cutting on a particular value - that we expect the integral to be correct, while the exact shape may be a little off.

Our approach is to subtract the effect of S.S. lepton pairs from OS lepton pairs, and do the $b\bar{b}/c\bar{c}$ scaling in the 0 to 5 GeV/c^2 region. There are a small amount S.S. lepton pairs from $b\bar{b}/c\bar{c}$ as well, presumably generated in the $b\bar{b}/c\bar{c}$ simulation, however they should be subtracted as well because they may not be simulated correctly.

The invariant mass plots with S.S. lepton pairs subtracted from O.S. lepton pairs are shown in Figure D.7, D.8.

The $b\bar{b}/c\bar{c}$ scale factor is 287/137.546 = 2.1 (2.08657)

Root Kolmogorov test of the shape between $b\bar{b}/c\bar{c}$ and data result is 0.254 (the value is the compatibility probability of test), so they are somewhat compatible.

Notes:

We removed events if there is a PEM electron in one of the two closest leptons because the charge sign of PEM cannot be determined. There are 0 out of 477 events in data, and 6 out of 2838 events in $b\bar{b}/c\bar{c}$.

Table D.1: Number of data and $b\bar{b}/c\bar{c}$ events in each dilepton channel in the invariant mass of 2 closest lepton less than 5 GeV/c^2 region.

	e^-e^+	$\mu^-\mu^+$	$e^-\mu^+$	$e^+\mu^-$	$e^-\mu^-$	$e^+\mu^+$	e^-e^-	e^+e^+	$\mu^-\mu^-$	$\mu^+\mu^+$	Total
data	26	312	22	22	10	6	0	0	37	42	477
$b\bar{b}/c\bar{c}$	4.456	140.568	10.125	8.986	2.978	1.951	0	0	12.411	9.249	190.724

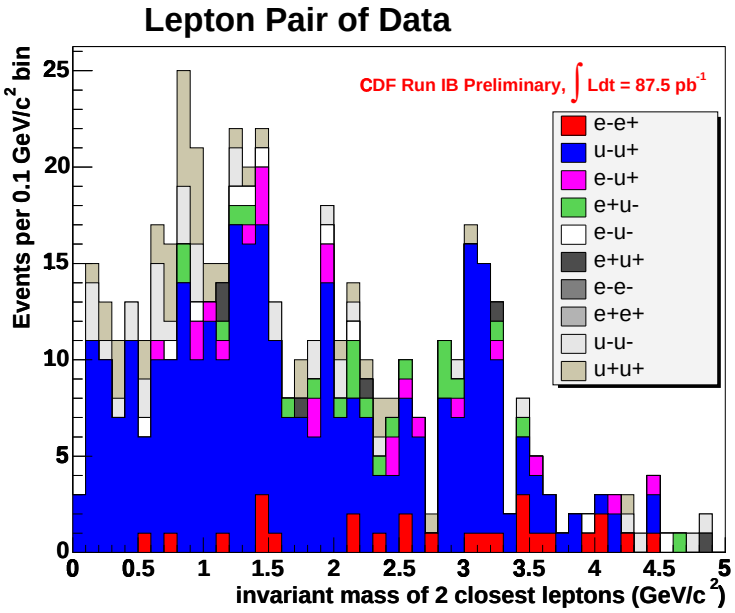

Figure D.1: Data invariant mass of the two closest leptons in the less than 5 GeV/c^2 region by lepton pair type.

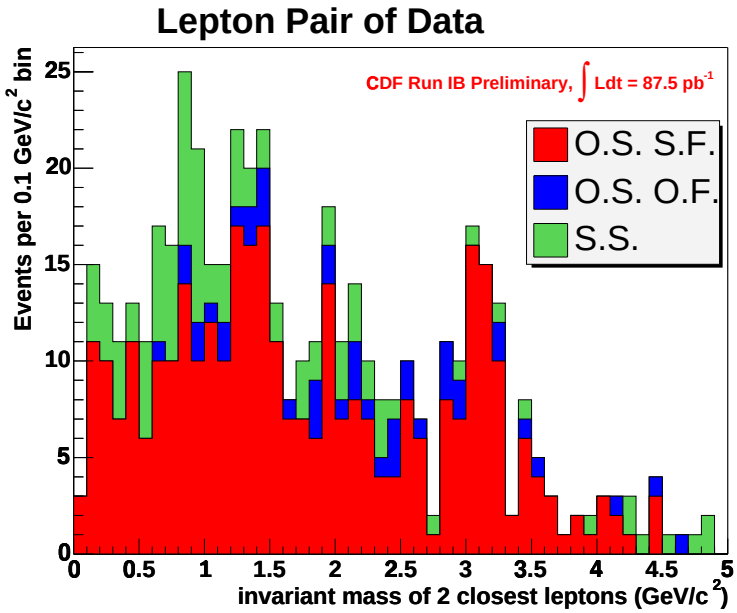

Figure D.2: Data invariant mass of the two closest leptons in the less than 5 GeV/c^2 region by S.S. and O.S. lepton pair type.

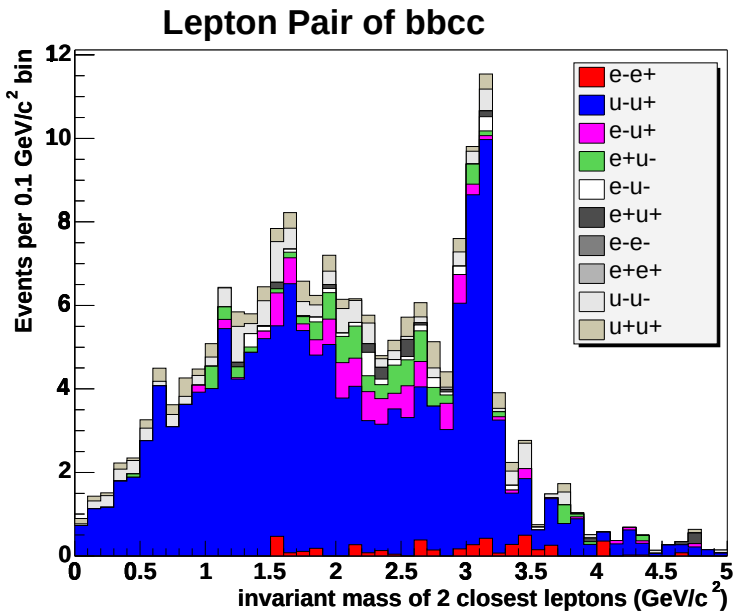

Figure D.3: $b\bar{b}/c\bar{c}$ invariant mass of the two closest leptons in the less than 5 GeV/c^2 region by lepton pair type.

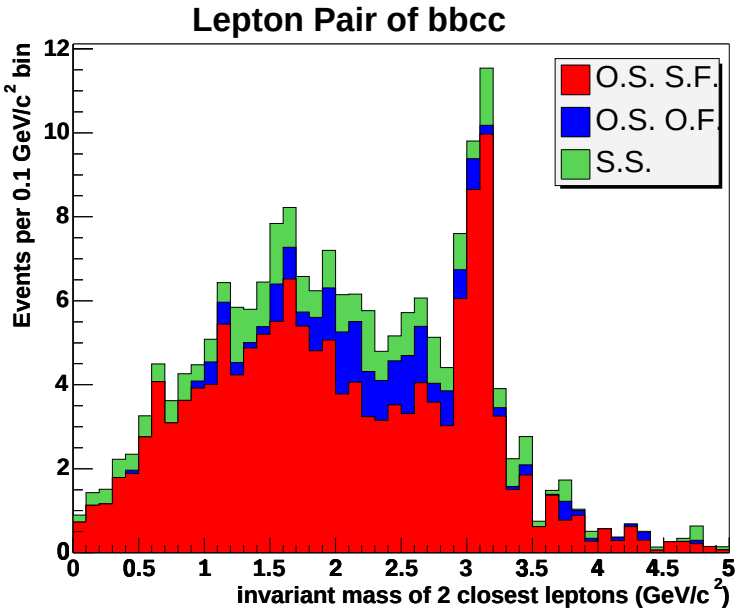

Figure D.4: $b\bar{b}/c\bar{c}$ invariant mass of the two closest leptons in the less than 5 GeV/c^2 region by S.S. and O.S. lepton pair type.

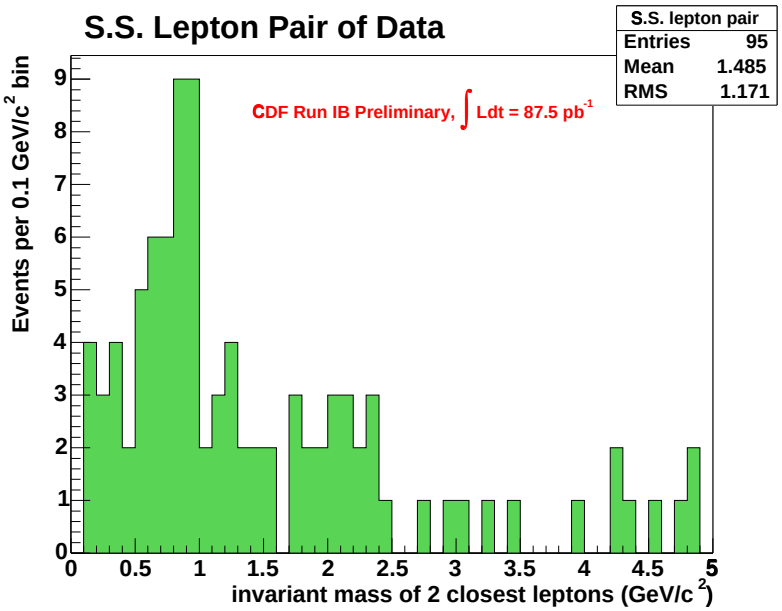

Figure D.5: Data invariant mass of the two closest leptons in the less than 5 GeV/c^2 region same sign lepton pair.

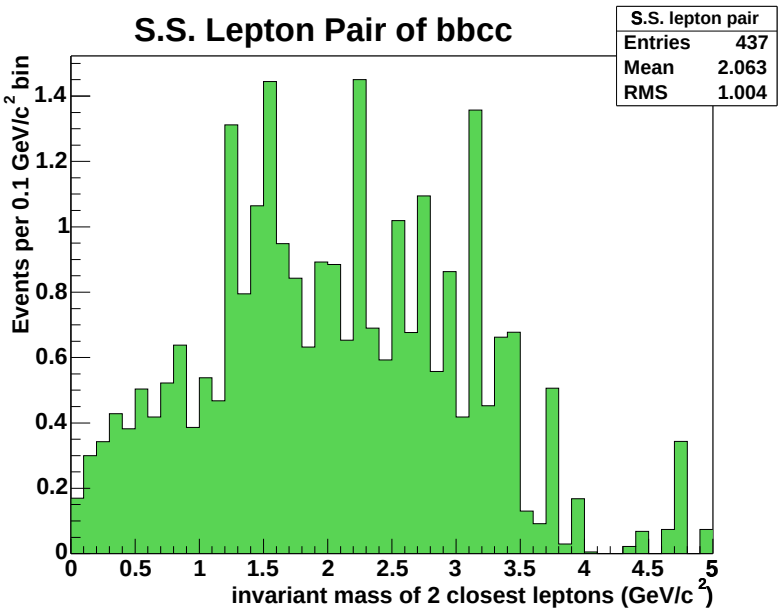

Figure D.6: $b\bar{b}/c\bar{c}$ invariant mass of the two closest leptons in the less than 5 GeV/c^2 region same sign lepton pair.

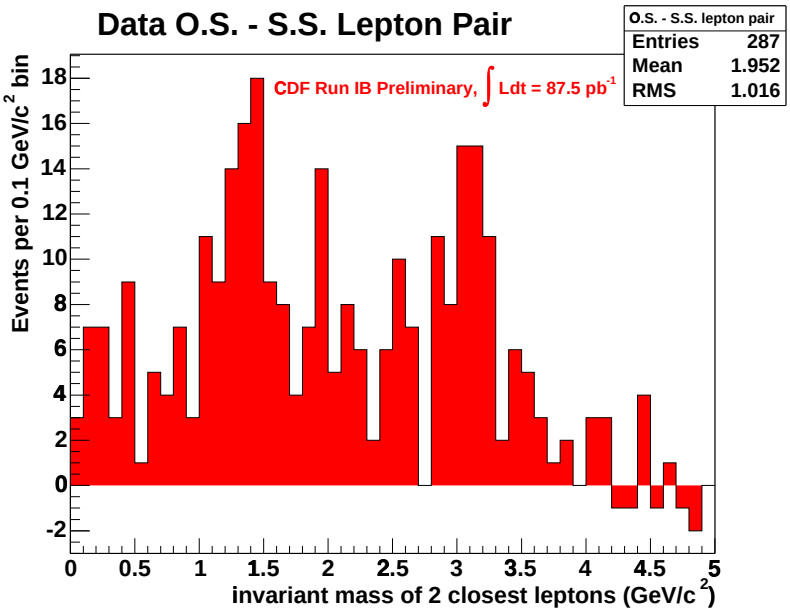

Figure D.7: Data invariant mass of the two closest leptons in the less than 5 GeV/c^2 region opposite sign lepton pair subtract same sign lepton pair.

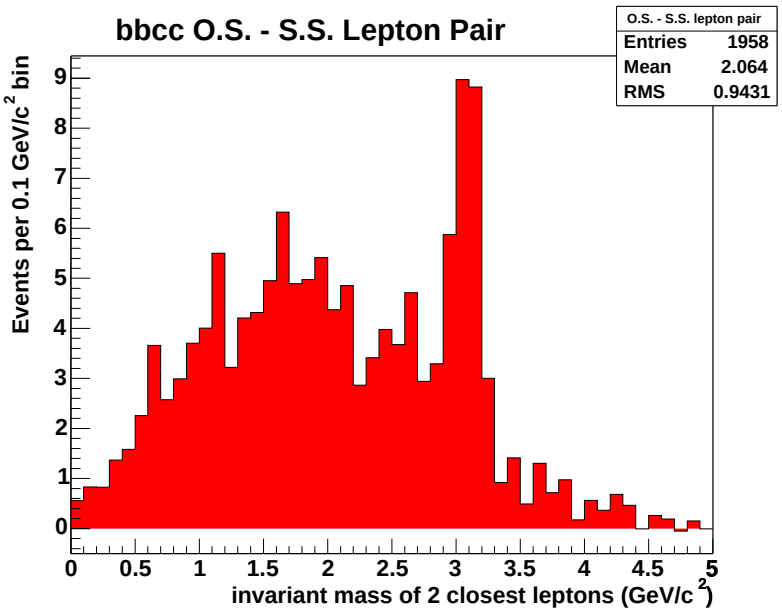

Figure D.8: $b\bar{b}/c\bar{c}$ invariant mass of the two closest leptons in the less than 5 GeV/c^2 region opposite sign lepton pair subtract same sign lepton pair.

Table D.2: Number of data and $b\bar{b}/c\bar{c}$ events in each trilepton channel in the invariant mass of 2 closest leptons less than 5 GeV/c^2 region.

	eee	$ee\mu$	$e\mu\mu$	$\mu\mu\mu$	Total
data	9	36	100	332	477
$b\bar{b}/c\bar{c}$	0.070	11.453	54.201	125.324	191.047

Appendix E

Combined Results from all Channels including eee, $ee\mu$, $e\mu\mu$ and $\mu\mu\mu$

In Fig. E.1, we plot the optimization value $\mathbb{A}$, where $a = 95\%$. We found the following cuts maximize $\mathbb{A}$ for all channels including eee, $ee\mu$, $e\mu\mu$ and $\mu\mu\mu$:

$$ISO < 6 \text{ GeV}, \ \not{E}_T > 20 \text{ GeV} \tag{E.1}$$

Table E.1 lists the number of events expected before and after the final optimization cuts from each type of background, the sum of all background, the number of data events and a sample MC signal point in all channels.

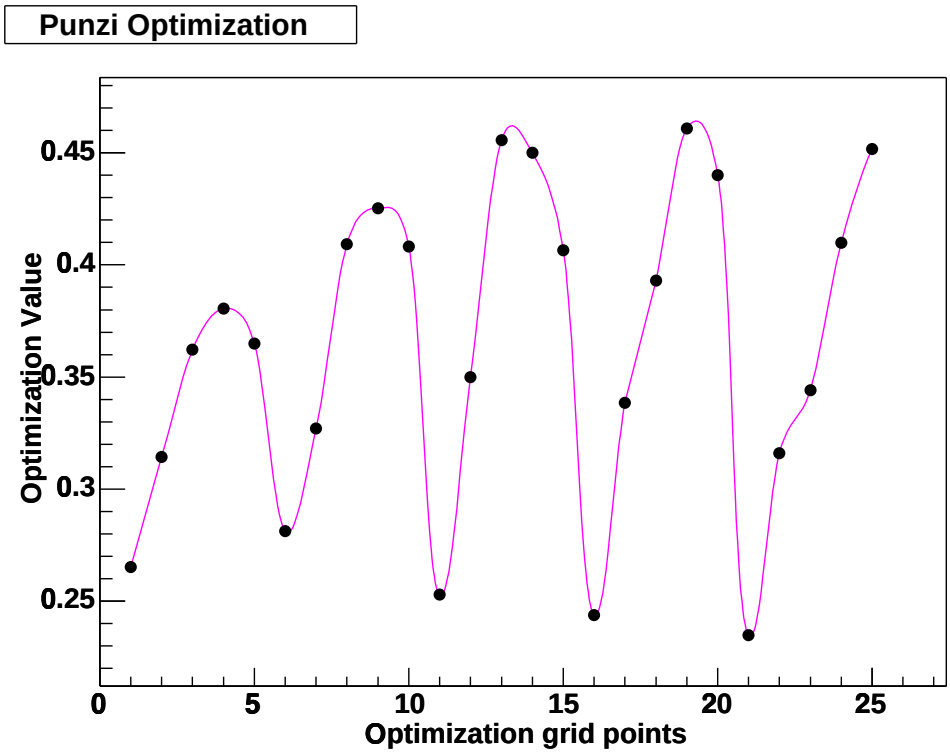

Figure E.1: Punzi search of the cut matrix to optimize value $\mathbb{A}$ (y axis), with $a = 95\%$. See Table. 8.1 for (x axis) grid points.

Table E.1: In all channels, number of expected background events contributed by $b\bar{b}/c\bar{c}$, Drell-Yan, $t\bar{t}$ and boson pair production, total number of expected background, data and signal Monte Carlo events remaining after each cut. All MC events are properly weighted with luminosity, lepton ID efficiency, and trigger efficiency.

all channels	Events remaining after each cut						
	$b\bar{b}/c\bar{c}$	Drell-Yan	$t\bar{t}$	Boson Pair	Sum BG	Data	MUED MC
before final optimization cuts	38.14	4.87	0.96	0.05	44.02	43	0.90
$ISO < 6$ GeV	3.93	4.74	0.10	0.02	8.79	15	0.64
$\not{E}_T > 20$ GeV	0.00	0.71	0.09	0.00	0.80	1	0.54

Appendix F

Results from the $\mu\mu\mu$ Channel

Cut Optimization The cut optimization for the $\mu\mu\mu$ channel is shown in Fig. F.1. We found the following cuts maximize $\mathbb{A}$ for the $\mu\mu\mu$ channels:

$$ISO < 8 \text{ GeV}, \ \not{E}_T > 20 \text{ GeV} \tag{F.1}$$

Table F.1 lists the number of events expected before and after the final optimization cuts from each type of background, the sum of all background, the number of data events and a sample MC signal point in the $\mu\mu\mu$ channel.

Table F.1: The number of expected background events contributed by $b\bar{b}/c\bar{c}$, Drell-Yan, $t\bar{t}$ and boson pair production, total number of expected background, data and signal Monte Carlo events remaining after each cut in the $\mu\mu\mu$ channel. All MC events are properly weighted with luminosity, lepton ID efficiency, and trigger efficiency.

$\mu\mu\mu$ channel	Events remaining after each cut						
	$b\bar{b}/c\bar{c}$	Drell-Yan	$t\bar{t}$	Boson Pair	Sum BG	Data	MUED MC
before final optimization cuts	17.70	4.81	0.44	0.04	22.99	20	0.26
$ISO < 8$ GeV	1.87	4.71	0.05	0.01	6.64	14	0.20
$\not{E}_T > 20$ GeV	0.00	0.71	0.05	0.00	0.76	1	0.16

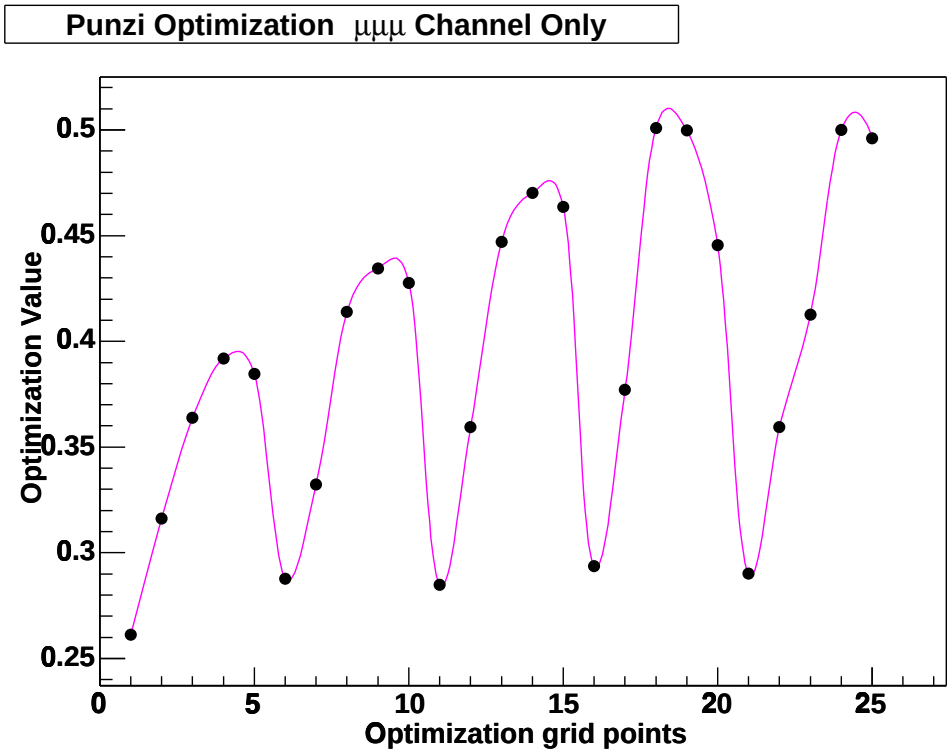

Figure F.1: Punzi search in $\mu\mu\mu$ channel of the cut matrix to optimize value $\mathbb{A}$ (y axis), with $a = 95\%$. See Table. 8.1 for (x axis) grid points.

Limits from the $\mu\mu\mu$ Channel Having observed 1 event with 0.76 expected background events in the $\mu\mu\mu$ channel, we obtain $N_{exp} = 4.36$ (3.48) at Confidence Level of 95% (90%). [1]

The total detection efficiency for the KK quark pairs, KK gluon-quark and KK gluon pair samples in the $\mu\mu\mu$ channel are listed in Table F.2.

Table F.2: Total Detection Efficiency in the $\mu\mu\mu$ Channel.

Sample	Total detection efficiency in the $\mu\mu\mu$ Channel
Q_1Q_1	1.5%
g_1Q_1	0.9%
g_1g_1	1.0%

[1] If we use charged multiplicity cut, we would observe 1 event with 0.21 expected background events, thus $N_{exp} = 4.66$ (3.77) at Confidence Level of 95% (90%).

The $\mu\mu\mu$ channel Q_1Q_1 production cross section limit at Confidence Level of 95% (90%) is:

$$\sigma_{Q_1Q_1} \quad < 11.1 \text{ pb } (8.9 \text{ pb}) \; ; \tag{F.2}$$

Thus the $\mu\mu\mu$ channel KK quark (excluding KK top) production cross section limit at Confidence Level of 95% (90%) is 22.2 pb (17.8 pb). Converting this to an extra dimension radius limit according to Fig. 4.2 we have $R^{-1} >$ 230 GeV (240 GeV).

For the combined production modes we have:

$$\begin{aligned} N_{exp} = (0.0145 \times \sigma_{\text{KK quark pair}} \times \frac{1}{2} \times \text{BR}(Q_1Q_1 \to lll + X) + \\ 0.009 \times 0.21 \times \sigma_{\text{KK quark pair}} \times \frac{1}{4} \times \text{BR}(Q_1Q_1 \to lll + X) + \\ 0.010 \times 0.11 \times \sigma_{\text{KK quark pair}} \times \frac{1}{4} \times \text{BR}(Q_1Q_1 \to lll + X)) \\ \cdot \int \mathcal{L} dt \end{aligned}$$

We obtain $\sigma_{\text{KK quark pair}} < 22.3$ pb (18.0 pb) at Confidence Level of 95% (90%)

Ignoring KK top production,

$\sigma_{KK} < 29.4$ pb (23.8 pb)

Converting this to an extra dimension radius limit according to Fig. 4.2 we have $R^{-1} >$ 240 GeV (250 GeV).

Interesting Event There is one event left after all cuts in the $\mu\mu\mu$ channel. The event displays of the remaining event (Run 63604 Event 108434) are shown in Figure F.2 and F.3.

The three lepton candidates are central muon, extension muon and central muon, sorted by transverse momentum in the descending order. Table F.3 shows the kine-

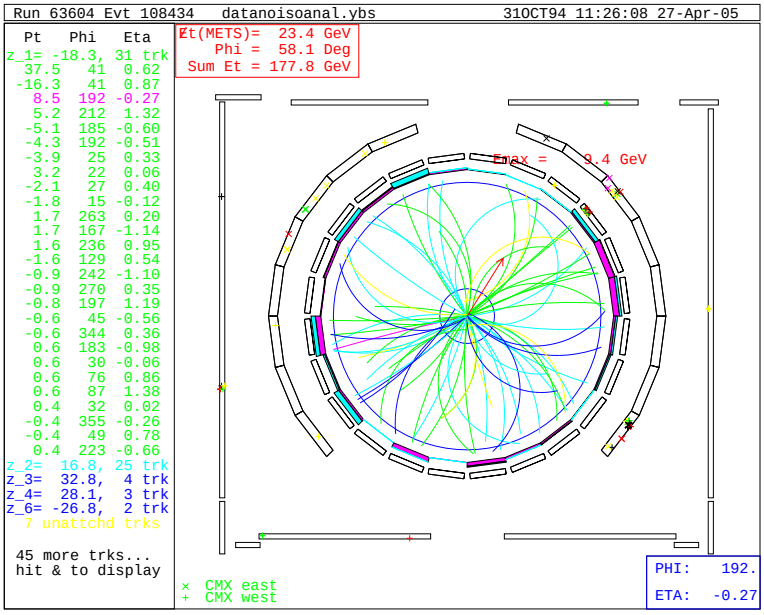

Figure F.2: Run 63604 Event 108434 event display.

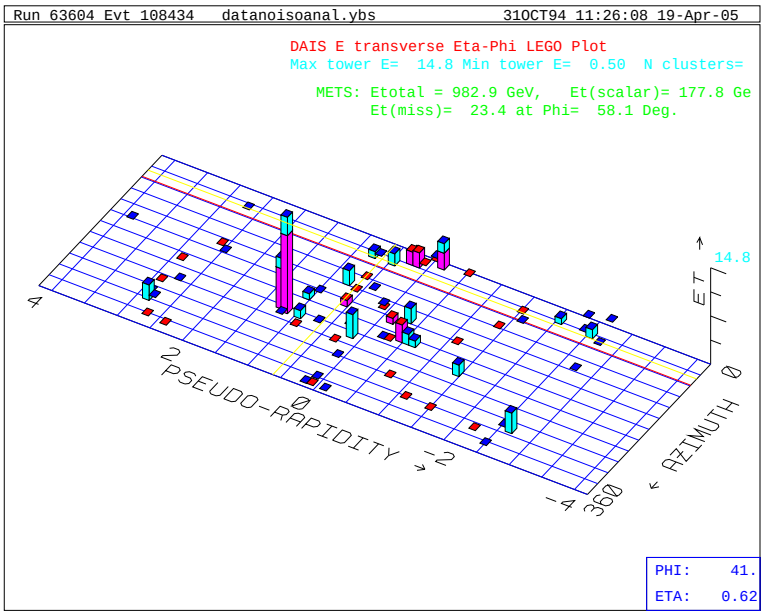

Figure F.3: Run 63604 Event 108434 transverse $\eta - \phi$ plot.

matics of the event.

The invariant mass of the two closest leptons is 5.45 GeV/c^2.

The missing energy of the event is 24.1 GeV.

There are 15 charged tracks with p_T greater than 2 GeV/c.

Table F.3: Summary of Event: Run 63604 Event 108434

	1st lepton	2nd lepton	3rd lepton
Species	CMU/P	CMX	CMU/P
p_T(GeV/c)	30.45	-15.71	8.98
ϕ (Radian)	0.71	0.71	3.35
η	0.62	0.87	-0.27
Isolation (GeV)	2.65	2.49	3.30

Appendix G

Charged Multiplicity

The signature of the UED signal we considered is multiple standard leptons, jets and missing energy. We do not use the jets signature in our event selection directly, - this is because the data sample we use has a relatively low integrated luminosity, and we can suppress most background events without requiring jets identification.

If we had a large amount of data (or perhaps for CDF Run II analysis), jets identification maybe required to further reduce background events. An alternative method is to include event charged multiplicity cut because jets activity will increase the event charged multiplicity.

We studied the effect of charged multiplicity [1] cut together with isolation cut and $\not\!\!E_T$ cut in the final cuts optimization.

We searched a cut matrix with isolation range from 2 GeV to 10 GeV with a step size of 1 GeV, $\not\!\!E_T$ range from 10 GeV to 30 GeV with a step size of 1 GeV, and charged multiplicity range from 0 to 10 with a step size of 1. In Fig. G.1, we plot the optimization value $\mathbb{A}$, where $a = 95\%$, with each grid point and charged multiplicity

[1] We calculate the event charged multiplicity by counting the number of charged tracks with $p_T > 2\ GeV/c$. We studied counting with various p_T requirements and 2 GeV/c has the best separation power.

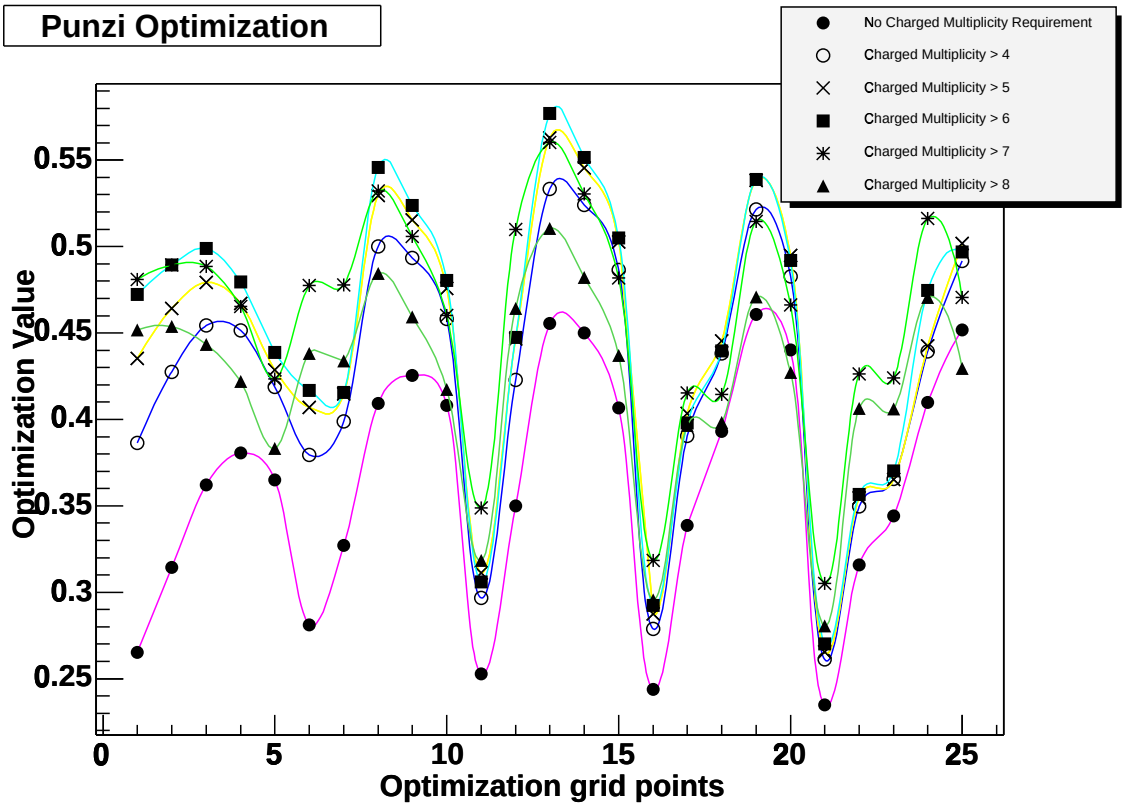

Figure G.1: Punzi search of the cut matrix to optimize value $\mathbb{A}$ (y axis), with $a = 95\%$. See Table. 8.1 for (x axis) grid points.

value. We found the following cuts maximize $\mathbb{A}$ for all channels:

$$ISO < 6 \text{ GeV}, \not{E}_T > 20 \text{ GeV}, \text{ Charged Multiplicity} > 6 \tag{G.1}$$

The number of events expected before and after the final optimization cuts are listed in Appendix E.

The separate cut optimization for the non-$\mu\mu\mu$ channels and the $\mu\mu\mu$ channel are shown in Fig. G.2 and Fig. G.3

We found the following cuts maximize $\mathbb{A}$ for the non-$\mu\mu\mu$ channels:

$$ISO < 4 \text{ GeV}, \not{E}_T > 15 \text{ GeV}, \text{ Charged Multiplicity} > 6 \tag{G.2}$$

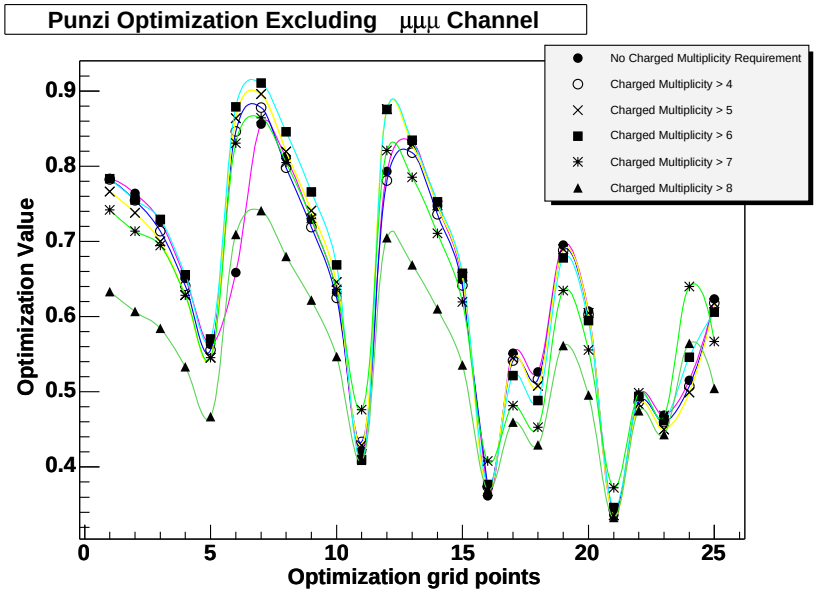

Figure G.2: Punzi search in non-$\mu\mu\mu$ channel of the cut matrix to optimize value $\mathbb{A}$ (y axis), with $a = 95\%$. See Table. 8.1 for (x axis) grid points.

and the following cuts maximize $\mathbb{A}$ for the $\mu\mu\mu$ channels:

$$ISO < 8 \text{ GeV}, \not{E}_T > 20 \text{ GeV}, \text{ Charged Multiplicity} > 6 \tag{G.3}$$

Fig. G.4 shows the charged multiplicity distribution of the MUED signal Monte Carlo, the SM background, and data, before imposing the final optimization cuts, in the non-$\mu\mu\mu$ channels.

Table G.1 lists the number of events expected before and after the final optimization cuts from each type of background, the sum of all background, the number of data events and a sample MC signal point, separated into non-$\mu\mu\mu$ channels and $\mu\mu\mu$ channel.

We decide not to use charge multiplicity cut because it doesn't improve our result [2]. In the non-$\mu\mu\mu$ channels before charged multiplicity cut there are 0.05

[2]Note that the optimal Punzi cuts for isolation and $\not{E}_T$ are the same whether we use the charged multiplicity cut or not, see Fig. G.1,G.2,G.3.

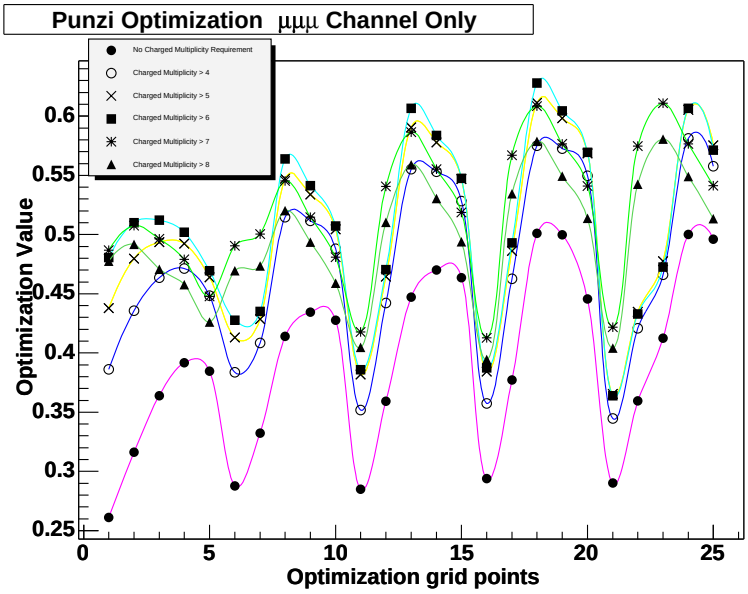

Figure G.3: Punzi search in $\mu\mu\mu$ channel of the cut matrix to optimize value $\mathbb{A}$ (y axis), with $a = 95\%$. See Table. 8.1 for (x axis) grid points.

background, after charged multiplicity cut there are 0.02 background [3]. In addition, using charged multiplicity cut will increase the systematic uncertainty [4]. Furthermore, without charged multiplicity cut, the total detection efficiency can be improved so we can obtain better cross section limit (see Table G.2).

[3] The number of expected events is the same 3.08 events in both cases using Bayesian method

[4] [72] studies quark and gluon jet charged track multiplicities and compares the Herwig and Pythia MC samples with the data. It indicates that for a 40 GeV jet with p_T cut of 500 MeV/c there are 30% systematic uncertainties of quark jets track multiplicities. Even though we use event charged multiplicity instead of jet charged multiplicity, and our p_T cut is at 2 GeV/c instead of 500 MeV/c, a systematic uncertainty still need to be assigned if we use charged multiplicity cut.

Table G.1: Separated into non-$\mu\mu\mu$ channels and $\mu\mu\mu$ channel, number of expected background events contributed by $b\bar{b}/c\bar{c}$, Drell-Yan, $t\bar{t}$ and boson pair production, total number of expected background, data and signal Monte Carlo events remaining after each cut. All MC events are properly weighted with luminosity, lepton ID efficiency, and trigger efficiency.

non-$\mu\mu\mu$ channels	Events remaining after each cut						
	$b\bar{b}/c\bar{c}$	Drell-Yan	$t\bar{t}$	Boson Pair	Sum BG	Data	MUED MC
before final optimization cuts	20.43	0.06	0.52	0.01	21.02	23	0.64
$ISO < 4$ GeV	0.44	0.04	0.04	0.00	0.52	3	0.42
$\not{E}_T > 15$ GeV	0.00	0.01	0.04	0.00	0.05	0	0.38
Charged Multiplicity > 6	0.00	0.00	0.01	0.00	0.02	0	0.34

$\mu\mu\mu$ channel	Events remaining after each cut						
	$b\bar{b}/c\bar{c}$	Drell-Yan	$t\bar{t}$	Boson Pair	Sum BG	Data	MUED MC
before final optimization cuts	17.70	4.81	0.44	0.04	22.99	20	0.26
$ISO < 8$ GeV	1.87	4.71	0.05	0.01	6.64	14	0.20
$\not{E}_T > 20$ GeV	0.00	0.71	0.05	0.00	0.76	1	0.16
Charged Multiplicity > 6	0.00	0.17	0.04	0.00	0.21	1	0.16

Table G.2: Total detection efficiency comparison of with and without charged multiplicity cut in combined, non-$\mu\mu\mu$, and $\mu\mu\mu$ channels.

Sample	with charged multiplicity	without charged multiplicity
Q_1Q_1	4.6% (3.2%, 1.4%)	5.0% (3.5%, 1.5%)
g_1Q_1	3.0% (2.1%, 0.9%)	3.0% (2.1%, 0.9%)
g_1g_1	3.0% (2.0%, 1.0%)	3.0% (2.0%, 1.0%)

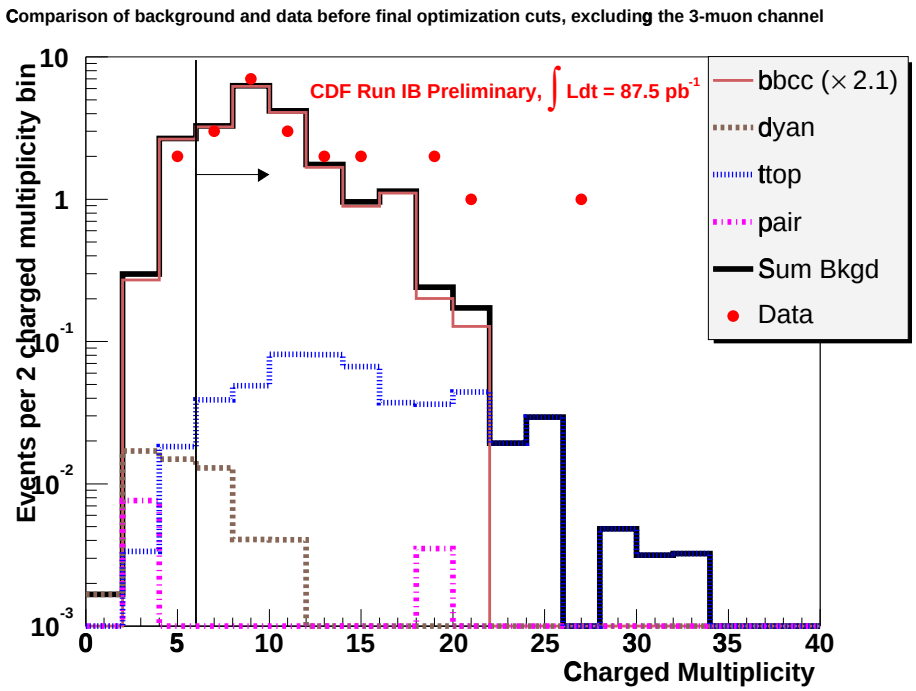

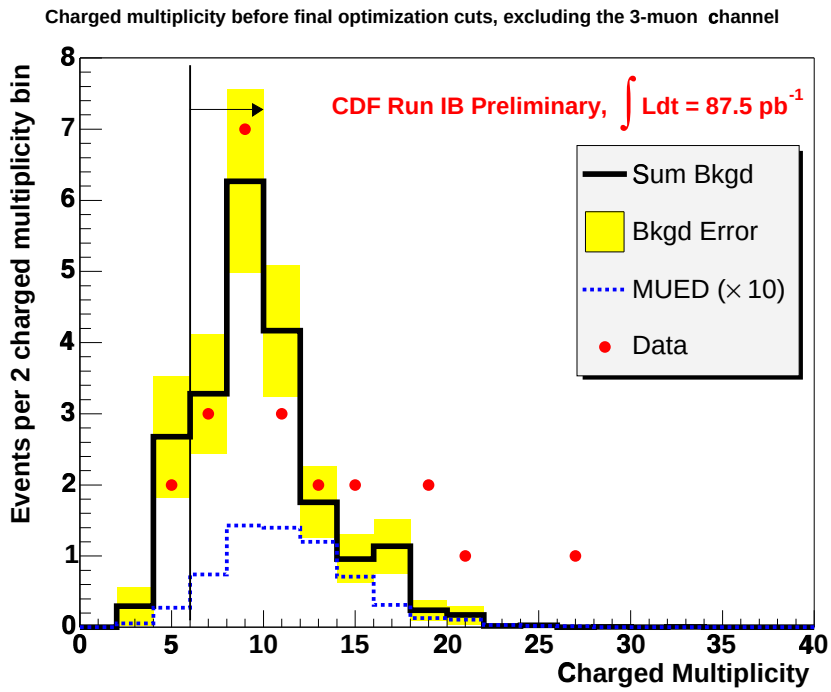

Figure G.4: Distributions of charged multiplicity in the non-$\mu\mu\mu$ channels. The top figure shows data and each type of background. The bottom figures shows the MUED signal, data and the total background with error band. The scale factor 2.1 is applied to $b\bar{b}/c\bar{c}$ background, and the total background includes $b\bar{b}/c\bar{c}$ background with scale factor 2.1 applied, Drell-Yan, $t\bar{t}$, and boson pairs. The vertical straight lines indicate the cut value and the arrows indicate the accepted values. Background MC samples are generated by SUSY working group (Appendix B).

Bibliography

[1] *Encyclopedia Britannica*, 2005.

[2] T. Appelquist, H.-C. Cheng and B. A. Dobrescu, *Bounds on Universal Extra Dimensions*, Phys. Rev. D **64**, 035002 (2001), hep-ph/0012100.

[3] K. Agashe, N. G. Deshpande and G. H. Wu, *Universal Extra Dimensions and $b \to s$ gamma*, Phys. Lett. B **514**, 309 (2001), hep-ph/0105084.

[4] T. Appelquist and B. A. Dobrescu, *Universal Extra Dimensions and the Muon Magnetic Moment*, Phys. Lett. B **516**, 85 (2001), hep-ph/0106140.

[5] N. Arkani-Hamed, H.-C. Cheng, B. A. Dobrescu and L. J. Hall, *Self-breaking of the Standard Model Gauge Symmetry*, Phys. Rev. D **62**, 096006 (2000), hep-ph/0006238.

[6] B. A. Dobrescu and E. Poppitz, *Number of Fermion Generations Derived from Anomaly Cancellation*, Phys. Rev. Lett. **87**, 031801 (2001), hep-ph/0102010.

[7] T. Appelquist, B. A. Dobrescu, E. Ponton and H. U. Yee, *Proton Stability in Six Dimensions*, Phys. Rev. Lett. **87**, 181802 (2001), hep-ph/0107056.

[8] T. Appelquist, B. A. Dobrescu, E. Ponton and H. U. Yee, *Neutrinos vis-a-vis the Six-dimensional Standard Model*, Phys. Rev. D **65**, 105019 (2002), hep-ph/0201131.

[9] N. Arkani-Hamed, H.-C. Cheng, B. A. Dobrescu and L.J. Hall, *Self-Breaking of the Standard Model Gauge Symmetry*, Phys. Rev. D **62**, 096006 (2000), hep-ph/0006238.

[10] H.-C. Cheng, J. L. Feng, and K. T. Matchev, *Kaluza-Klein Dark Matter*, Phys. Rev. Lett. **89**, 211301 (2002), hep-ph/0207125.

[11] D. Hooper and G. D. Kribs, *Probing Kaluza-Klein Dark Matter with Neutrino Telescopes*, Phys. Rev. D **67**, 055003 (2003), hep-ph/0208261.

[12] C. Macesanu, C. D. McMullen, and S. Nandi, *New Signal for Universal Extra Dimensions*, Phys. Lett. B546 (2002) 253-260, hep-ph/0207269.

[13] S. L. Glashow, in *Partial Symmetries Of Weak Interactions*, Nucl. Phys. **22**, 579-588, 1961; S. Weinberg, Phys. Rev. Lett. **19**, 1264-66, 1967; A. Salam, in *Elementary Particle Theory*, N. Svartholm, ed. (Stockholm: Almquist and Wiksell, 1968).

[14] K. G. Wilson, in *Confinement of Quarks*, Phys.Rev.**D10**:2445-2459 (1974); G. Altarelli and G. Parisi, in *Asymptotic freedom in parton language*, Nucl.Phys. **B126**:298 (1977).

[15] M. Drees and S. Martin, *Implications of SUSY Model Building*, Report of the DPF Working Group on "Electroweak Symmetry Breaking and Beyond the Standard Model",March 1995, hep-ph/9504324.

[16] See e.g., K. D. Lane, *Technicolor 2000*, hep-ph/0007304; *Two Lectures on Technicolor*, hep-ph/0202255.

[17] See e.g., C. Kounnas, A. Masiero, D. V. Nanopoulos and K. A. Olive, *Grand Unification With and Without Supersymmetry and Cosmological Implications*,

World Scientfic, Singapore (1984); G. G. Ross, *Grand Unified Theories*, Benjamin/Cummings, MA, (1983).

[18] See e.g., H. P. Nilles, *Supersymmetry, Supergravity and Particle Physics*, Phys. Rept. 110 (1984) 1; M. Drees, *An Introduction to Supersymmetry*, Lectures given at Seoul summer symposium on field theory, August 1996, hep-ph/9611409; D. J. H. Chung, L. L. Everett, G. L. Kane, S. F. King, J. Lykken and L. T. Wang, *The Soft Supersymmetry-breaking Lagrangian: Theory and Applications*, Phys. Rept. **407**, 1 (2005), hep-ph/0312378.

[19] See e.g., C. Csaki, *TASI Lectures on Extra Dimensions and Branes*, hep-ph/0404096 (2004).

[20] T. G. Rizzo, *Pedagogical Introduction to Extra Dimensions*, hep-ph/0409309 (2004).

[21] J. D. Lykken, *Phenomenology Beyond the Standard Model*, hep-ph/0503148 (2005).

[22] See e.g., G. Landsberg, *Collider Searches for Extra Dimensions*, hep-ex/0412028 (2004); M. K. Unel, *Searches for Extra Dimensions at the Tevatron*, hep-ex/0411067 (2004).

[23] G. Nordström, *Über die Möglichkeit, das elektromagnetische Feld und das Gravitationsfeld zu vereinigen*, Phys. Zeitschr. **15** (1914) 504.

[24] T. Kaluza, Sitzungsber. Preuss. Akad. Wiss., Phys. Math. Klasse (1921) 966.

[25] O. Klein, Nature **188** (1926) 516.

[26] N. Arkani-Hamed, S. Dimopoulos and G. Dvali, *The Hierarchy Problem and New Dimensions at a Millimeter*, Phys. Lett. **B429** (1998) 263, hep-

ph/9803315; *Phenomenology, Astrophysics and Cosmology of Theories with Sub-Millimeter Dimensions and TeV Scale Quantum Gravity*, Phys. Rev. **D59** (1999) 086004, hep-ph/9807344.

[27] C. D. Hoyle, U. Schmidt, B. R. Heckel, E. G. Adelberger, J. H. Gundlach, D. J. Kapner, H. E. Swanson, *Sub-millimeter Tests of the Gravitational Inverse-square Law: A Search for "Large" Extra Dimensions*, Phys. Rev. Lett. **86** (2001) 1418-1421, hep-ph/0011014; *Sub-millimeter Tests of the Gravitational Inverse-square Law*, Phys. Rev. D **70** (2004) 042004, hep-ph/0405262.

[28] E. G. Adelberger, B. R. Heckel, A. E. Nelson, *Tests of the Gravitational Inverse-Square Law*, Ann. Rev. Nucl. Part. Sci. **53** (2003) 77-121, hep-ph/0307284.

[29] D. Acosta, *et al.*, (The CDF Collaboration), *Search for Kaluza-Klein Graviton Emission in $p\bar{p}$ Collisions at $\sqrt{s} = 1.8$ TeV using the Missing Energy Signature*, Phys. Rev. Lett. **92** (2004) 121802, hep-ex/0309051.

[30] The D0 Collaboration, *Search for Large Extra Dimensions in the Monojet + Missing ET Channel at D0*, Phys. Rev. Lett. **90** (2003) 251802, hep-ex/0302014.

[31] L. Randall and R. Sundrum, *A Large Mass Hierarchy from a Small Extra Dimension*, Phys. Rev. Lett. **83**, 3370 (1999), hep-ph/9905221; *An Alternative to Compactification*, Phys. Rev. Lett. **83**, 4690 (1999), hep-th/9906064.

[32] C. Macesanu, C. D. McMullen and S. Nandi, *Collider Implications of Universal Extra Dimensions*, Phys. Rev. D **66**, 015009 (2002), hep-ph/0201300.

[33] D. A. Dicus, C. D. McMullen and S. Nandi, *Collider Implications of Kaluza-Klein Excitations of the Gluons*, Phys. Rev. D **65**, 076007 (2002), hep-ph/0012259.

[34] H.-C. Cheng, K. T. Matchev and M. Schmaltz, *Bosonic Supersymmetry? Getting Fooled at the LHC*, Phys. Rev. D **66**, 056006 (2002), hep-ph/0205314.

[35] H.-C. Cheng, K. T. Matchev and M. Schmaltz, *Radiative Corrections to Kaluza-Klein Masses*, Phys. Rev. D **66**, 036005 (2002), hep-ph/0204342.

[36] C. D. Carone, J. M. Conroy, M. Sher, and I. Turan, *Universal Extra Dimensions and Kaluza Klein Bound States*, Phys. Rev. D **69**, 074018 (2004), hep-ph/0312055.

[37] J. Thompson, *Introduction to Colliding Beams at Fermilab*, FERMILAB-TM-1909 (1994).

[38] The CDF detector is described in F. Abe, *et al.*, (The CDF Collaboration), Nucl. Instrum. Methods **A271**, 387 (1988) and the references within.

[39] The CDF upgrades are described in F. Abe, *et al.*, (The CDF Collaboration), Phys. Rev. **D50**, 2966 (1994); D. Amidei, *et al.*, Nucl. Instrum. Methods **A350**, 73 (1994) and the references within.

[40] J. D. Cockcroft and E. T. S. Walton, Artificial Production of Fast Protons, Nature **129**, 242 (1932).

[41] D. Mohl, G. Petrucci, L. Thorndahl, and S. van der Meer, Physics and Technique of Stochastic Cooling, Phys. Rep. **58**, 73-119 (1980).

[42] T. G. Rizzo, *Probes of Universal Extra Dimensions at Colliders*, Phys. Rev. D **64**, 095010 (2001), hep-ph/0106336.

[43] J. M. Smillie, B. R. Webber , *Distinguishing Spins in Supersymmetric and Universal Extra Dimension Models at the Large Hadron Collider*, hep-ph/0507170, 2005.

[44] A. J. Barr, *Determining the Spin of Supersymmetric Particles at the LHC Using Lepton Charge Asymmetry*, Phys. Lett. B **596**, 205 (2004), hep-ph/0405052.

[45] F. Abe, *et al.*, (The CDF Collaboration), *Search for Chargino-Neutralino Production at the Fermilab Tevatron Collider*, Phys. Rev. Lett. **80**, 5275 (1998).

[46] B. Tannenbaum, *A Search for Chargino-Neutralino Production at the Fermilab Tevatron Collider*, CDF Note 4571 (1998).

[47] J.P. Done et al.,*SUSY Dilepton Selection for Run I*, CDF Note 4446 (1998). Also see CDF Note 3472.

[48] E. Buckley-Geer and S. Lammel, *How to Find Out What Run IB Data is Available*, CDF Note 2657 (1995).

[49] The Particle Data Group, *The Review of Particle Physics*, 2004 Edition.

[50] T. Abe et al., The CDF Collaboration, *Measurement of the B Meson and b Quark Cross Section at sqrts = 1.8 TeV Using the Exclusive Decay B0 → J/psi K*(892)0*, Phys. Rev. D **50**, 4252 (1994).

[51] Todd. A. Keaffaber, *Measurement of the B+ Meson Cross Section in Proton-Antiproton Collisions at 1.8 TeV*, CDF Note 5443 (2000).

[52] T. Affolder et al., The CDF Collaboration, *Measurement of the tt-bar Production Cross Section in p anti-p Collisions at s**(1/2) = 1.8 TeV*, Phys. Rev. D **64**, 032002 (2001).

[53] J. Ohnemus, J. F. Owens *Order- alpha_s calculation of hadronic ZZ production*, Phys. Rev. D **43**, 3626 (1991).

[54] J. Ohnemus, *Order- alpha_s calculation of hadronic WZ production*, Phys. Rev. D **44**, 3477 (1991).

[55] J. Ohnemus, *Order- alpha_s calculation of hadronic W-W+ production*, Phys. Rev. D **44**, 1403 (1991).

[56] J. M. Campbell, R. K. Ellis *An Update on Vector Boson Pair Production at Hadron Colliders*, Phys. Rev. D **60**, 113006 (1999), hep-ph/9905386.

[57] F. Abe et al., The CDF Collaboration, *Measurement of Z0 and Drell-Yan Production Cross Sections Using Dimuons in p-barp Collisions at Sqrt[s]=1.8 TeV*, Phys. Rev. D **59**, 052002 (1999).

[58] F. Abe et al., The CDF Collaboration, *Measurement of Drell-Yan Electron and Muon Pair Differential Cross Sections in p-barp Collisions at Sqrt[s]=1.8 TeV*, Phys. Rev. D **49**, 1 (1994).

[59] S. Tether, *The Fake Lepton Rate for the Run IB Susy Trilepton Analysis*, CDF Note 3566 (1996).

[60] A. Koen, *Search for R-Parity Violating Susy in the CDF Multi-Lepton Channel*, CDF Note 5212 (1999).

[61] H. Baer, F.E. Paige, S.D. Protopescu, X. Tata, *ISAJET 7.40: A Monte Carlo Event Generator for* $pp, \bar{p}p$, *and* e^+e^- *Reactions*, hep-ph/9810440 (1998).

[62] T. Sjostrand, L. Lonnblad, S. Mrenna, *PYTHIA 6.2 Physics and Manual*, hep-ph/0108264 (2001).

[63] M. SHAPIRO et al, *A User's Guide to QFL*, CDF Note 1810 (1992).

[64] The CTEQ Collaboration, http://www.phys.psu.edu/ cteq/.

[65] J.P. Done, M. Chertok, T. Kamon, *Study of Run IB Lepton Identification Efficiencies for SUSY searches*, CDF Note 4218 (1997).

[66] J.P. Done, M. Chertok, T. Kamon, *Study of Run IB Lepton Isolation Efficiencies for SUSY Searches*, CDF Note 4291 (1997).

[67] S. Kopp and C. Grosso-Pilcher, *A Good Run List for The 1992-1993 CDF Run*, CDF Note 1992 (1993).

[68] M. Krasberg, T. LeCompte, *CMCOS: The Run 1A Cosmic Ray Filter*, CDF Note 2032 (1993).

[69] G. Punzi, *Sensitivity of Searches for New Signals and its Optimization*, hep-physics/0308063.

[70] D. Cronin-Hennessy, A. Beretvas, *Luminosity at CDF*, CDF Note 4721 (1998).

[71] J. Conway, K. Maeshima, *Upper Limits on Poisson Processes Incorporating Uncertainties in Acceptance and Background*, CDF Note 4476 (1998).

[72] A. Korytov, A. Pronko, A. Safonov, *Update on the Measurement of Charged Particle Multiplicities in Gluon and Quark Jets*, CDF Note 6809, 5899 (2003).

[73] C. Lin, *CDF Run II Online Trigger Rates Monitor (ScalerMon) and Dynamic Prescaling Algorithms*, CDF/DOC/TRIGGER/7832.